Progress on Perovskite Materials and Solar Cells with Mixed Cations and Halide Anions

doi: info:doi/10.1021/acsami.7b06001

ACS APPLIED MATERIALS & INTERFACES

Review

www.acsami.org

Progress on Perovskite Materials and Solar Cells with Mixed Cations and Halide Anions

Luis K. Ono,[‡] Emilio J. Juarez-Perez,[‡] and Yabing Qi*

Energy Materials and Surface Sciences Unit (EMSS), Okinawa Institute of Science and Technology Graduate University (OIST), 1919-1 Tancha Onna-son, Okinawa 904-0495, Japan

ABSTRACT: Organic−inorganic halide perovskite materials (e.g., $MAPbI_3$, $FAPbI_3$, etc.; where MA = $CH_3NH_3^+$, FA = $CH(NH_2)_2^+$) have been studied intensively for photovoltaic applications. Major concerns for the commercialization of perovskite photovoltaic technology to take off include lead toxicity, long-term stability, hysteresis, and optimal bandgap. Therefore, there is still need for further exploration of alternative candidates. Elemental composition engineering of $MAPbI_3$ and $FAPbI_3$ has been proposed to address the above concerns. Among the best six certified power conversion efficiencies reported by National Renewable Energy Laboratory on perovskite-based solar cells, five are based on mixed perovskites (e.g., $MAPbI_{1-x}Br_x$, $FA_{0.85}MA_{0.15}PbI_{2.55}Br_{0.45}$, $Cs_{0.1}FA_{0.75}MA_{0.15}PbI_{2.49}Br_{0.51}$). In this paper, we review the recent progress on the synthesis and fundamental aspects of mixed cation and halide perovskites correlating with device performance, long-term stability, and hysteresis. In the outlook, we outline the future research directions based on the reported results as well as related topics that warrant further investigation.

KEYWORDS: *perovskite, solar cell, mixed cations, mixed halides, stability, hysteresis*

1. INTRODUCTION

Organic−inorganic halide perovskite materials (hereinafter denoted as "perovskites") continue to attract worldwide attention, shown by a rapid increase in the number of publications per year (Figure 1a).[1] $CH_3NH_3PbI_3$ and $CH_3NH_3PbBr_3$ perovskites were first incorporated as light harvesters in liquid dye-sensitized solar cells in 2009 by Kojima et al.[2] In 2012, a significant breakthrough was made with the introduction of all solid-state $CH_3NH_3PbI_3$ perovskite solar cells by Kim et al.[3] Since then, perovskite solar cells have been under the spotlight with a cluster of fundamental scientific discoveries[4−39] as well as breakthroughs in solar-to-electricity power conversion efficiencies (PCEs).[40] The highest certified efficiency of 22.1% as of today is only a few percent points shy of that of the best single-crystalline silicon solar cells.[40−43] Perovskite solar cells are considered as the most promising candidate for the next generation high efficiency solar cell technology that is compatible with low-cost, low-temperature processing, flexible substrates, and large-area (module) fabrication processes.[4,10,23,25,44−58]

Highly efficient perovskite solar cells are composed of perovskites that have an ABX_3 three-dimensional (3D) structure and are commonly composed of an organic/inorganic monovalent cation, A = (methylammonium (MA), $CH_3NH_3^+$; formamidinium (FA), $CH(NH_2)_2^+$; Cs^+; Rb^+), a divalent metal cation, B = (Pb^{2+}; Sn^{2+}), and halide anion motif X_3 = (I^-; Br^-; Cl^-). Pristine methylammonium lead iodide perovskite ($MAPbI_3$) has been intensively used as light harvesting material from earlier times of perovskite solar cell developments.[2,3,42,43,59] Perovskite compositions with single ions occupying each of A, B, and X sites (e.g., $MAPbI_3$, $FAPbI_3$, etc.) are hereinafter denoted as "simple perovskites" and has been intensively studied (Figure 1a). In earlier studies, perovskites with mixed halides including minute quantities of Cl^- in the X_3 motif of $MAPbI_3$ (i.e., $MAPbI_{3-x}Cl_x$) were employed,[60,61] and currently there is still a high predominance of employing high contents of iodine-based perovskite

Received: May 9, 2017
Accepted: July 6, 2017
Published: July 6, 2017

DOI: 10.1021/acsami.7b06001
ACS Appl. Mater. Interfaces XXXX, XXX, XXX−XXX

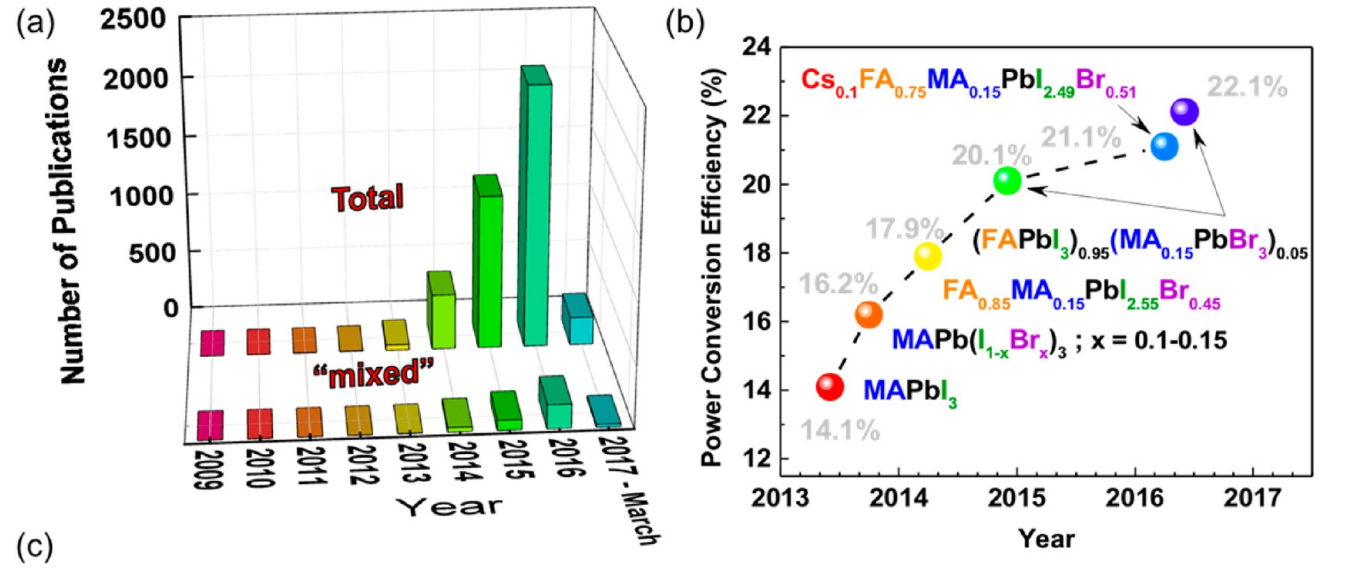

(c)

Pb-Based	MA	(MA,FA)	(MA,Cs)	(MA,Rb)	FA	(FA,Cs)	(FA,Rb)	Cs	(Cs,Rb)	Rb	(MA,FA,Cs)	(MA,FA,Rb)	(FA,Cs,Rb)	(MA,FA,Cs,Rb)
I	$MAPbI_3$	$(MA,FA)PbI_3$	$(MA,Cs)PbI_3$		$FAPbI_3$	$(FA,Cs)PbI_3$	$(FA,Rb)PbI_3$	$CsPbI_3$		$RbPbI_3$				
(I,Br)	MAPb(I,Br)	(MA,FA)Pb(I,Br)	(MA,Cs)Pb(I,Br)		FAPb(I,Br)	(FA,Cs)Pb(I,Br)		CsPb(I,Br)			(MA,FA,Cs)Pb(I,Br)	(MA,FA,Rb)Pb(I,Br)	(FA,Cs,Rb)Pb(I,Br)	(MA,FA,Cs,Rb)Pb(I,Br)
Br	$MAPbBr_3$				$FAPbBr_3$			$CsPbBr_3$	$(Cs,Rb)PbBr_3$	$RbPbBr_3$				
(I,Cl)	MAPb(I,Cl)	(MA,FA)Pb(I,Cl)			FAPb(I,Cl)			CsPb(I,Cl)						
(Br,Cl)	MAPb(Br,Cl)							CsPb(I,Br)						
Cl	$MAPbCl_3$				$FAPbCl_3$			$CsPbCl_3$	$(Cs,Rb)PbCl_3$	$RbPbCl_3$				
(I,Br,Cl)	MAPb(I,Br,Cl)													

Figure 1. (a) Number of publications retrieved from Web of Science (Thomson Reuters) as a function of the year using the following search keywords: "perovskite" AND "solar" AND "cell" (AND "mixed").[1] (b) Best research perovskite solar cells efficiencies certified by NREL.[40] For each of certified efficiencies, the chemical compositions of mixed perovskites are specified. (c) matrix of several simple and mixed cations and mixed halides Pb-based perovskites generated by the permutation of A = (MA,FA,Cs,Rb) and X = (I,Br,Cl). The perovskite compositions marked in yellow are documented in the literature. The green ones correspond to widely studied in the literature due to suitability for optoelectronic applications. The orange ones are the ones receiving great attention. Finally, the white boxes are perovskite compositions not still explored.

deposition recipes for photovoltaic applications.[13,24−26] In fact, except for the first certified efficiency record reported for hybrid perovskite research cells using phase pure $MAPbI_3$,[59] the following subsequent five National Renewable Energy Laboratory (NREL) records with publicly disclosed information used A and/or X site mixed hybrid perovskites[62−66] (hereinafter denoted as "mixed perovskites"), see Figure 1b. However, based on Figure 1a, the fraction of the number of publications employing mixed perovskites with respect to the total number are still relatively low, ∼9% in 2016 and ∼10% as of April 15th, 2017.[1] A question naturally arises whether the future trends for perovskite photovoltaic technology should be focused on mixed perovskites. In this review, we outline systematically the benefits to employ mixed cations and halides in perovskite materials. For example, we will highlight the following advantages: (i) higher performance, (ii) increased stability, (iii) enhanced carriers charge transport, (iv) enabling band gap tuning, (v) less pronounced hysteresis, (vi) a thorough understanding of fundamental aspects of Pb-based mixed cations and halides may lead to alternative Pb-free perovskites by rational designs. In this review, only the Pb-based mixed cations and halides perovskites are to be covered based on the fact that substantial knowledge has been accumulated with several congruent conclusions for Pb-based mixed cations and halides perovskites. In Figure 1c, we marked the Pb-based pure and mixed cations and halides perovskites that have been reported in the literature. The color coding signifies: (yellow,-green,orange) = reported in the literature; green = widely studied composition; orange = receiving attention recently; white = not reported composition. Following our survey (Figure 1c) and aiming a comprehensive description of mixed cations and mixed halides perovskites, we start with the description of the simpler systems of mixed A cations (FA/MA)PbI_3, (MA/Cs)PbI_3, (FA/Cs)PbI_3, (FA/Rb)PbI_3 perovskites (section 2) and the mixed X halides MAPb(I/Cl), FAPb(I/Cl), MAPb(I/Br), FAPb(I/Br), MAPb(Br/Cl), MAPb(I/Br/Cl), CsPb(I/Br), CsPb(Br/Cl), CsPb(I/Cl) perovskites (section 3). Based on important concepts described in sections 2 and 3, the more complex systems of simultaneously mixed A and mixed X (MA/Cs)Pb(I/Br), (FA/MA)Pb(I/Br), (FA/MA)Pb(I/Cl), (FA/Cs)Pb(I/Br), (Cs/FA/MA)Pb(I/Br), (Rb/FA/MA)Pb(I/Br), (Rb/Cs/FA)Pb(I/Br), (Rb/Cs/FA/MA)Pb(I/Br) perovskites are described in section 4.

DOI: 10.1021/acsami.7b06001
ACS Appl. Mater. Interfaces XXXX, XXX, XXX−XXX

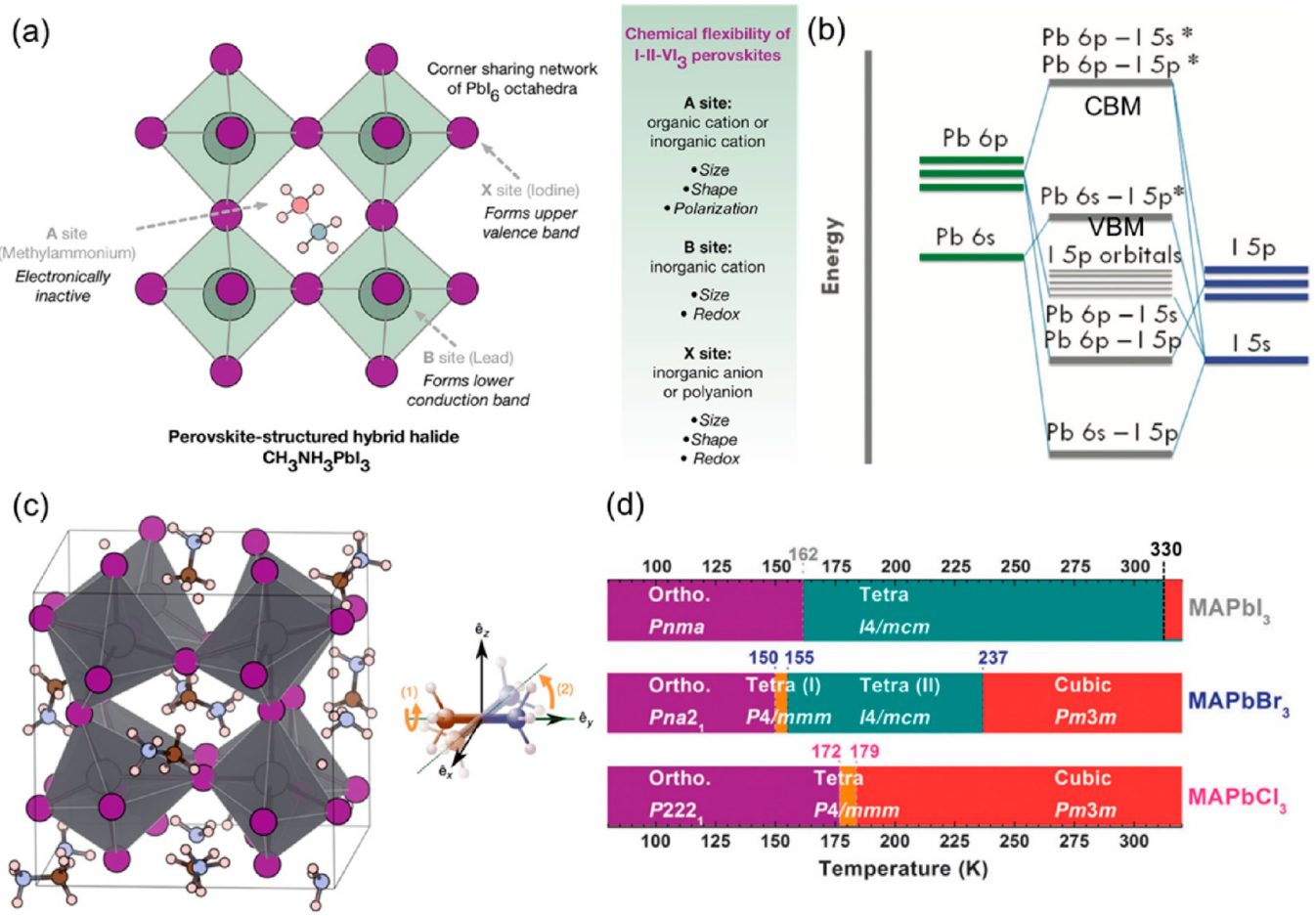

Figure 2. (a) Illustration of a $CH_3NH_3PbI_3$ perovskite structure with A, B, and X lattice sites. The redox chemistry of ions influence the valence and conduction band energies and orbital composition. Reprinted with permission from ref 67. Copyright 2015 American Chemical Society. (b) Illustration of energy bands in $CH_3NH_3PbI_3$ relative to isolated *p* and *s* atomic orbital energies of Pb and I. The $CH_3NH_3^+$ cation does not introduce states at the band edge. Reprinted with permission from ref 68. Copyright 2014 The Royal Society of Chemistry. (c) Dynamics of $CH_3NH_3^+$ cations generating distortions in the PbI_6 octahedra. Reprinted with permission from refs 69 and 70. Copyright 2015 American Chemical Society and Copyright 2015 Nature Publishing Group. (d) Summary of $CH_3NH_3PbX_3$-based (X = I, Br, Cl) perovskites and space groups adopted as a function of temperature. Reprinted with permission from ref 71. Copyright 2016 The Royal Society of Chemistry.

Before starting to describe more complex mixed cation perovskite systems [e.g., (Rb/Cs/MA/FA)Pb(I/Br) or (MA/FA)Pb(I/Br)], we briefly outline our current understanding on structure−property relationship of simple perovskite systems (e.g., $MAPbI_3$ and $FAPbI_3$) and then gradually add one element (cation or halide) at a time and introduce the new properties of the material induced by the addition of this new element. $MAPbI_3$ is the most widely studied hybrid halide perovskite for photovoltaic applications[13,24−26,72] and therefore its fundamental properties were investigated most thoroughly.[12,14,67,73−82] At room temperature, the Goldschmidt's tolerance factor (*t*) of $MAPbI_3$ is 0.91[83,84] with ionic radii of Pb^{2+} = 0.132 nm, I^- = 0.206 nm, and MA^+ = 0.18 nm[7] suggesting the tetragonal phase, which was confirmed experimentally by $MAPbI_3$ single crystal X-ray diffraction (XRD) data.[7,9] It was reported that the PbI_6 octahedra in $MAPbI_3$ are corner connected and the MA^+ cations are filled in the octahedral interstices (Figure 2a).[67] According to density functional theory (DFT) calculations, the ions within the inorganic PbI_6 octahedra have electronic configuration of Pb: $5d^{10}6s^26p^0$ and I: $5p^6$. The Pb 6*s*6*p*−I 5*p* interactions are responsible for chemical bonding in PbI_6 octahedra and generation of two bands: the valence band maximum (VBM) is formed of an antibonding (σ^*) Pb 6*s*−I 5*p* interactions, while the conduction band minimum (CBM) is formed of empty Pb 6*p* orbitals[73] and/or from Pb 6*p*−I 5*p* interactions (Figure 2b).[68,72,85−87] The MA^+ molecular units form bonding (σ) states deep (5 eV below Fermi level) in the VBM and they do not hybridize with the PbI_6 octahedra near VBM or CBM. Therefore, the MA^+ cations were proposed to do not contribute directly toward the band structure, but play a major role providing structural stability by charge compensation within the PbI_6 octahedra based largely on electrostatic (van der Waals) interactions.[15,26,74] Because of this lack of electronic interaction between MA^+ and PbI_6^{4-}, free carriers in $MAPbI_3$ are likely to diffuse along the corner shared PbI_6 chains in the crystal lattice.[88,89] The VBM electrons that are photoexcited to CBM empty states determine the band gap (E_g) (Figure 2b).[85] A wide range of E_g values between 1.5 and 1.61 eV have been reported for $MAPbI_3$[14,15,80,90] with the E_g values generally higher for polycrystalline films possibly due to quantum confinement.[7,90] Because the optimal E_g for a single-junction solar cell is between 1.1 and 1.4 eV on the basis of the Shockley−Queisser limit,[91] efforts have been made to modify the $MAPbI_3$ structure.[14,15]

In addition, material instabilities have been widely reported.[28,29,92,93] It has been proposed that perovskites have

DOI: 10.1021/acsami.7b06001
ACS Appl. Mater. Interfaces XXXX, XXX, XXX−XXX

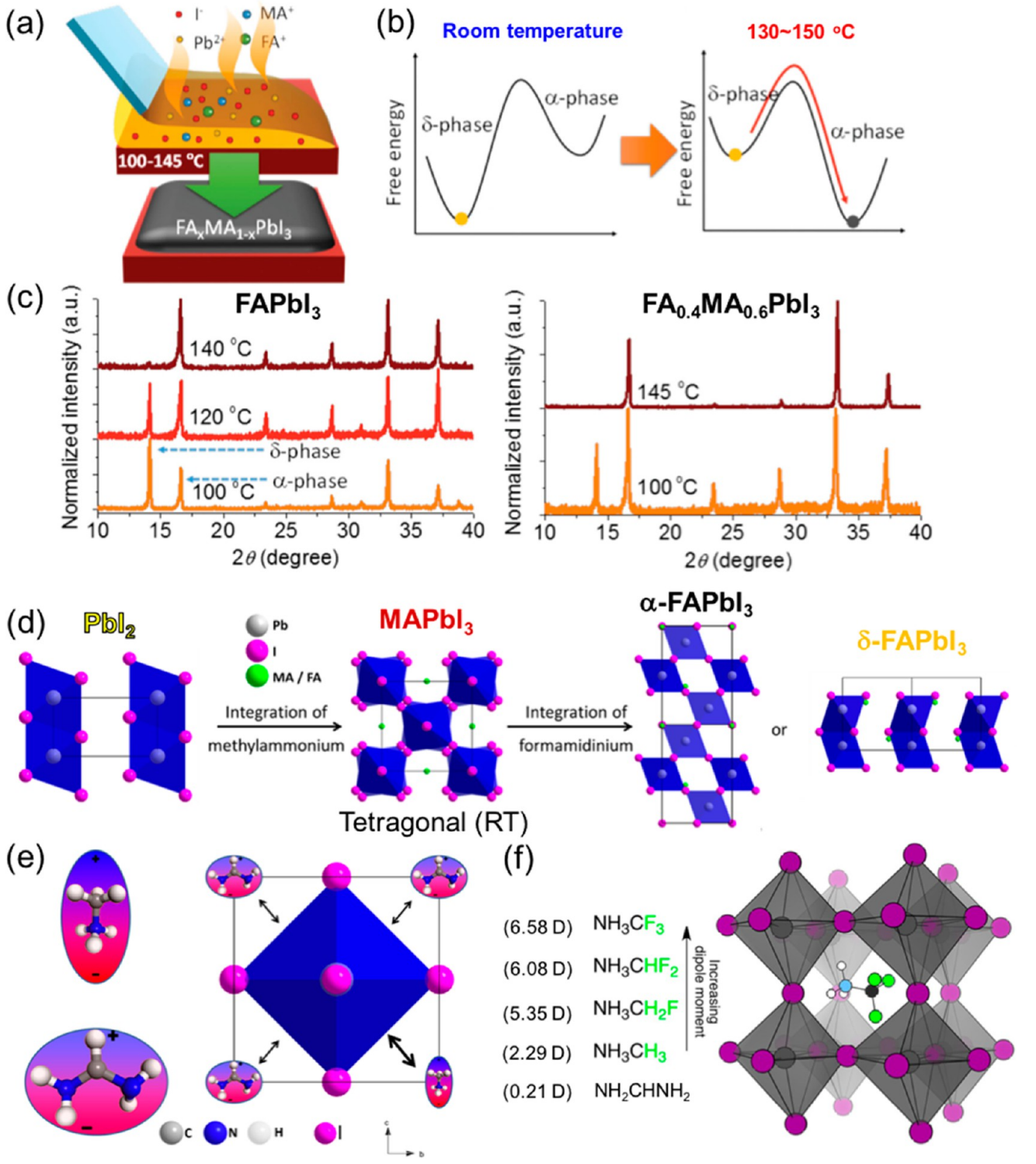

Figure 3. (a) Illustration of $MA_{0.6}FA_{0.4}PbI_3$ perovskite film formation by doctor-blade method. (b) Schematic diagrams of free energy versus α-phase and δ-phase of $FAPbI_3$ and $MA_xFA_{1-x}PbI_3$ perovskites. (c) XRD patterns for $FAPbI_3$ and $MA_xFA_{1-x}PbI_3$ perovskites as a function of annealing temperature. The reflection at $2\theta = 12°$ and 14° are correlated to δ- and α-phase of $FAPbI_3$, respectively. Reprinted with permission from ref 111. Copyright 2016 WILEY-VCH Verlag GmbH & Co. KGaA, Weinheim. (d) Crystal structures of PbI_2 where PbI_6 octahedra are connected via shared plane of three iodide ions. Incorporation of MA leads the layered octahedra to form a 3D $MAPbI_3$ network in tetragonal phase by reducing the number of shared iodide ions from three to one. Incorporation of <20% FA to $MAPbI_3$ leads the unit cell to expand while maintaining the tetragonal phase. With FA/MA >80% in the $MAPbI_3$ structure, the tetragonal phase collapses and the trigonal phase of α-$FAPbI_3$ is formed (3D network). However, at room temperature, the hexagonal phase of δ-$FAPbI_3$ can also be formed. (e) Schematic illustration of the mechanism for the $MA_xFA_{1-x}PbI_3$ stabilization based on the dipole moments of cations. Reprinted with permission from ref 106. Copyright 2015 American Chemical Society. (f) Theoretically calculated dipole moments for selected cations. Reprinted with permission from ref 114. Copyright 2014 American Chemical Society.

DOI: 10.1021/acsami.7b06001
ACS Appl. Mater. Interfaces XXXX, XXX, XXX−XXX

Table 1. Summary of Perovskite Solar Cell Performances Employing Mixed Cations and/or Halide Perovskites[a,b]

Solar cell architecture	Perovskite thickness (nm)	E_g (eV)	Electrode active area (cm^2)	J_{sc} (mA/cm^2)	V_{oc} (V)	FF (%)	PCE (%)	Hysteresis	Stability	ref.
FTO/c-TiO_2/mp-TiO_2/$MA_{0.6}FA_{0.4}PbI_3$/spiro/Au	~300 nm	1.53	0.285	18.15	1.027	71.5	13.4	–	–	102
ITO/PEDOT:PSS/$MA_{0.6}FA_{0.4}PbI_3$/PC61BM/Ca/Ag	~300 nm	–[c]	0.4	18.95	0.943	73.1	13.0	Hysteresis present.	–	109
FTO/c-TiO_2/$(MAPbI_3)(FAPbI_3)$/Au [No HTL]	–	1.53–1.54	0.09	9.58	0.77	54	4.0	–	–	103
FTO/c-TiO_2//$MA_{0.13}FA_{0.87}PbI_3$/spiro/Au	–	1.52 ± 0.02	0.0831	15.7	1	56	8.73	–	–	106
FTO/c-TiO_2/mp-TiO_2/$MA_{0.6}FA_{0.4}PbI_3$/spiro/Au	–[c]	–[c]	0.16	20.87	0.975	69.97	14.23	$MA_{0.6}FA_{0.4}$ shows small hysteresis; Other compositions show hysteresis.	Storage in air and dark; RH < 60%; 120 days.	104
ITO/PTAA/ $MA_{0.6}FA_{0.4}PbI_3$/ICBA/C_{60}/BCP/Cu [Doctor blade]	–[c]	1.55	–	23	1.03	77	18.3	Small hysteresis.	Storage in air; ~25 °C and RH 20%–60%; 30 days.	111
ITO/PEDOT:PSS/ $MA_{0.6}FA_{0.4}PbI_3$/$PC_{61}BM$/Ag	–	–	0.1	20.96 ± 0.14	0.979 ± 0.016	64.7 ± 1.2	13.28 ± 0.37	Small hysteresis.	–	110
FTO/c-TiO_2/mp-TiO_2/$MA_xFA_{1-x}PbI_3$/WO_3/Ag [CVD]	–	1.57	0.2	20.85	1.04	73.15	15.86	Negligible hysteresis.	Storage in air; 30 days.	112
FTO/ZnO/$MA_{0.6}FA_{0.4}PbI_3$/spiro/Ag	~315	–	0.045	22.39	0.984	60.66	13.4	Hysteresis present.	Storage in N_2; 21 days.	105
FTO/c-TiO_2/C60/$MA_{1-x}FA_xPbI_3$/spiro/Au [LP-VASP]	~340	1.55	0.09	22.51	1.00	73.56	16.48	Small hysteresis.	Storage in N_2; 288 h.	113
			1	17.12	0.88	52.80	8.00	Hysteresis present.	–	
FTO/c-TiO_2/mp-TiO_2/$MA_{0.25}FA_{0.75}PbI_3$/spiro/Ag	~300	~1.545	–	21.10	1.03	71.38	15.51	Hysteresis present.	–	107
FTO/c-TiO_2/$MA_{0.7}FA_{0.3}PbI_3$/spiro/Ag	–	–	–	22.03	1.03	75	17.02	Hysteresis present.	–	108
ITO/PEDOT:PSS/ $MA_{0.9}Cs_{0.1}PbI_3$/PC60BM/Al	38 ± 9	1.54	0.13	10.10	1.05	73	7.68	–	Storage in air; ~20 °C and RH 11%; 42.5 h.	115
FTO/c-TiO_2/mp-TiO_2/$MA_{0.91}Cs_{0.09}PbI_3$/spiro/Au	~400	–[c]	0.09	22.57	1.06	76	18.1	Hysteresis present.	Storage in air; ~85 °C; 1 h.	116
FTO/c-TiO_2/$Cs_{0.1}FA_{0.9}PbI_3$/spiro/Ag or Au	–[c]	1.55	0.125	23.5	1.06	66.3	16.5[d]	Hysteresis present.	Test 1: Exposure to white light; Sample temperature ~60 °C; RH < 50%. Test 2: Storage in dark; 25 °C; RH 85%.	100
FTO/c-TiO_2/$Cs_{0.15}FA_{0.85}PbI_3$/spiro/Ag	–	1.52	–	20.39	1.06	74	16.1[d]	Hysteresis present.	Storage in a desiccator and dark; RH 15%; 350 h.	101
FTO/c-TiO_2/ mp-TiO_2/$Cs_{0.2}FA_{0.8}PbI_3$/spiro/Au	–	1.56	0.16	21.5	1.017	70.1	15.69	–	Storage in air; 1000 h.	117
FTO/c-SnO_2/C60-SAM/$Cs_{0.2}FA_{0.8}PbI_3$/spiro/Au	~435	–[c]	0.08	21.73 ± 0.51	1.03 ± 0.02	72.37 ± 1.18	16.18 ± 0.50[d] [Reverse]	Hysteresis present.	Storage in a drybox under room light; 10 days.	118
FTO/c-SnO_2/C60-SAM/$Cs_{0.2}FA_{0.8}PbI_3$ + **0.5 mol % $Pb(SCN)_2$**/spiro/Au		–[c]		21.94 ± 0.31	1.06 ± 0.01	77.77 ± 1.51	18.16 ± 0.54[d] [Reverse]			
FTO/c-TiO_2/$Cs_xFA_{1-x}PbI_3$/spiro/Ag (x not determined)	–[c]	–[c]	0.12	20.4	1.09	74	16.4	Hysteresis present.	Storage in air; ~25 °C and RH ~ 40%; 4 h.	119
FTO/NiO/ $Cs_{0.15}FA_{0.85}PbI_3$/PC61BM/PFN-Br/Ag	–[c]	–[c]	0.09	20.81	1.035	71.4	15.38	–	–	120
FTO/c-TiO_2/mp-TiO_2/$Rb_{0.05}FA_{0.95}PbI_3$/spiro/Au	~480 (capping layer)	1.53	–	23.93	1.07	67	17.16	Smaller hysteresis compared to $FAPbI_3$.	Storage in air; ~25 °C and RH ~ 55%; 1000 h.	121
FTO/c-TiO_2/mp-TiO_2/$Rb_{0.05}FA_{0.95}PbI_3$/spiro/Au	–	–[c]	0.65	23.8	1.03	65.9	16.2	–	Storage in air; ~25 °C and RH ~ 55%; 4 weeks.	122

ACS Appl. Mater. Interfaces XXXX, XXX, XXX−XXX
DOI: 10.1021/acsami.7b06001

Table 1. continued

Solar cell architecture	Perovskite thickness (nm)	E_g (eV)	Electrode active area (cm^2)	J_{sc} (mA/cm^2)	V_{oc} (V)	FF (%)	PCE (%)	Hysteresis	Stability	ref.
FTO/c-TiO_2/ mp-TiO_2/ **$Cs_{0.2}FA_{0.8}PbI_{2.84}Br_{0.16}$**/spiro/Au	–	1.58	0.16	21.9	1.073	74.2	17.35	–	Storage in air; 1000 h.	117
FTO/c-TiO_2/ mp-TiO_2/(**MAPbI$_3$**)$_{1-x}$(**CsPbBr$_3$**)$_x$/spiro/Au	360	–[c]	0.09	20.9 ± 0.42	1.07 ± 0.01	71 ± 2	15.9 ± 0.52	Small hysteresis	(1) Degradation test of unencapsulated devices under UV light (365 nm, 364 mW/cm^2) (2) Stability of unencapsulated devices in ambient air (25 °C, 20–30% RH)	123
FTO/Nb-TiO_2/$FA_{0.84}MA_{0.16}Pb(I_{0.84}Br_{0.16})$/ spiro/Au	~500	–[c]	0.12	23.4	1.006	74	17.6	–	2000 h aging test.	124
FTO/c-TiO_2/mp-TiO_2/$FAPbI_3$-MABr/spiro/ Au	~450	–	0.096	22.17	1.07	67.38	15.98	Small hysteresis	Storage in air (~50% RH, 23 °C) without encapsulation for 1000 h.	125
			0.48	22.14	1.04	63.38	14.59			
ITO/PEDOT:PSS/(FAPbI$_3$)$_{0.8}$(MAPbBr$_3$)$_{0.2}$/C60/BCP/Ag	~280[c]	–	0.1	20.6	0.88	65.9	12	–	–	126
FTO/c-TiO_2/mp-TiO_2/$(FAPbI_3)_{0.85}$Pb $(MABr_3)_{0.15}$/spiro/Au	mp-TiO_2 with PVSK infiltrated (~200 nm) + capping layer (~650 nm)	1.57–1.58	0.126	22.5	1.13	69	17.6	Yes	—	127
FTO/c-TiO_2/mp-TiO_2/(FA/MA)Pb(I/Br)$_3$/ spiro/Au	mp-TiO_2 with PVSK infiltrated (~150 nm) + capping layer (~400 nm)	–	0.36	21	1.01	69	14.5	Small hysteresis	ISOS-O-2 protocol for 1000 h.	128
ITO/PEDOT:PSS/(FAPbI$_3$)$_{0.8}$(MAPbBr$_3$)$_{0.2}$/C60/BCP/Ag	–	–[c]	0.1	20.1 ± 0.5	0.87 ± 0.01	66.4 ± 1.2	11.8 ± 0.20	Small hysteresis	–	129
FTO/c-TiO_2/mp-TiO_2/(FA/MA)Pb(I/Br)$_3$/ spiro/Au PbI_2:FAI = 1.05 (PbI_2 excess)	~400[c]	1.6	0.16	24.6	1.16	73	20.8	No hysteresis	Sealed cells using epoxy and stored in a desiccator in dark for 1 month.	130
FTO/c-TiO_2/mp-TiO_2/$FA_{4/6}MA_{2/6}Pb$ $(I_{5/6}Br_{1/6})$/spiro/Au	~400[c]	1.64	0.16	23.7	1.14	76	20.67	Hysteresis varies according to composition.	–	90
ITO/PEDOT:PSS/$MA_{0.80}FA_{0.20}PbI_{3-y}Cl_y$/ PC61BM/C60/LiF/Ag	~280	1.58	0.11	21.55 ± 0.55	1.10 ± 0.01	75 ± 2	17.45	No hysteresis when $MA_{0.80}FA_{0.20}PbI_{3-y}Cl_y$ is annealed below 110 °C.	–	131
FTO/SnO_2/PC60BM/$FA_{0.83}Cs_{0.17}Pb$ $(I_{0.6}Br_{0.4})_3$/spiro/Ag	–[c]	1.74	0.0919	19.4	1.2	75.1	17.1	–	–	132
	–[c]		0.715	19.5	1.19	67.8	14.7			
ITO/NiO/$FA_{0.83}Cs_{0.17}Pb(I_{0.6}Br_{0.4})_3$/LiF/ PC60BM/$SnO_2$/ZTO/ITO/LiF/Ag	–	1.63	1	18.7	0.98	78.8	14.5	–	single-junction perovskite device with no additional encapsulation during 1000 h of continuous maximum-power-point tracking	133
FTO/SnO_2/C60/$Cs_{0.17}FA_{0.83}Pb(I_{0.6}Br_{0.4})$/ spiro/Au	–	–	0.0919	23	1.06	75	18.3	–	Aged under full AM1.5 spectrum at V_{oc} in air without UV filter.	134
FTO/c-TiO_2/mp-TiO_2/ $Cs_{0.2}FA_{0.8}PbI_{2.84}Br_{0.16}$/spiro/Au	–	1.49	0.16	21.9	1.073	74.2	17.35	–	Storage in air; 1000 h.	117
FTO/c-TiO_2/mp-TiO_2/ $Cs_{0.05}(FA_{0.83}MA_{0.17})_{0.95}Pb(I_{0.83}Br_{0.17})_3$/ spiro/Au	~500[c]	1.6[c]	0.16	22.69 ± 0.75	1.132 ± 0.025	74.8 ± 1.8	19.2 ± 0.91	Yes	Under constant illumination and maximum power tracking for 250 h; Cells held at room temperature.	65
FTO/c-TiO_2/mp-TiO_2/$Cs_{0.1}FA_{0.8}MA_{0.0.1}Pb$ $(I_{0.83}Br_{0.17})_3$/spiro/Au	~500	–[c]	0.16	21.5	1.155	73	18.1	Yes	300 h storage; dry air and in dark.	135
FTO/SnO_2/$Cs_{0.1}FA_{0.8}MA_{0.0.1}Pb(I_{0.83}Br_{0.17})_3$/ spiro/Au				22.4	1.129	68	17.3	Yes	–	
FTO/c-TiO_2/mp-TiO_2/ $Rb_x(FAPbI_3)_{1-y}(MAPbBr_3)_y$/PTAA/Au 15% PbI_2 excess 5% RbI doping	–[c]	–[c]	0.16	22.86 ± 0.37	1.123 ± 0.011	69.6 ± 1.9	17.68 ± 0.91	Exhibit some degree of hysteresis	(1) Under continuous light illumination; cells kept under ambient conditions (40–50% RH, 25 °C).	136

ACS Appl. Mater. Interfaces XXXX, XXX, XXX−XXX
DOI: 10.1021/acsami.7b06001

Table 1. continued

Solar cell architecture	Perovskite thickness (nm)	E_g (eV)	Electrode active area (cm^2)	J_{sc} (mA/cm^2)	V_{oc} (V)	FF (%)	PCE (%)	Hysteresis	Stability	ref.
									(2) Steady-state efficiency tracking maximum power point under N_2 environment.	
FTO/c-TiO_2/mp-TiO_2/ **$Rb_{0.05}FA_{0.8}MA_{0.15}PbI_{2.55}Br_{0.45}$**/spiro/Au	–	–[c]	0.5	22.5	1.168	74.7	19.6	–	Storage in air; ∼25 °C and RH ∼55%; 4 weeks.	122
FTO/c-TiO_2/mp-TiO_2/$Rb_{0.05}Cs_{0.10}FA_{0.85}Pb(I_{0.83}Br_{0.17})_3$/spiro/Au	–	–	0.16	22.3	1.157	75	19.3	Yes	–	137
FTO/c-TiO_2/mp-TiO_2/$Rb_{0.05}Cs_{0.05}(FA_{0.83}MA_{0.17})_{0.90}Pb(I_{0.83}Br_{0.17})_3$/PTAA/Au	∼500	1.63	0.16	22.8	1.180	81	21.8	Yes	Device aged for 500 h at 85 °C under continuous full illumination and maximum power tracking in a nitrogen atmosphere.	
			0.5	>20[c]	>1.15[c]	–	17.4 (steady state power)	–	–	
FTO/c-TiO_2/mp-TiO_2/Rb(5%) in $FA_{0.75}(MA_{0.6}Cs_{0.4})_{0.25}PbI_2Br$/PTAA/Au	mp-TiO_2 with PVSK infiltrated (∼180 nm) + capping layer (∼400 nm)	1.73	0.1764	18.3	>1.1[c]	–[c]	17.4 (steady state power)	Negligible	(1) Light stability for 12 h under continuous 1 sun illumination and applied maximum power point voltage in N_2 environment with (controlled 25 °C). (2) 12 h−light/dark cycles.	138

[a]Perovskite thickness, bandgap (E_g), electrode active area, solar cell parameters of short-circuit current (J_{sc}), open-circuit voltage (V_{oc}), fill factor (FF), and power conversion efficiency (PCE) are indicated. Additional notes on hysteresis and stability are indicated. [b]Abbreviations: ITO = indium tin oxide; FTO = fluorine doped tin oxide; polyTPD = poly(*N*,*N*′-bis(4-butylphenyl)-*N*,*N*′-bis(phenyl)benzidine); c-TiO_2 = compact layered TiO_2; spiro-MeOTAD = 2,7′-7,7′-tetrakis(*N*,*N*-di-*p*-methoxyphenylamine)-9,9′-spirobifluorene; PTAA = poly[bis(4-phenyl)(2,4,6-trimethylphenyl)amine]; PEDOT:PSS = poly(3,4-ethylenedioxythiophene):poly(styrenesulfonate); ICBA = indene-C60 bisadduct; BCP = 2,9-dimethyl-4,7-diphenyl-1,10-phenanthroline; PC60BM = [6,6]-phenyl-C60 butyric acid methyl ester; PC61BM = [6,6]-phenyl C61 butyric acid methyl ester; PFN-Br = poly[(9,9-bis(3′-((*N*,*N*-dimethyl)-*N*-ethylammonium)propyl)-2,7-fluorene)-*alt*-2,7-(9,9-dioctylfluorene)]dibromide. C60-SAM = fullerene-self-assembled-monolayer. $Pb(SCN)_2$ = lead(II) thiocyanate. PFN-Br = poly[(9,9-bis(3′-((*N*,*N*-dimethyl)-N-ethylammonium)propyl)-2,7-fluorene)-*alt*-2,7-(9,9-dioctylfluorene)] dibromide. ZTO = zinc tin oxide. [c]Thickness and absorption measured, but values not explicitly stated. [d]Averaged values based on forward and reverse scans reported.

ACS Appl. Mater. Interfaces XXXX, XXX, XXX−XXX
DOI: 10.1021/acsami.7b06001

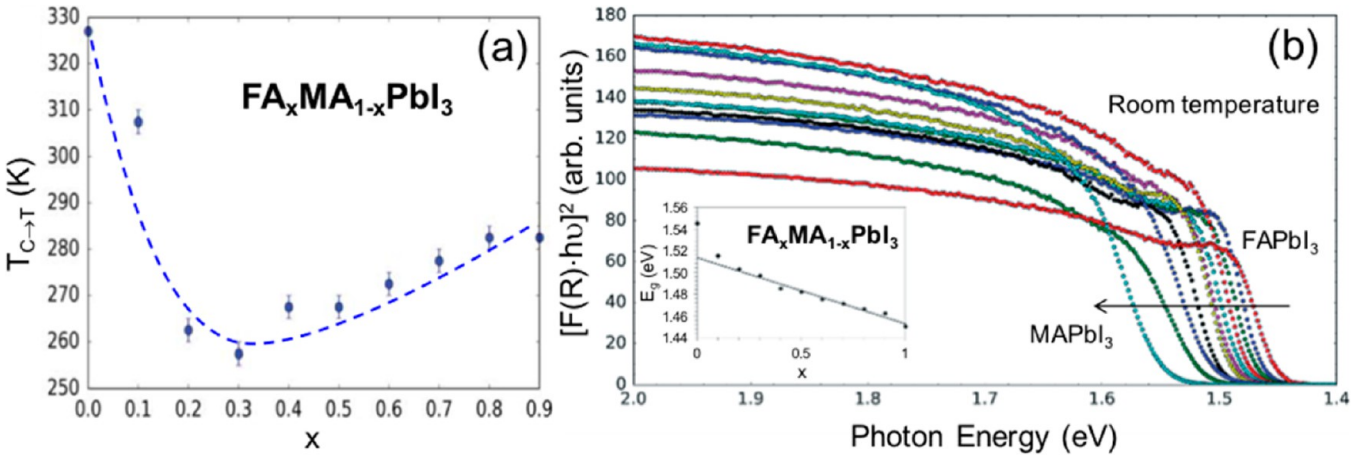

Figure 4. (a) Phase transition temperatures from cubic to tetragonal ($T_{C\to T}$) and (b) Tauc plots of UV−vis reflectance spectra measured at room temperature and (inset) extracted band gap (E_g) of $FA_xMA_{1-x}PbI_3$ ($0 \le x \le 1$) perovskites. Reprinted with permission from ref 83. Copyright 2016 The Royal Society of Chemistry.

an inherently "soft" structure ("plastic crystals"[94]) and therefore several dynamical phenomena characterized by different time scales exist in perovskites (from femtosecond up to minutes) influencing strongly on the overall optoelectronic properties (e.g., energy levels, bandgap, balanced/imbalanced charge transport, etc.) of perovskites (Figure 2c).[69,70,95−97] Furthermore, $MAPbI_3$ undergoes a phase transition from the tetragonal to cubic phase at ∼54 °C (Figure 2d), a temperature that is of relevance during typical solar cell operation.[9,49] Therefore, it is imperative to develop perovskites insensitive to composition instabilities under stress conditions for solar cell operation. For certification, solar modules must operate successfully in the temperature range between −40 and +85 °C.[98] In contrast to $MAPbI_3$, $FAPbI_3$ was reported to be free from phase transition between a wide temperature range from 25 to 150 °C.[99,100] Chemical compositional engineering[63] (or alloying[8,101]) was shown to be an effective strategy (e.g., substitution of MA^+ by other cations such as FA^+, Cs^+, Rb^+, Figure 1c) to further enhance the optoelectronic properties of $MAPbI_3$ as evidenced by reported certified efficiencies (Figure 1b).[5,7,90]

2. MIXED A CATIONS

2.1. Binary (FA/MA)PbI_3 System. Perturbing the A cation size can influence the optical properties by deforming the BX_6 octahedron network. A larger (e.g., FA^+ = 0.19−0.22 nm) or smaller (e.g., Cs^+ = 0.167 nm, Rb^+ = 0.152 nm) cation causes the lattice to expand or contract leading to the change of B−X bond length, which has been shown to influence E_g.[7] Pellet et al. reported the first mixed A cation describing the bandgap tunability of $MA_xFA_{1-x}PbI_3$-based solar cells by varying the ratio of MA to FA.[102] The MA/FA mixed perovskites were synthesized by dipping the predeposited PbI_2 with premixed $MA_xFA_{1-x}I$ solution in isopropanol. They showed that the $MA_{0.6}FA_{0.4}PbI_3$ composition resulted in the best PCE of 13.4% (Table 1) with the absorption edge extending up to ∼810 nm (E_g ∼ 1.53 eV), which was also similar to the pure $FAPbI_3$ perovskite. Later several works have been published showing better $MA_xFA_{1-x}PbI_3$ film quality (higher film coverage, fewer pin-holes, higher crystal quality, larger grain sizes, smaller roughness within the grains, and alternative selective contacts),[103−108] employing inverted structure,[109,110] and using perovskite deposition techniques other than spin-coating (Table 1),[111−113] such as doctor blading (Figure 3a),[111] chemical vapor deposition (CVD),[112] and low-pressure vapor-assisted solution process (LP-VASP)[113] (Table 1). Based on Table 1, among optimized MA/FA ratios, there is a consensus that $MA_{0.6}FA_{0.4}PbI_3$ composition results in the best PCE as high as 18.3%.[111] Deng et al.[111] employed additionally Cu as the top electrode in their devices and observed high device performances. Chen et al.[113] reported devices with larger active area of 1 cm^2 generating PCE of 8%, while their smaller cells (0.09 cm^2) generated PCE of 16.48%.

The highest PCE for $MAPbI_3$ solar cells in a standard device architecture was reported to reach ∼20%,[139,140] whereas in an inverted structure, the highest PCE of 18.1% was reported.[141] Up to now, employing complex strategies (e.g., solvent-engineering, $HPbI_3$ precursor, organic-cation displacement), the best PCE reported for $FAPbI_3$ perovskite solar cells reached 13.5−18%, which is somehow lower than the $MAPbI_3$-based ones.[64,99,142−144] Because of the larger ionic radius of FA^+ compared to MA^+, $FAPbI_3$ perovskites are expected to have a smaller E_g (1.47 to 1.55 eV depending on the fabrication methods[145]) compared to $MAPbI_3$.[99,143,146,147] As the consequence, higher PCE would be expected for $FAPbI_3$ solar cells as light harvesting range extends further into the near-infrared. Comparative works have shown that the short-circuit current (J_{sc}) of $FAPbI_3$ devices is higher than that of $MAPbI_3$, confirming the ability of extended light-absorption of $FAPbI_3$ perovskites. The main loss in PCE comes from the poor fill factor (FF).[143,148] Several studies proposed that there is a fundamental limitation associated with the phase instability of the pure $FAPbI_3$ in ambient conditions (either in the form of polycrystalline film[8,63,106,149] or single crystal[150]). As a matter of fact, $FAPbI_3$ possess two polymorphs (Figure 3b−d).[8,82,106,119,149−151] $FAPbI_3$ crystallizes at room temperature as (i) photoinactive nonperovskite, hexagonal δ-$FAPbI_3$ perovskite ("delta or yellow phase", space group $P6_3mc$[82]) formed from face-sharing PbI_6 octahedra (Figure 3d), and (ii) photoactive trigonal α-$FAPbI_3$ perovskite ("alpha or black phase", space group $P3m1$[82] or $Pm\bar{3}m$[149]) formed at higher temperatures, ∼125−165 °C (Figure 3d).[65,82,101,111,121] Similar polymorphism was reported for α,δ-$CsPbI_3$ system.[65,121] After α-$FAPbI_3$ is formed, a slow phase transformation to δ-$FAPbI_3$ is reported when kept at room temperature, which leads to unstable device operation.[8,111] It is interesting to note that the incorporation of MA^+ into $FAPbI_3$ structure results in a much

DOI: 10.1021/acsami.7b06001
ACS Appl. Mater. Interfaces XXXX, XXX, XXX−XXX

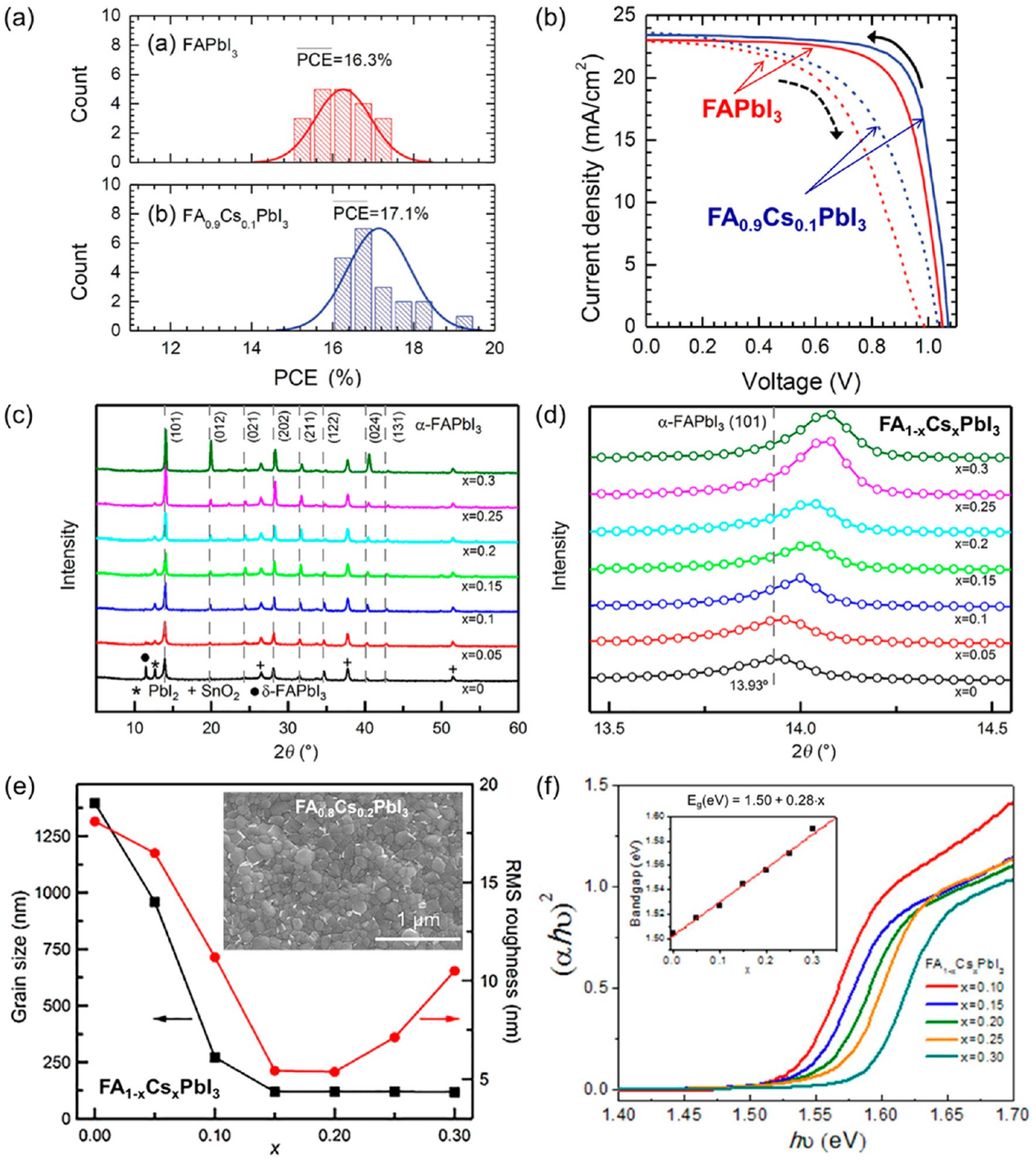

Figure 5. (a) Statistical distribution of perovskite solar cell PCE based on $FAPbI_3$ (red) and $FA_{1-x}Cs_xPbI_3$ (blue) and (b) $J-V$ curves of the best performing devices for $FAPbI_3$ (red) and $FA_{1-x}Cs_xPbI_3$ (blue) at reverse scans (solid lines) and forward scans (dotted lines). Reprinted with permission from ref 100. Copyright 2015 WILEY-VCH Verlag GmbH & Co. KGaA, Weinheim. (c,d) XRD patterns and (e) grain size and surface RMS roughness of $FA_{1-x}Cs_xPbI_3$ with x = 0 to 0.30. Reprinted with permission from ref 118. Copyright 2016 WILEY-VCH Verlag GmbH & Co. KGaA, Weinheim. (f) Tauc plots and extracted band gaps (E_g, inset) for $FA_{1-x}Cs_xPbI_3$ with x = 0 to 0.30. Reprinted with permission from ref 101. Copyright 2015 American Chemical Society.

more stable $MA_xFA_{1-x}PbI_3$ perovskite structure,[83,152,153] its origins of which were further investigated by Binek et al.[106] It has been proposed that the incorporation of a smaller cations (MA^+) with a large dipole moment exhibits stronger interaction with the PbI_6 octahedra, which stabilizes the 3D arrangement of α-$FAPbI_3$ with little lattice shrinkage or changes in the optical properties (Figure 3e). MA^+ has a dipole moment ten times higher than that of FA^+ (Figure 3f).[114] Similarly, based on DFT

DOI: 10.1021/acsami.7b06001
ACS Appl. Mater. Interfaces XXXX, XXX, XXX−XXX

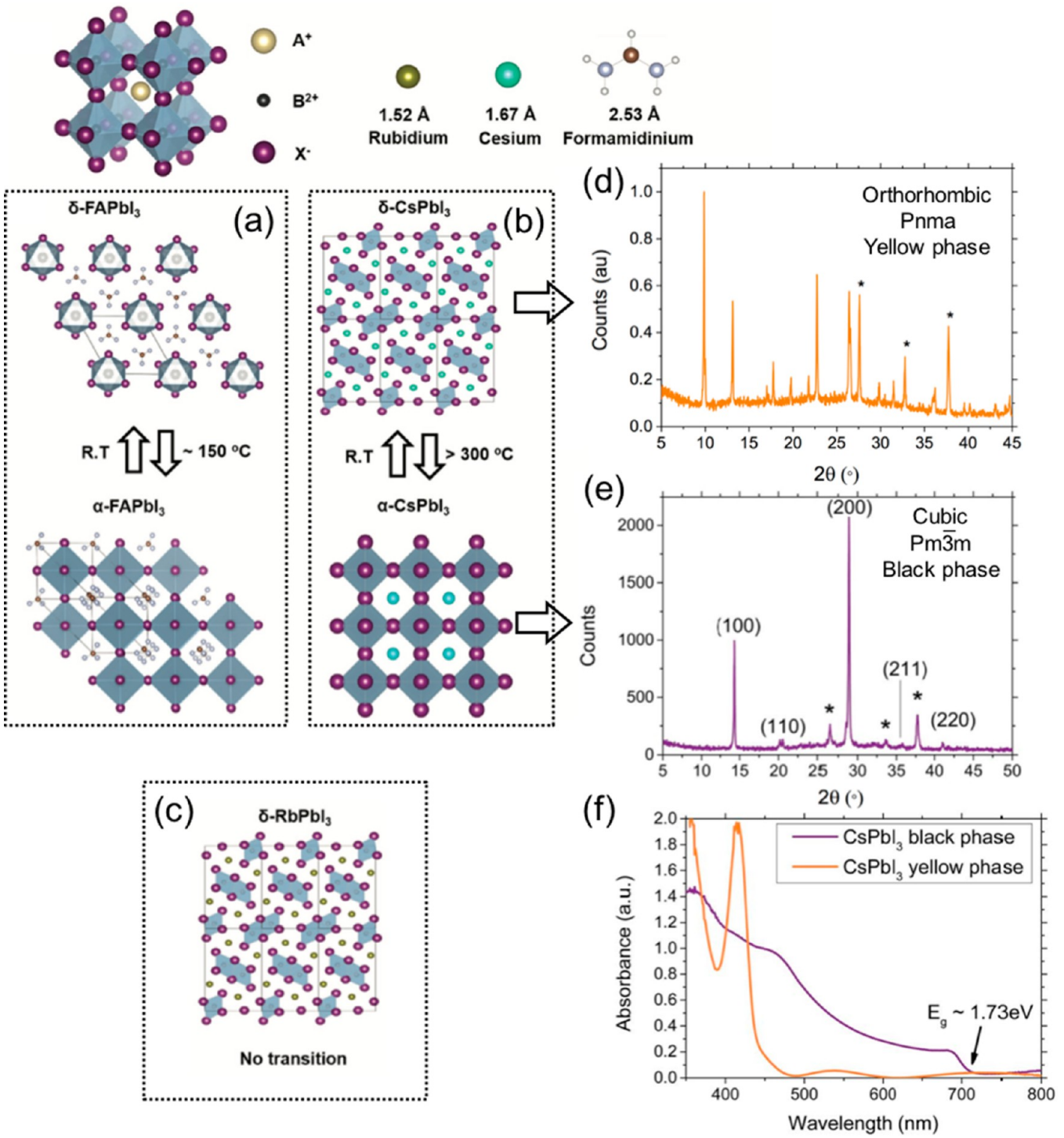

Figure 6. Illustration of ABX_3 perovskite crystal structure and possible candidates for the A-site cation (FA^+, Cs^+, Rb^+) with corresponding ionic radius. (a) Schematic representations of the polymorphs in (b) α,δ-$FAPbI_3$ and (c) α,δ-$CsPbI_3$ perovskites. The $\alpha \rightarrow \delta$ phase transitions for $CsPbI_3$ is much higher than in $FAPbI_3$. At room temperature, the δ-phases are preferentially stabilized. Reprinted with permission from ref 121. Copyright 2017 WILEY-VCH Verlag GmbH & Co. KGaA, Weinheim. (d) XRD of $CsPbI_3$ thin film in yellow phase and (e) black phase. Peaks with * correspond to the FTO substrate. (f) Absorbance spectra of black and yellow phases of $CsPbI_3$ thin films. The measurements were done in air, with the black phase perovskite coated with poly methyl methacrylate (PMMA) to minimize transformation into the yellow phase. Reprinted with permission from ref 155. Copyright 2015 The Royal Society of Chemistry.

calculations El-Mellouhi et al.[154] proposed that $CH_3PH_3^+$, $CH_3SH_2^+$, and SH_3^+ cations could also result in stronger cohesion between PbI_6 octahedra and A cation within the crystal and attain enhanced stability while maintaining a suitable bandgap for solar cell applications. As described later in section 2.3, Cs^+ that has no dipole moment also helps stabilize the α-$FAPbI_3$ phase. The transition from tetragonal $MAPbI_3$ to trigonal α-$FAPbI_3$ is observed when the FA^+/MA^+ ratio in the structure is >80%.[106] The phase transition behavior as a function of $FA_xMA_{1-x}PbI_3$ ($0 \leq x \leq 1$) composition and

DOI: 10.1021/acsami.7b06001
ACS Appl. Mater. Interfaces XXXX, XXX, XXX−XXX

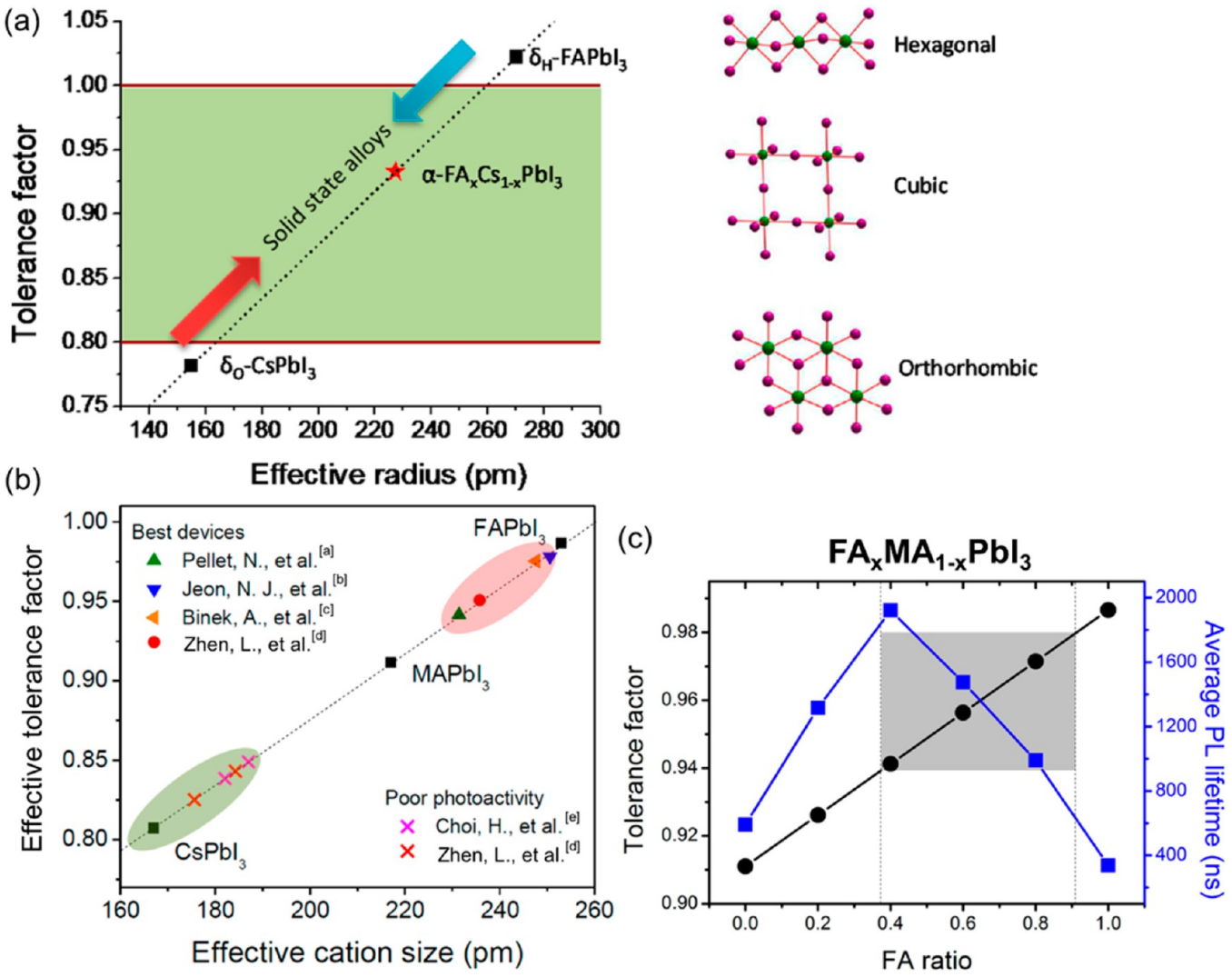

Figure 7. (a) Goldschmidt tolerance factor as empirical index for predicting stable perovskite crystal structure. Tolerance factor between 0.8 and 1.0 (green area) is favorable for cubic perovskite structure, and larger (>1) or smaller (<0.8) values generate nonperovskite structures. (b) Summary of the effective tolerance factors of different mixed perovskite alloys from the literature. [a] $MA_{0.6}FA_{0.4}PbI_3$,[102] [b] $(FAPbI_3)_{1-x}(MAPbBr_3)_x$ (x = 0.15),[63] [c] $MA_{0.13}FA_{0.87}PbI_3$,[106] [d] $Cs_{0.15}FA_{0.85}PbI_3$,[101] [e] $MA_{0.9}Cs_{0.1}PbI_3$.[115] Reprinted with permission from ref 101. Copyright 2016 American Chemical Society. (c) Correlation between Goldschmidt tolerance factor (black circles) and PL (blue squares) of the mixed cation $FA_xMA_{1-x}PbI_3$ perovskites. Reprinted with permission from ref 152. Copyright 2016 American Chemical Society.

temperature (150 K ≤ T ≤ 300 K) was investigated experimentally by Weber et al.[83] At 300 K, the $FA_xMA_{1-x}PbI_3$ with 0.2 ≤ x ≤ 1 composition revealed a cubic structure with unit cell dimensions of ∼6.3 Å. However, the tetragonal phase was observed for $MAPbI_3$ (x = 0) and $FA_{0.1}MA_{0.9}PbI_3$ (x = 0.1) perovskites. Their summary data (Figure 4a) extracted from variable temperature single crystal XRD measurements show a nonmonotonic behavior of the phase transition temperatures from cubic to tetragonal ($T_{C\rightarrow T}$). Starting from x = 0 ($MAPbI_3$) showing $T_{C\rightarrow T}$ ∼ 327 K, $T_{C\rightarrow T}$ decreased sharply reaching ∼257 K at x = 0.3. Subsequent increase in the FA (0.3 ≤ x ≤ 0.9) content leads to a slow steady increase in $T_{C\rightarrow T}$ ∼ 298 K at x = 0.9 (Figure 4a). UV−vis measurements on $FA_xMA_{1-x}PbI_3$ (0 ≤ x ≤ 1) revealed a linear decrease in the optical band gap with increase in the FA content from 0.2 ≤ x ≤ 1 (Figure 4b), corresponding to the range of compositions adopting the cubic unit cell at room temperature. $MAPbI_3$ (x = 0) and $FA_{0.1}MA_{0.9}PbI_3$ (x = 0.1) showed deviation from the linear trend due to the tetragonal structure stabilized at room temperature.

2.2. Binary $(MA/Cs)PbI_3$ System. To the best of our knowledge, there are only two reports about the $(MA/Cs)PbI_3$ system. The first study was conducted by Choi et al.,[115] in which they optimized $Cs_xMA_{1-x}PbI_3$ devices with x = 0.1 (inverted structure: ITO/PEDOT:PSS/$Cs_{0.1}MA_{0.9}PbI_3$/PCBM/Al) achieved a PCE of 7.68%. The second study was performed by Niu et al.[116] reporting a higher efficiency (reverse scan) of 18.1% in their optimized $Cs_xMA_{1-x}PbI_3$ devices with x = 0.09 (regular structure: FTO/c-TiO_2/mp-TiO_2/$Cs_{0.09}MA_{0.91}PbI_3$/Spiro-MeOTAD/Au) (Table 1). When the PCEs of $Cs_xMA_{1-x}PbI_3$ devices are compared to their individual reference cells, i.e., $MAPbI_3$, both studies observed increase of ∼20%[115] and ∼15%,[116] respectively. Although, the phase transitions for $(MA/Cs)PbI_3$ system were not studied, Niu et al.[116] showed better thermal stability of $Cs_xMA_{1-x}PbI_3$ with x = 0.09 and x = 0.20 than that of $MAPbI_3$. Contrary to MA^+ (section 2.1), which has a large dipole moment, Cs^+

DOI: 10.1021/acsami.7b06001
ACS Appl. Mater. Interfaces XXXX, XXX, XXX−XXX

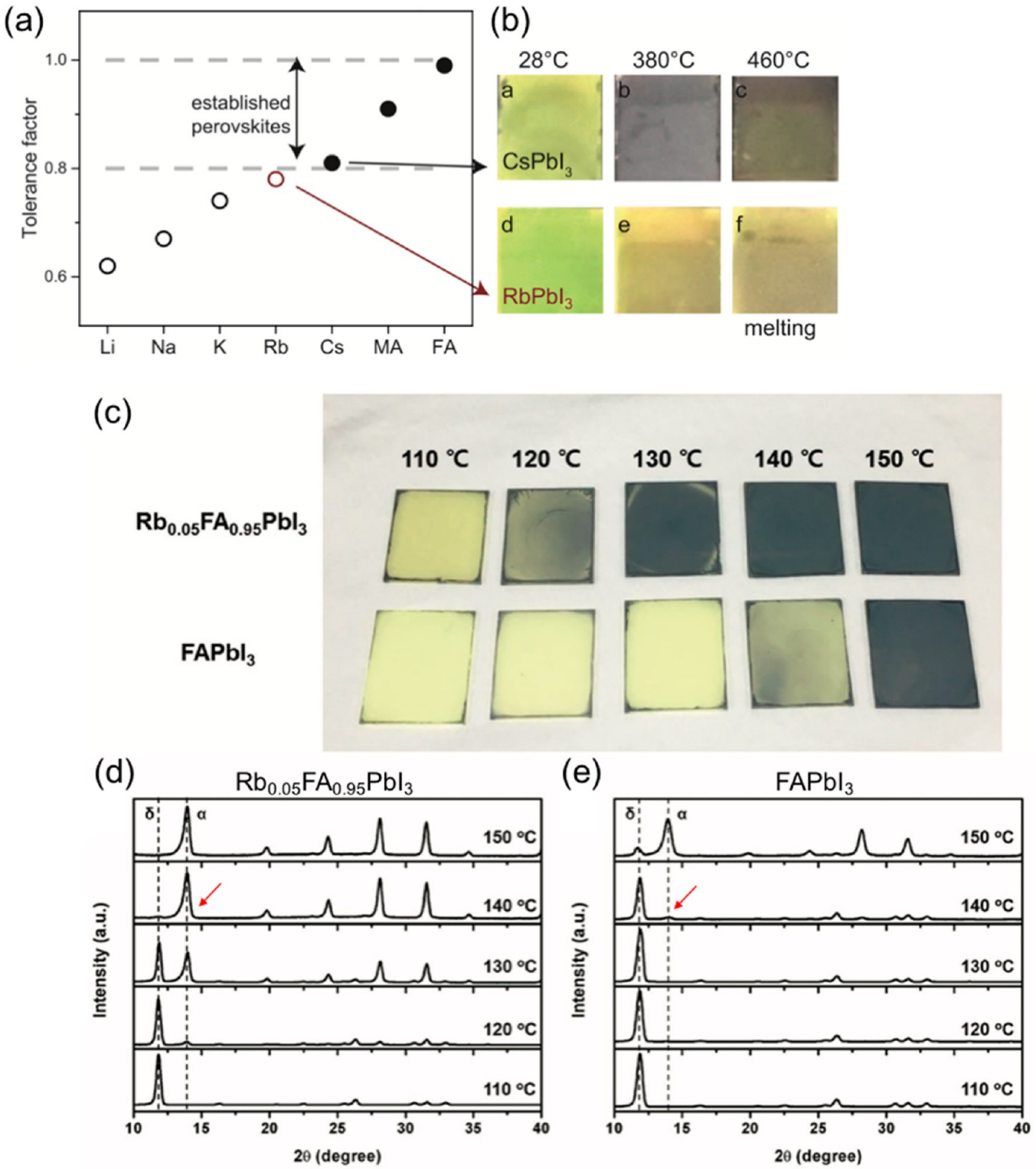

Figure 8. (a) Goldschmidt tolerance factor of $APbI_3$ (A = Li, Na, K, Rb, Cs, MA, FA) perovskites. Empirically, perovskites with a tolerance factor between 0.8 and 1.0 (dashed lines) show a photoactive black phase (solid circles) as opposed to nonphotoactive phases (open circles). Rb (red open circle) is very close to this limit. (b) $CsPbI_3$ and $RbPbI_3$ at 28, 380, and 460 °C. Irreversible melting occurs at 460 °C. $RbPbI_3$ never shows a black phase. Reprinted with permission from ref 137. Copyright 2016 American Association for the Advancement of Science (AAAS). (c) Photographs and XRD patterns of (d) $Rb_{0.05}FA_{0.95}PbI_3$ and (e) $FAPbI_3$ films after heating at specified temperatures for 5 min. Diffraction peaks corresponding to α- and δ-$FAPbI_3$ are indicated. Reprinted with permission from ref 121. Copyright 2016 WILEY-VCH Verlag GmbH & Co. KGaA, Weinheim.

cation (ionic radius = 0.167−0.181 nm) has no dipole moment, therefore it would be interesting to study the fundamental aspects of stabilization of MA/Cs and FA/Cs combinatorial systems.

2.3. Binary (FA/Cs)PbI_3 System. The number of reports on (FA/Cs)PbI_3 system is also scarce (Table 1).[100,101,118−120] In all these studies, similar to the $Cs_xMA_{1-x}PbI_3$ case, it is noticed that $Cs_xFA_{1-x}PbI_3$ with Cs quantities in the range of x

DOI: 10.1021/acsami.7b06001
ACS Appl. Mater. Interfaces XXXX, XXX, XXX−XXX

= 0.1 to 0.2 shows some enhancement in PCEs when compared to pure $FAPbI_3$ (Table 1, Figure 5a). These enhancements in PCEs can go as high as ~5%,[100] ~13%,[101] ~16%.[118] Hysteresis phenomena (Figure 5b) are present in all these studies employing devices with a standard structure of (i) FTO/c-TiO_2/$Cs_xFA_{1-x}PbI_3$/spiro-MeOTAD/Au (or Ag)[100,101,119] and (ii) FTO/c-SnO_2/C60-SAM/$Cs_{0.2}FA_{0.8}PbI_3$/spiro-MeOTAD/Au.[118] Encapsulated $Cs_xMA_{1-x}PbI_3$ devices were reported to show some promises regarding long-term stability tests under continuous white light illumination (250 h)[100] or unencapsulated devices under storage at low relative humidity (~15%) for 350 h.[101] Lee et al.[100] proposed that partial substitution of FA^+ by Cs^+ leads to the contraction of the cuboctahedral volume (Figure 5c,d), and consequently enhances the interactions between FA^+ and iodine. Calculated lattice parameters of $Cs_xMA_{1-x}PbI_3$ vary from ~6.363 Å (x = 0) down to ~6.310 Å (x = 0.25).[101] Full width at half-maximum (fwhm) was reported to broaden with increasing Cs content (Figure 5d), which was correlated with a decrease in grain size (Figure 5e).[100,118] An exception is observed in the work by Li et al.[101] who observed enhancement in grain size as a function of Cs addition. Nevertheless, proposed additional strategies such as the use of $Pb(SCN)_2$ additive[118] and microstructure-mediated $\delta \rightarrow \alpha$ phase transformation methods[119] in perovskite film formation help further enlarge grain sizes. The lattice contraction of $Cs_xMA_{1-x}PbI_3$ with increasing Cs concentration (Figure 5d) leads to increase in E_g (Figure 5f) from ~1.50 eV (x = 0) up to ~1.59 eV (x = 0.3) resulting in lower J_{sc} (and consequently diminishing PCEs).[100,101,118,119]

Similar to the α,δ-$FAPbI_3$ perovskite (Figure 3b), $CsPbI_3$ also shows the polymorphism; however, the $\alpha \rightarrow \delta$ phase transition temperature is much higher (>300 °C) than in the $FAPbI_3$ case (Figure 6a). Although the black α-$CsPbI_3$ has E_g of ~1.67 to ~1.73 eV (Figure 6f),[82,155] solar cells based on $CsPbI_3$ have exhibited low PCEs (<2.9%),[115,155,156] which was attributed to the structural instability, i.e., favorable $\alpha \rightarrow \delta$ phase transformation at room temperature (Figure 6b,d,e).[155,157] Typical E_g for the yellow δ-$CsPbI_3$ is ~2.82 eV (Figure 6f).[155] Despite these complex behaviors of $FAPbI_3$, $CsPbI_3$ and predominance of δ-phases at room temperature, it is interesting to note that mixing small quantities of Cs with FA substantially enhances the stability of $Cs_xFA_{1-x}PbI_3$.[100,101,118,119] For example, the $\delta \rightarrow \alpha$ phase transformation in $FAPbI_3$ that occurs at ~125−165 °C (Figure 6a)[65,82,101,111,121] can be lowered down to room temperature when Cs/FA ratio of 45 at. % is incorporated in the $Cs_xFA_{1-x}PbI_3$.[101] This decrease of phase transition temperature suggests that the stability of black phase α-$FAPbI_3$ can be stabilized even at room temperature, which is important for solar cell applications.[101] An explanation for the enhanced stability of $Cs_xMA_{1-x}PbI_3$ perovskites was proposed by Li et al.[101] based on the empirical Goldschmidt tolerance factor (t).[158−160] For a composition of $A_xB_{1-x}PbI_3$, the effective tolerance factor ($t_{effective}$) is given by (eq 1). The atomic-ratio weighted average of two different cations is used as the estimated effective cation size ($r_{effective}$) as shown in (eq 2).

$$t_{effective} = \frac{r_{effective} + r_{I^-}}{\sqrt{2}\,(r_{Pb^{2+}} + r_{I^-})} \quad (1)$$

$$r_{effective} = x r_{A^+} + (1 - x) r_{B^+} \quad (2)$$

(Cs/FA)PbI_3 perovskite materials tend to form δ-phase orthorhombic perovskite structure (e.g., δ_O-$CsPbI_3$) for t < 0.8, a cubic structure for 0.8 < t < 1 (e.g., $Cs_xFA_{1-x}PbI_3$), and a hexagonal nonperovskite structure for t > 1 (e.g., δ_H-$FAPbI_3$) (Figure 7a).[101] Alloying $FAPbI_3$ with a high t value and $CsPbI_3$ with a low t value, $t_{effective}$ can be tuned to be between 0.8 and 1.0 in $Cs_xMA_{1-x}PbI_3$ perovskites, which favors a stable perovskite structure. This concept was extended to other alloy systems to verify its validity (Figure 7b).[101] For the different alloy compositions reported (see Figure 7b), [a] $MA_{0.6}FA_{0.4}PbI_3$,[102] [b] $(FAPbI_3)_{1-x}(MAPbBr_3)_x$ (x = 0.15),[63] [c] $MA_{0.13}FA_{0.87}PbI_3$,[106] [d] $Cs_{0.15}FA_{0.85}PbI_3$,[101] [e] $MA_{0.9}Cs_{0.1}PbI_3$,[115] the best performing devices are for perovskites with $t_{effective}$ around 0.94−0.98 (red circle).[101] On the other hand, poor-photoactive mixed perovskites assemble at the low tolerance factor region with t < 0.85 (green area).[101] In summary, Li et al.[101] proposed that $t_{effective}$ (eqs 1 and 2) can be a simpler figure of merit to roughly predict stable structures of mixed perovskite alloys. Furthermore, they extracted that $t_{effective}$ of approximately 0.95 but not exceeding 1 is good for maintaining a cubic perovskite structure. However, an $t_{effective}$ lower than 0.85 would cause too much distortion in the lattice leading easily to nonperovskite structures.[101] Returning to the (MA/FA)PbI_3 system, Dai et al.[152] found that all mixed $FA_xMA_{1-x}PbI_3$ nanorods presented longer photoluminescence (PL) lifetimes than the pure $FAPbI_3$ and $MAPbI_3$ nanorods, (blue squares, Figure 7c). The longer PL lifetimes at the composition around $FA_{0.4}MA_{0.6}PbI_3$ (Figure 7c) was correlated with a lower density of defects and consequently resulting in high performance.[102,104,105,107−113] Based on PL measurements, Dai et al.[152] identified that the FA/MA molar ratio region in the range of 37.5−91% would lead to high performing solar cells (gray area, Figure 7c).

2.4. Binary (FA/Rb)PbI_3 System. Recently, Rb^+ cation, which has an even smaller ionic radius of 0.152 nm than Cs^+ (Figure 6), has also received attention due to the viability of enhancing further both the efficiency and stability of Rb-mixed perovskite solar cells.[121,122,137] Due to the intrinsic nonperovskite structure of δ-$RbPbI_3$ (Figure 6c and 8a,b), it has been rarely investigated as a light harvesting material for perovskite solar cell.[121,122,137,157] In fact, $RbPbI_3$ is known to have only the δ-phase (E_g ~ 2.7−3.1 eV)[121,161−163] and the α-phase has not been reported.[121,122,137,157,164] As shown by heating experiments of $RbPbI_3$ films at different temperatures (Figure 8b), $RbPbI_3$ at 28 °C is yellow; upon heating to 380 °C still the yellow color persists in $RbPbI_3$ while $CsPbI_3$ (as comparison) has transformed to its black α-$CsPbI_3$. Further heating up to 460 °C causes eventually both $RbPbI_3$ and $CsPbI_3$ to melt, and $RbPbI_3$ does not show a black phase (Figure 8b).[121,137]

The (FA/Rb)PbI_3 system was studied systematically and independently by Park et al.[121] and Zhang et al.[122] Both studies report that only a small Rb quantity ($x \leq 0.05$) can be incorporated into the $Rb_xFA_{1-x}PbI_3$ perovskite lattice, otherwise phase segregation will occur. As shown in Figure 8c, the formation of the black α-phase $Rb_{0.05}FA_{0.95}PbI_3$ started at 120 °C, whereas for $FAPbI_3$ started at a higher temperature of 140 °C and completely darkened at 150 °C. XRD patterns of $Rb_{0.05}FA_{0.95}PbI_3$ (Figure 8d) and $FAPbI_3$ (Figure 8e) confirms a slightly lower transition temperature for the $Rb_{0.05}FA_{0.95}PbI_3$ compared to $FAPbI_3$.[121,122] Further differential scanning calorimetry (DSC) results also confirmed a temperature difference of ~10 °C when probing the $\delta \rightarrow \alpha$ phase transitions of $Rb_{0.05}FA_{0.95}PbI_3$ and $FAPbI_3$.[121] Park et al.[121] described that the area under the transition peak in DSC curve is indicative of enthalpy of transition (ΔH). The area of the peak

DOI: 10.1021/acsami.7b06001
ACS Appl. Mater. Interfaces XXXX, XXX, XXX−XXX

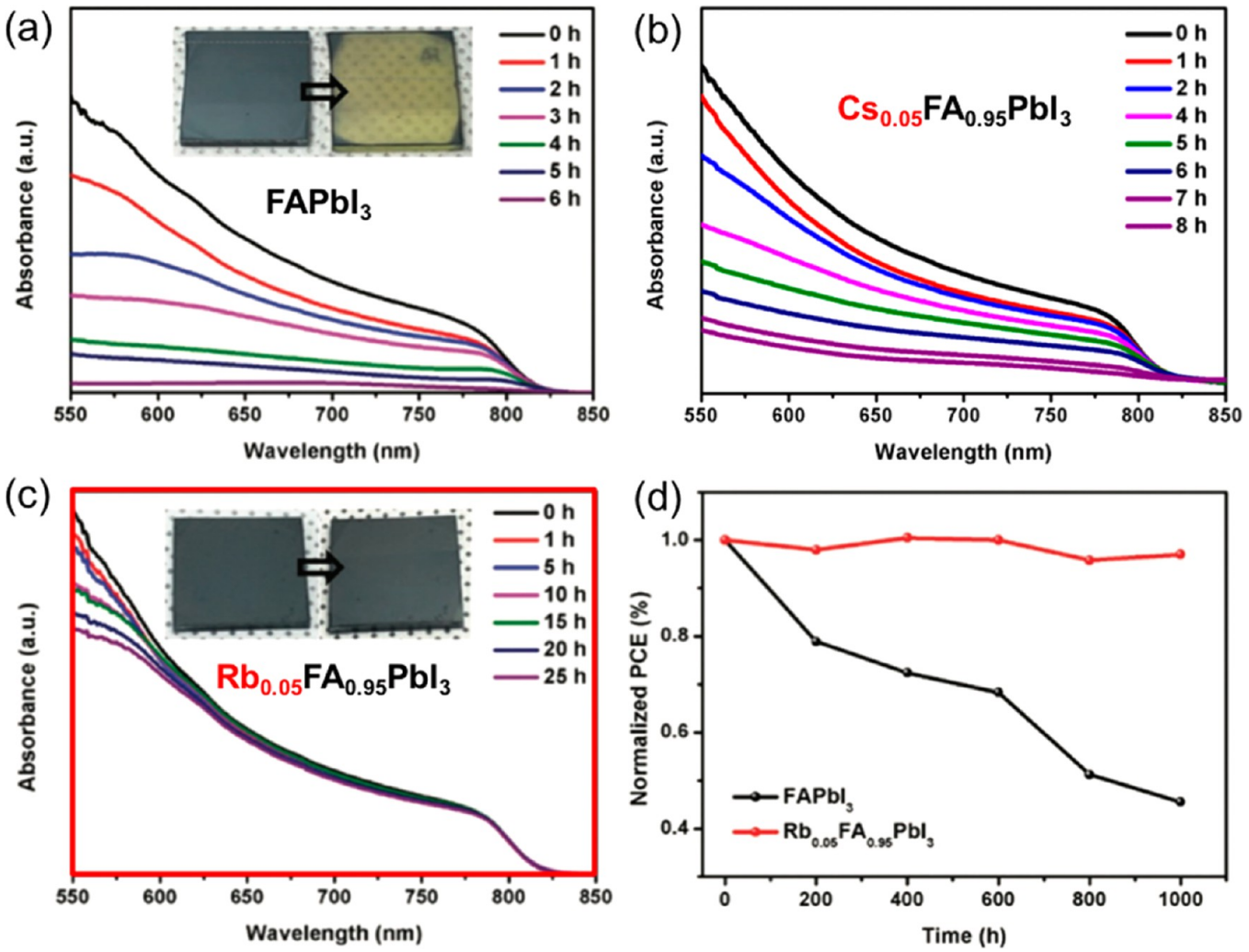

Figure 9. Stability tests (85% RH, 25 °C, and dark) of (a) $FAPbI_3$, (b) $Cs_{0.05}FA_{0.95}PbI_3$, and (c) $Rb_{0.05}FA_{0.95}PbI_3$ perovskite films monitored by the changes in absorbance as a function of time. The enhanced stability of $Rb_{0.05}FA_{0.95}PbI_3$ films is highlighted from this comparison experiments. (d) Comparison of the stability of $FAPbI_3$ and $Rb_{0.05}FA_{0.95}PbI_3$-based unencapsulated devices kept under ambient conditions (average 55% RH) and in the dark. Reprinted with permission from ref 121. Copyright 2017 WILEY-VCH Verlag GmbH & Co. KGaA, Weinheim.

corresponding to the perovskite $\delta \rightarrow \alpha$ phase transition was observed to be smaller for $Rb_{0.05}FA_{0.95}PbI_3$ than $FAPbI_3$, indicating that perovskite transition to α-phase is more favorable when Rb is present in $FAPbI_3$. It was also reported that the $\delta \rightarrow \alpha$ phase transformation kinetics of $Rb_{0.05}FA_{0.95}PbI_3$ is faster (~60 s) than $FAPbI_3$ (~4 min).[121]

Park et al.[121] and Zhang et al.[122] showed that perovskite devices based on $Rb_{0.05}FA_{0.95}PbI_3$ when compared to $FAPbI_3$ devices, outperformed in PCE from 11.1% → 16.15% (on average) and 14.9% → 16.2%, respectively. More importantly, the superior enhanced stability against moisture of Rb-mixed perovskites (Figure 9) was highlighted in these two works.[121,122] Figure 9a,b,c shows the absorbance change with time for $FAPbI_3$, $Cs_{0.05}FAPbI_3$, and $Rb_{0.05}FA_{0.95}PbI_3$ films kept in a sealed box at 85% RH and 25 °C.[121] In the case of $FAPbI_3$, the film degraded after 6 h indicated by the formation of δ-phase and/or PbI_2 (Figure 9a). Slightly better stability can be inferred when Cs is incorporated forming $Cs_{0.05}FAPbI_3$ (Figure 9b). However, no obvious changes in the absorbance onset (~800 nm) can be observed for $Rb_{0.05}FA_{0.95}PbI_3$ films even after 25 h air exposure (Figure 9c). Cs^+ and Rb^+ cations have chemically and electrostatically similar properties if not equal because they belong to the same alkali metal group. The stability properties in $Cs_{0.05}FAPbI_3$, and $Rb_{0.05}FA_{0.95}PbI_3$ perovskites are mainly dictated by the small differences in the ionic radius for hexacoordinated Cs^+ (0.167 nm) and Rb^+ (0.152 nm). This ionic radius difference is not significant, and it is remarkable the enhanced stability of $Rb_{0.05}FA_{0.95}PbI_3$ compared to that of $Cs_{0.05}FA_{0.95}PbI_3$ (Figure 9b,c). Park et al.[121] and Zhang et al.[122] also compared the long-term stabilities (~1 month) of complete devices (FTO/c-TiO_2/mp-TiO_2/$Rb_{0.05}FA_{0.95}PbI_3$/Spiro-MeOTAD/Au) evaluating under ambient air storage conditions without any encapsulation. $Rb_{0.05}FA_{0.95}PbI_3$-based solar cells maintained a PCE >97%[121] and >90%[122] of their initial efficiencies corresponding to the fresh devices.

Yi et al.[117] proposed that the stability of $Cs_xFA_{1-x}PbI_3$ perovskites could be rationalized based on the structural and thermodynamics arguments of internal energy variation (ΔE) and entropic gains (ΔS, mixing entropy concept) (Figure 10a). They calculated the free energies, $\Delta F = \Delta E - T \cdot \Delta S$ (black squares, Figure 10a), of $Cs_xFA_{1-x}PbI_3$ with δ-, β-, α-phases considering different Cs contents ($0 \leq x \leq 1$). A range in Cs composition was identified to lead to $\Delta F < 0$ (black squares,

DOI: 10.1021/acsami.7b06001
ACS Appl. Mater. Interfaces XXXX, XXX, XXX−XXX

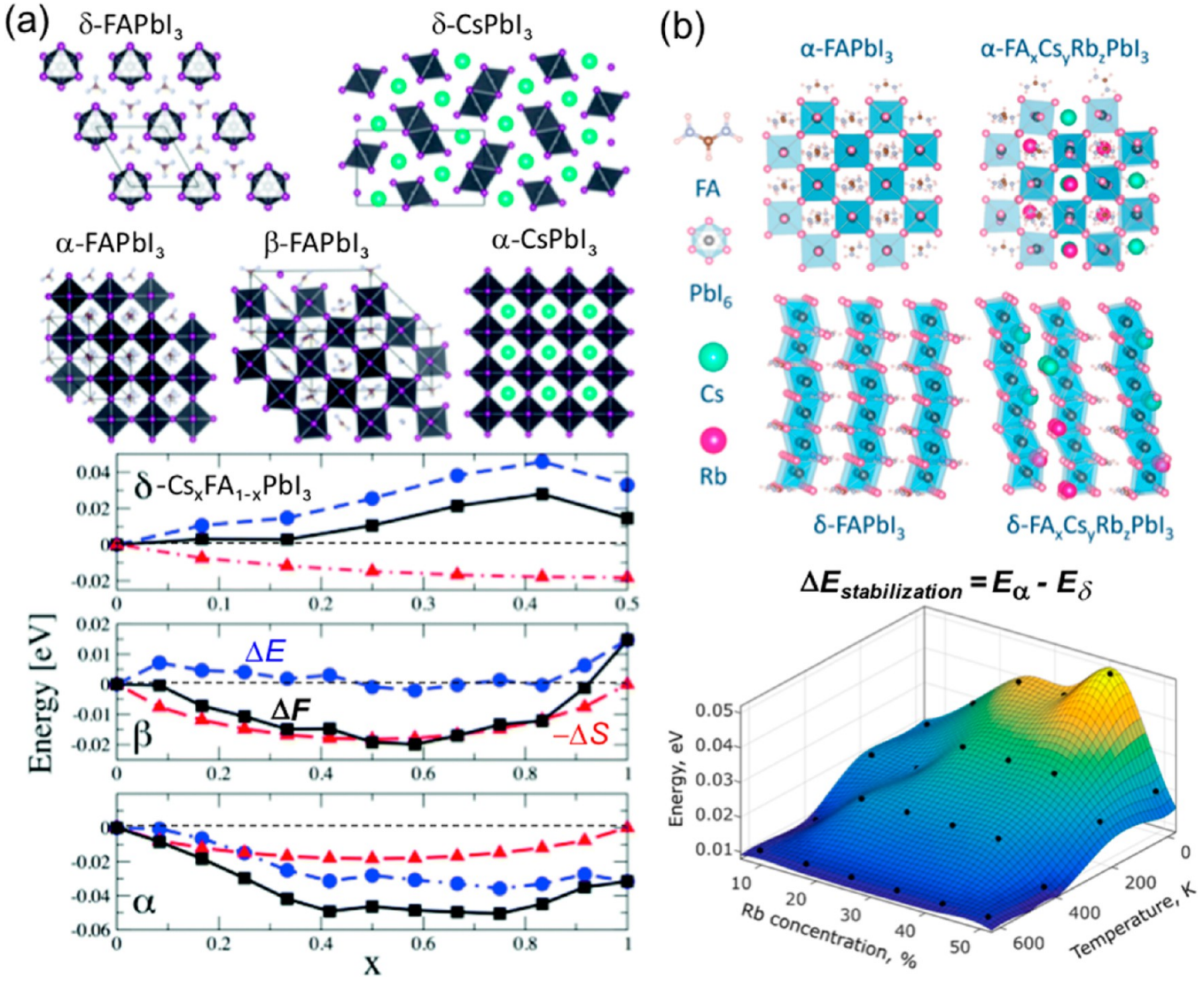

Figure 10. (a) Crystal structure of various polymorphs of $FAPbI_3$ and $CsPbI_3$. The stability of $Cs_xFA_{1-x}PbI_3$ was rationalized based on structural and thermodynamic arguments. Variation of internal energy ΔE (blue circles), mixing entropy contribution $-\Delta S$ (red triangles), and free energy $\Delta F = \Delta E - T\cdot\Delta S$ (black squares). $\Delta F < 0$ (below the dashed lines) signifies stability is observed. Reprinted with permission from ref 117. Copyright 2016 The Royal Society of Chemistry. (b) Structures of pure $FAPbI_3$ and mixed $FA_xCs_yRb_zPbI_3$ in α- and δ-phases. Reprinted with permission from ref 157. Copyright 2017 American Chemical Society.

Figure 10a), which signifies stable configuration. The stabilization energy was calculated to be in the order of 0.05 eV ($\sim 2k_BT$ at room temperature) and 0.02 eV ($\sim 0.8k_BT$) per stoichiometric unit for α- and β-phases, respectively. Based on this model, the $\delta \rightarrow \alpha$ or β transition temperature is reduced by ~200−300 K when going from pure $FAPbI_3$ to the mixed $Cs_xFA_{1-x}PbI_3$ perovskites. In a follow-up work, Syzgantseva et al.[157] have recently performed additional computational study comparing the influences of MA^+, Cs^+, Rb^+ cation substitutions on the stabilization energies of $FAPbI_3$ perovskite (Figure 10b) based on the same arguments described by Yi et al.[117] The relative stabilization energies ($\Delta E_{stabilization} = E_\alpha - E_\delta$, Figure 10b) of α- (E_α) with respect to δ-phase (E_δ) were determined using simulations of a series of α and δ structures, in which FA^+ cations were successively substituted by MA^+, Cs^+, and Rb^+. Cs^+ and Rb^+ were shown to be more efficient in stabilizing the perovskite than MA^+ based on the balance of ΔE and ΔS.[117,157] The introduction of Cs^+ and/or Rb^+ thermodynamically favors the formation of new perovskite phases, bringing the system into a new equilibrium state.[157]

To achieve a systematic understanding of the influences of mixing halides in the ABX_3 structure, in the next section we will first describe simpler systems constraining the A cation to single elements (MA^+, FA^+, or Cs^+) and allowing to vary halide part (I/Br, I/Cl, or I/Br/Cl) in the X site.

3. MIXED X HALIDE ANIONS

A handful number of reviews described and summarized the new optoelectronic properties of mixed perovskites when mixed halide ions are incorporated in perovskites.[5,7,8,14,15,24,26] Below we present the current views of the structure−property relationship based on a survey of recently published papers summarized for MAPb(I/Cl), FAPb(I/Cl), MAPb(I/Br), FAPb(I/Br), MAPb(Br/Cl), CsPb(I/Br), CsPb(Br/Cl), CsPb(I/Cl), MAPb(I/Br/Cl).

3.1. Binary MAPb(I/Cl) and FAPb(I/Cl) Systems. The MAPb(I/Cl) material system is by far one of the most studied

DOI: 10.1021/acsami.7b06001
ACS Appl. Mater. Interfaces XXXX, XXX, XXX−XXX

Table 2. Summary of Experimental Conditions for $MAPbI_{3-x}Cl_x$ Synthesis Methods and Experimental Technique and Measurement Conditions Extracted from References 60, 165−199, 209[a]

ref. (Year)	Sample structure	$MAPbI_{3-x}Cl_x$ fabrication method	$MAPbI_{3-x}Cl_x$ fabrication environmental conditions	Experimental techniques	Measurement environmental conditions	Cl detected?	Main conclusions
165 (2017)	ITO/PEDOT:PSS PVSK	(1) 40 wt % dissolving MAI and $PbCl_2$ in 3:1 molar ratio in DMF.	N_2 glovebox	TOF-SIMS	Vacuum	Yes	(1) $MAPbCl_3$ forms as intermediate phase during crystallization.
				XPS	Vacuum		
				GIXRD	N_2 flux		
		(2) Postannealing at 100 °C in a N_2 glovebox from 10 to 100 min.					(2) After completion of PVSK crystallization some Cl detected by TOF-SIMS.
		(3) ∼250 thickness.					(3) Cl is majorly located at the interface and within the underlying PEDOT:PSS.
166 (2016)	FTO/c-TiO_2/PVSK	Redissolution and crystal grain growth via spray coating:	Ambient	XPS	Vacuum	Yes	Atomic ratio of Cl:I ∼ 3:97 determined by XPS.
		(1) MAI and $PbCl_2$ in 3:1 molar ratio dissolved in IPA.					
		(2) Centrifuge.					
		(3) $MAPbI_{3-x}Cl_x$ redissolved in DMF:GBL.					
167 (2016)	Glass slide	Single-crystalline nanofibers; Stock solutions of (MACl+$PbCl_2$/DMF, 0.03 M) and (MAI+PbI_2/DMF, 0.03 M) at different volume ratios.	–	EDX, XRD, UV−vis, PL	–	Yes	(1) EDX analysis showed compositions of $MAPbCl_{0.27}I_{2.73}$, $MAPbCl_{0.55}I_{2.45}$, $MAPbCl_{0.75}I_{0.25}$.
							(2) 3D crystal structure for $MAPbI_{3-x}Cl_x$ proposed.
168 (2016)	FTO/c-TiO_2/mp-TiO_2/PVSK	Vapor-assisted solution deposition: 1 M PbI_2 in DMF spin coated and substrate heated at 110 °C (15 min); PbI_2 film placed 2 mm above MACl source in an oven; Postannealing at 70 °C (30 min).	–	EDX, XRD	–	Yes	(1) EDX showed Cl:I ∼ 0.61.
							(2) XRD showed $MAPbCl_3$ phase.
							(3) Assuming 4% Cl incorporation in $MAPbI_{3-x}Cl_x$ lattice, the ratio of $MAPbI_{3-x}Cl_x$ and MAPbI3 phases will be ∼65:35. This is close to expected reaction: $3MACl + 3PbI_2 \rightarrow 2MAPbI_3 + MAPbCl_3$.
169 (2015)	FTO/c-TiO_2/PVSK (and) SiN/PVSK	(1) MAI and $PbCl_2$ in 3:1 molar ratio dissolved in DMF.	–	XANES	He atmosphere	Yes	(1) $x = 0.05 \pm 0.03$ Cl atoms per formula unit (i.e., Pb atom).
		(2) Postannealing at 95 °C for 0, 15, 60, 90, 120 min in dry air (3 ppm of H_2O).					(2) Cl may be incorporated in the film directly (e.g., substitution or interstitial) or indirectly (e.g., grain boundary or poor crystalline region).
170 (2015)	ZnS optical prism/PEDOT:PSS/PVSK	Multicycle spin-coating process: PbI_2 in DMF spin-coated on substrate; MAI/MACl (4:1 molar ratio) in IPA spin-coated on PbI_2 film; Postannealing at different temperatures.	—	PTIR	Under N_2 flow	Yes	(1) Mild annealing (60 °C, 1 h) leads to a $MAPbI_{3-x}Cl_x$ film with Cl-rich ($x < 0.3$) and Cl-poor phases.
							(2) Further annealing (110 °C) leads to a homogeneous Cl-poorer ($x < 0.06$) phase.
171 (2015)	Quartz	Vacuum coevaporation of MAI and $PbCl_2$; Postannealing at 70, 80, 90, 100, 110, 120 °C (1 h) in N_2 glovebox; ∼530 nm thickness.	Vacuum	XRD, EDX, UV−vis, PL	–	Yes	(1) As-grown $MAPbI_{3-x}Cl_x$ showed 0.13 at. % Cl.
172 (2015)	c-TiO_2/PVSK	(1) MAI and $PbCl_2$ in 3:1 molar ratio dissolved in DMF.	–	Ion chromatography	Films dissolved in DI water and H_2SO_4 (0.15 M)	Yes	(1) $MAPbI_{2.94}Cl_{0.06}$ composition determined.
		(2) Postannealing at 120 °C for 45 min.					
173 (2015)	ITO/PEDOT:PSS PVSK	Two-step method: (1) 1.5 M $PbCl_2$/PbI_2 dissolved in DMF and spin coated.	Ambient air with 20 °C and 20% RH.	Potentiometric titration method, XRD, UV−vis	Ultrapure water	Yes	(1) Measured $n_{Cl}/(n_{Cl} + n_I)$ mole fraction content in PVSK according to ($PbCl_2$/PbI_2): 0.012 ± 0.008 (0.10); 0.073 ± 0.012 (0.20); 0.185 ± 0.015 (0.30); 0.220 ± 0.015 (0.40).
		(2) substrate dipped in MAI dissolved in IPA at 70 °C.					(2) Band gap varies from 1.54 to 1.59 eV with increasing Cl.
							(3) XRD shows shifts in (110) and (220) peaks.

ACS Appl. Mater. Interfaces XXXX, XXX, XXX−XXX
DOI: 10.1021/acsami.7b06001

Table 2. continued

ref. (Year)	Sample structure	$MAPbI_{3-x}Cl_x$ fabrication method	$MAPbI_{3-x}Cl_x$ fabrication environmental conditions	Experimental techniques	Measurement environmental conditions	Cl detected?	Main conclusions
		One-step method.				Yes	$n_{Cl}/(n_{Cl} + n_I)$ mole fraction of 0.056 ± 0.015 determined.
174 (2015)	FTO/c-TiO_2/PVSK	(1) MAI and $PbCl_2$ in 3:1 molar ratio dissolved in DMF. (2) Postannealing at 90 °C (2.5 h) and then 120 °C (15 min).	N_2 glovebox	HAXPES, FY-PES	Vacuum	Yes	(1) Cl is depleted from top surface. (2) Upper limit on the amount of Cl in $MAPbI_{3-x}Cl_x$: $x < 0.07$ and $x < 0.40$ to depths of ∼10 and ∼26 nm, respectively. (3) High Cl concentration ($x > 0.40$) deep in the film and near PVSK/TiO_2 interface.
175 (2015)	FTO/c-TiO_2/PVSK	Two-step method: (1) PbI_2 in DMF spin coated. MAI/MACl (10:1 in weight) dissolved in IPA spin coated on top of dry PbI_2 film. (2) PbI_2 in DMF spin coated. MACl dissolved in IPA spin coated on top of dry PbI_2 film. Both films annealed in air at 135 °C.	Dry air (Dew Point of −70 °C)	XRD, XPS	–	Yes	(1) Cl incorporation improve carrier transport across heterojunction interfaces, rather than within perovskite crystal. (2) XRD showed ∼0.5% difference of the unit cell volume. (3) Very weak Cl 2p signal in XPS; Cl has negligible impact on the original crystal structure.
176 (2014)	Glass/PVSK (for optical and structural determination) (and) Si/TiO_2 (for GIWAXS)	(1) MAI and $PbCl_2$ in 3:1 molar ratio dissolved in DMF. (2) Postannealing at 95 and 100 °C for various times.	PVSK preparation in glovebox. Post annealing in air and N_2 for comparison.	GIWAXS, in situ XRD, XPS, XRF, EDX, UV−vis	In situ XRD in ambient; XPS and EDX in vacuum; UV−vis in glovebox	Yes	(1) $MAPbI_{3-x}Cl_x$ with maximum of $x = 0.15$ determined based on lattice volume. (2) Cl content of samples annealed at 95 °C for 120 min, varies from 0 to 0.3 Cl per formula unit determined by XRF. (3) XPS and EDX did not show Cl. (4) Small Cl amount incorporated in the crystal lattice; Most of Cl resides at grain boundary or interface with substrate.
177 (2015)	FTO/c-TiO_2/PVSK	Two-step method: (1) 1 M PbI_2 in DMF. (2) Substrate dipping into MACl + MAI dissolved in IPA.	–	KPFM	–	Yes	Larger band-bending at grain boundaries with Cl incorporation.
178 (2015)	ITO/PEDOT:PSS/PVSK	Layer-by-layer growth: $PbCl_2$ thermally evaporated in vacuum; Dipping in MAI solution (IPA); Similarly a second $PbCl_2$ thermally evaporated on $MAPbI_{3-x}Cl_x$ and dipped into MAI solution. These cycles are repeated until desired film thickness is attained.	–	XPS	Vacuum	Yes	(1) Cl atomic ratio was 8.3%. The ratio above is much higher than that of solution-cast counterpart (1.4%).
179 (2014)	FTO/c-TiO_2/PVSK	(1) 1.5 wt % dissolving MAI and $PbCl_2$ in 3:1 molar ratio in DMF. (2) Postannealing at 100 °C for 1 h. (3) ∼15 nm thickness.	N_2 atmosphere	AR-XPS	Vacuum	Yes	Chloride located at TiO_2/PVSK
180 (2014)	Soda lime glass/PVSK	Vacuum coevaporation of MAI and $PbCl_2$.	Vacuum	In situ XRD, EDX	Vacuum	Yes	(1) There exists a miscibility gap for $MAPbI_3$ and $MAPbCl_3$ in the $0.5 < x < 0.95$ regime for $MAPb(I_xCl_{1-x})_3$. (2) Cl incorporation stabilizes the cubic phase of $MAPbI_3$ at room temperature.
181 (2015)	FTO/c-TiO_2/PVSK	(1) 0.88 M $PbCl_2$ + 2.64 M MAI. (2) 0.88 M PbI_2 + 0.88 M MAI + 0.88 M MACl. (3) Films were dried at 70 °C (10 min) and annealed at 100 °C (45 min).	Glove box	TGA, XPS, EDX	TGA in N_2 flow (40 mL/min) and ∼10 mg of PVSK; XPS and EDX in vacuum	Yes	(1) Cl content in the film is miniscule, but detected by XPS (∼1 at. %) and TGA (∼1.3 at. %). (2) EDX did not detect Cl. (3) $MAPbI_{3-x}Cl_x$ shows tetragonal *I*4/*mcm* structure.

ACS Appl. Mater. Interfaces XXXX, XXX, XXX−XXX
DOI: 10.1021/acsami.7b06001

Table 2. continued

ref. (Year)	Sample structure	$MAPbI_{3-x}Cl_x$ fabrication method	$MAPbI_{3-x}Cl_x$ fabrication environmental conditions	Experimental techniques	Measurement environmental conditions	Cl detected?	Main conclusions
182 (2014)	FTO/PVSK	MAI and $PbCl_2$ in 3:1 molar ratio dissolved in DMF; Postannealing at 100 °C (50 min).	N_2 glovebox	XPS depth profile (Ar sputtering), EDX	Vacuum	Yes	(1) Very weak Cl signal in XPS of ∼1% Cl detected for the top 20 nm. (2) EDX probed Cl content of 0.7 at. %. There is a note that detection limit of EDX setup is ∼1 at. %.
183 (2014)	ITO/PEDOT:PSS/PVSK	MAI and $PbCl_2$ in 3:1 molar ratio dissolved in DMF; Postannealing at 90 °C (2 h).	–	XPS	Vacuum	Yes	(1) Cl/(Cl + I) ∼ 2.2% detected by XPS. (2) XRD shows similar diffraction pattern to $MAPbI_3$; therefore, only small fraction of Cl can be incorporated.
184 (2014)	ITO/TiO_2/PVSK	22.5−60 wt % MAI and $PbCl_2$ in 3:1 molar ratio dissolved in DMSO; Postannealing at 100 °C (50 min).	N_2 glovebox (<1 ppm of O_2 and H_2O)	XPS	Vacuum	Yes	XPS on the 60 wt % precursor concentration, showed atomic composition of C:N:Pb:I:Cl = 1.04:1:1.05:2.02:0.99.
185 (2013)	Glass slide (and) FTO/c-TiO_2/mp-TiO_2/PVSK	(1) 20 wt % MAI and $PbCl_2$ (3:1 molar ratio) dissolved in DMF; Postannealing at 100 °C (45 min). (2) 20 wt % MACl and PbI_2 (1:1 molar ratio) dissolved in DMF; Postannealing at 100 °C (10 min).	Spin coating in N_2 flux.	EDX	Vacuum	Yes	(1) Reliable values of the Cl content not achieved as the amplitude of Cl-related signal was observed to decrease during the measurement. (2) Based on DFT, Cl incorporation is allowed at low concentrations (below 3−4%) in $MAPbI_3$.
60 (2012)	FTO/c-TiO_2/mp-TiO_2(or Al_2O_3)/PVSK	MAI and $PbCl_2$ in 3:1 molar ratio dissolved in DMF; Postannealing at 100 °C for 45 min.	Ambient air	EDX	Vacuum	Yes	$MAPbI_2Cl$ had I/Cl ratio ∼2:1.
186 (2017)	FTO/c-TiO_2/PC61BM/PVSK	1 M $PbCl_2$:PbI_2 (molar ratios of 0:1, 1:3, 11: 3:1)	N_2 glovebox (RH < 10%)	XRD, XPS	–	No	(1) Cl can be incorporated into precursor film in the form of PbICl or $PbCl_2$ and it was found in the final PVSK film in $MAPbCl_3$, PbICl, or $PbCl_2$. (2) No evidence for $MAPbI_{3-x}Cl_x$ phase observed. (3) $MAPbI_{3-x}Cl_x$ phase is relatively unstable or possess higher formation energy.
187 (2017)	FTO/c-TiO_2/PVSK	MAI and $PbCl_2$ in 3:1 molar ratio dissolved in DMF; Postannealing at 100 °C (110 min).	Glove box	XRD, UV−vis, XPS	–	No	XPS shows negligible amount of Cl in fully annealed films.
188 (2016)	Glass	PbI_2 and $PbCl_2$ dissolved in DMSO spin coated on glass and loaded in XRD stage. MAI powder dispersed around the film and sample stage controllably heated.	He atmosphere	in situ XRD, TOF-SIMS	In situ XRD in He	No	(1) In the presence of reactive I^- ions, neither Br^- nor Cl^- can be incorporated into the perovskite crystal lattice. (2) TOF-SIMS mapping revealed that Cl^- resides in the grain boundaries, possibly in the form of amorphous Cl^--based compounds.
189 (2016)	FTO/c-TiO_2/PVSK	MAI and $PbCl_2$ in 3:1 molar ratio dissolved in DMF; Postannealing at 90 °C (2 h), 100 °C (10 min), 130 °C (5 min).	–	in situ XRD	N_2 atmosphere	No	(1) Initially, the film crystallizes in $MAPbCl_3$ and is fully converted to $MAPbI_3$ after a certain time under heating.
209 (2016)	MAPbI(Cl) single crystal	Supporting info in ref209.	–	XRD, XPS, TOF-SIMS	–	No	(1) Below detection limits of XPS. (2) Trace amounts of Cl detected by TOF-SIMS.
190 (2015)	ITO	(1) Sequential vacuum evaporation of MAI (15 nm) and then $PbCl_2$. (2) coevaporation.	Vacuum	In situ XPS	Vacuum	No	(1) No Cl detected at the initial $PbCl_2$ deposition (0.2−0.5 nm); Below detection limit of XPS (∼0.1 at. %) (2) As grown and annealed (100 °C, 1 h) MAI:PbI_2 (3:1) films 15 nm did not show Cl in XPS.
191 (2015)	FTO/c-TiO_2/PVSK	(1) PbI_2 dissolved in DMF and spin coated. (2) CVD: First reacted with MACl (120 °C, 5 min) and then with MAI at 145 °C, 100 min.	–	XRD, XPS, EDX	XPS and EDX in vacuum.	No	Cl content not detectable in XPS and EDX.

ACS Appl. Mater. Interfaces XXXX, XXX, XXX−XXX
DOI: 10.1021/acsami.7b06001

Table 2. continued

ref. (Year)	Sample structure	$MAPbI_{3-x}Cl_x$ fabrication method	$MAPbI_{3-x}Cl_x$ fabrication environmental conditions	Experimental techniques	Measurement environmental conditions	Cl detected?	Main conclusions
192 (2015)	ITO/PEDOT:PSS/PVSK	MAI and $PbCl_2$ in 3:1 molar ratio dissolved in DMF; Postannealing at 60 °C (2 h).	Postannealing in vacuum and glovebox	XPS	Vacuum	No	Cl content of 1.36% at. % assigned as MACl residue.
193 (2014)	FTO/c-TiO_2/PVSK	(1) Two-step: PbI_2; MAI:MACl (95:5 wt %) in IPA.	–	STEM-EDS	Vacuum	No	No Cl feature detected within the detection limit of EDS (~1000 ppm).
		(2) Two-step: $PbCl_2$; MAI in IPA.					
		(3) One-step: $PbCl_2$:MAI = 1:3					
194 (2014)	ITO/PEDOT:PSS/PVSK	Several (Table S2 in ref 194) dissolved in DMF; Postannealing at 90 °C for 2–3 h.	N_2 glovebox	TEM, SAED, EDX, XPS	Vacuum	No (below detection limit)	(1) EDX showed I:Pb ~3 at. % ratio.
							(2) Cl was below detection limit of EDX (~0.1 at. %).
							(3) Presence of Cl impacts on the microstructure and orientation of PVSK films.
							(4) SAED patterns indexed to tetragonal $MAPbI_3$.
195 (2014)	FTO/c-TiO_2/PVSK	MAI and $PbCl_2$ in 3:1 molar ratio dissolved in DMF; Postannealing at 120 °C (30–60 min).	Ambient atmosphere	EDX, XPS	Vacuum	No	(1) No signs of Cl in XPS.
							(2) EDX showed no Cl (or is below detection limit, <1% mol).
196 (2014)	Glass/mp-TiO_2/PVSK	MAI and $PbCl_2$ in 3:1 molar ratio dissolved in DMF and DMSO mixed in 7:3 by volume; Postannealing at 140 °C (30 min) in dry air box (RH < 10%); Samples dried in vacuum (5×10^{-5} Torr, 1 h)	Dry air box (RH < 10%)	XRD	Room temperature in air; RH 30–50%; 4 h measurement.	No	Material reported $MAPbI_{3-x}Cl_x$ is a combination of $MAPbI_3$ and $MAPbCl_3$ phases.
197 (2014)	FTO/c-TiO_2/mp-TiO_2/PVSK	PbI_2, MAI, MACl dissolved in DMF with molar ratio of 1:1:x (x varies from 0 to 2; max dissoluble x is ~2.8); Postannealing at 100 °C (5–45 min).	Ambient air	EDX	Vacuum	No	Longer annealing (45 min) leads to complete loss of Cl (within EDX detection limit of 1%).
198 (2014)	FTO/c-TiO_2/PVSK	Two-step: PbI_2 in DMF; Spin coating (~200 nm film thickness); MAI and MACl dissolved in IPA. Substrate immersed.	–	EELS, EDX, XPS	Vacuum	No	Cl was below detection limit of EELS, EDX, XPS.
199 (2014)	FTO/mp-TiO_2/PVSK	MAI and $PbCl_2$ in 3:1 molar ratio dissolved in DMF; Postannealing at different temperatures (60–200 °C) and times (20 to 0.17 h)	Ambient air	XRD	Ambient	No	Cl sublimes as MACl leaving only $MAPbI_3$ as observed in XRD.

[a]Abbreviations: See Table 1. PVSK = "$MAPbI_{3-x}Cl_x$"; DMF = *N*,*N*- dimethylformamide; GBL = γ-butyrolactone; IPA = 2-propanol; XPS = X-ray photoelectron spectroscopy; AR-XPS = angle-resolved XPS; hard XPS (HAXPES); fluorescence yield X-ray absorption spectroscopy (FY-XAS); TOF-SIMS = time-of-flight secondary ion mass spectrometry; GIXRD = glazing-incidence X-ray diffraction; XANES = X-ray absorption near edge structure; EDS/EDX = energy-dispersive X-ray spectroscopy; XRF = X-ray fluorescence spectroscopy; GIWAXS = grazing-incidence wide-angle X-ray scattering, TEM = transmission electron microscopy, SAED = select area electron diffractogram, KPFM = Kelvin probe force microscopy, PTIR = photothermal-induced resonance; TGA = thermogravimetric analysis, PL = photoluminescence, STEM-EDS = scanning transmission electron microscopy EDS. EELS = electron energy loss spectroscopy.

ACS Appl. Mater. Interfaces XXXX, XXX, XXX−XXX
DOI: 10.1021/acsami.7b06001

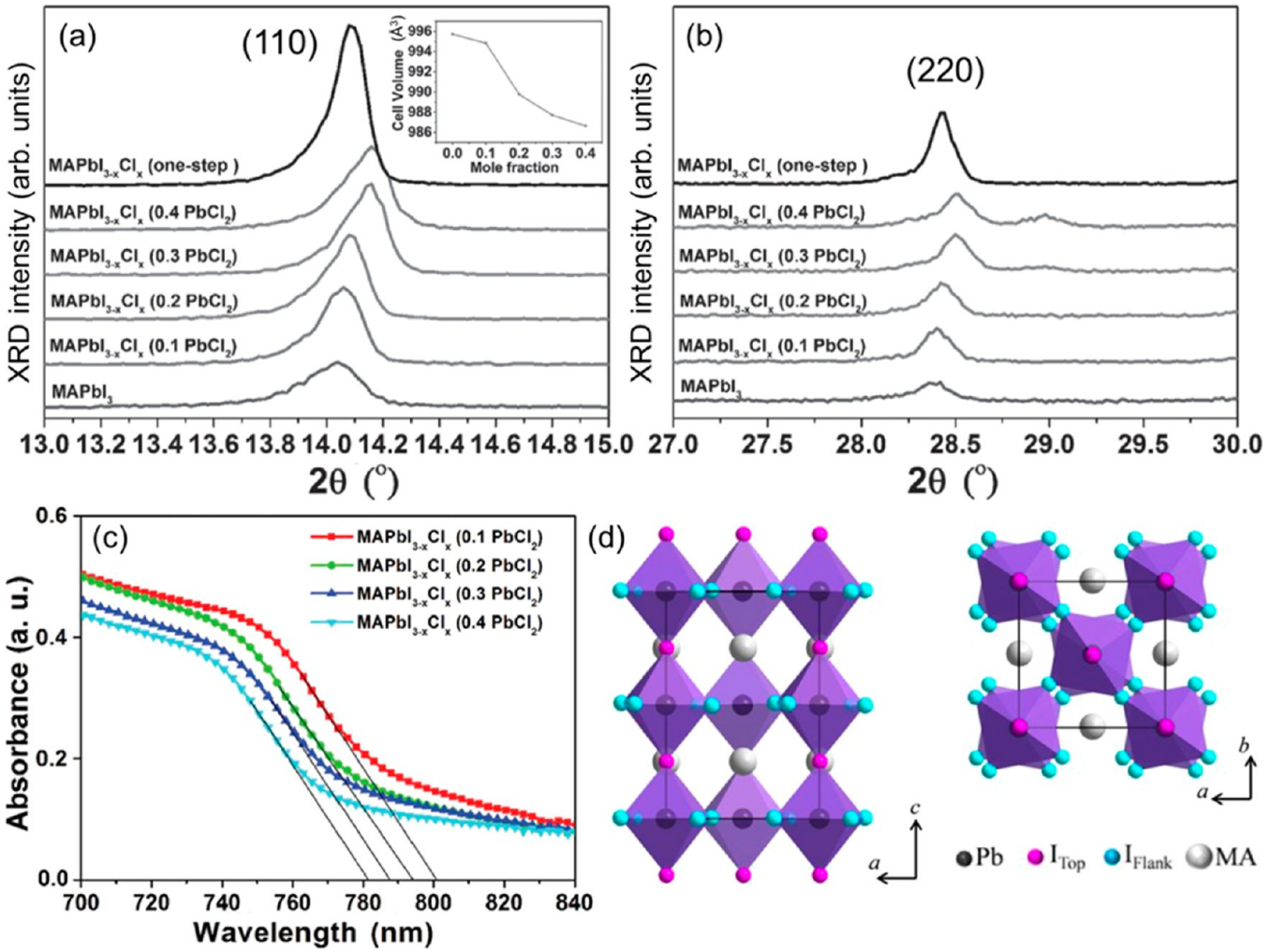

Figure 11. XRD pattern of (a) (110) and (b) (220) lattice planes of $MAPbI_{3-x}Cl_x$ perovskites with different $PbCl_2$ mole fractions by a two-step method. $MAPbI_{3-x}Cl_x$ perovskites formed by one-step method and pure-phase $MAPbI_3$ are shown as comparison. (c) UV−vis of $MAPbI_{3-x}Cl_x$ perovskites with different $PbCl_2$ mole fractions by a two-step method. Reprinted with permission from ref 173. Copyright 2017 WILEY-VCH Verlag GmbH & Co. KGaA, Weinheim. (d) Proposed schematic representation of tetragonal crystal structure of $MAPbI_{3-x}Cl_x$ where Cl atoms partly substituted I at I_{flank} (blue) positions forming different contents of x. Reprinted with permission from ref 167. Copyright 2017 WILEY-VCH Verlag GmbH & Co. KGaA, Weinheim.

binary mixed perovskite.[60,61,165−200] From earlier reports,[2,3,21,47,201,202] PbI_2 and MAI precursors are employed for the synthesis of $MAPbI_3$. Furthermore, if one-step method is employed, generally equimolar ratio of PbI_2:MAI (i.e., 1:1) is used. Lee et al.[60] reported the first deposition approach employing $PbCl_2$ and 3-fold excess of MAI (i.e., 1:3). The dissolution of $PbCl_2$ in *N*,*N*-dimethylformamide (DMF) is difficult when the MAI:$PbCl_2$ molar ratio is lower than 3:1.[194,195] Although Cl incorporation has been reported to improve optoelectronic properties (e.g., diffusion lengths for electron and holes of ∼130 and ∼90−105 nm in $MAPbI_3$ increases by 10 times in $MAPbI_{3-x}Cl_x$, ∼1069 and ∼1213 nm, respectively),[200,203] the controversial question whether Cl can in fact be incorporated into the crystal lattice of $MAPbI_3$ is still not completely settled. Reviews on this topic can be found in refs[8,14,15,169,204] The reported studies show contradicting results regarding detection or absence of Cl in $MAPbI_{3-x}Cl_x$ perovskite (Table 2). From a total of thirty seven studies surveyed by us (Table 2), we find that twenty two confirmed the presence of Cl in $MAPbI_{3-x}Cl_x$ based on an extensive number of analytical tools such as X-ray photoelectron spectroscopy (XPS),[166,175,178,181,183,184] angle-resolved XPS (AR-XPS),[179] XPS depth-profile,[182] hard XPS (HAXPES),[174] fluorescence yield X-ray absorption spectroscopy (FY-XAS),[174] time-of-flight secondary ion mass spectrometry (TOF-SIMS), in situ XRD,[180] glazing-incidence XRD (GIXRD),[165] X-ray absorption near edge structure (XANES),[169] energy-dispersive X-ray spectroscopy (EDX or EDS),[167,168,171,182,185] X-ray fluorescence spectroscopy (XRF),[176] grazing-incidence wide-angle X-ray scattering (GIWAXS), select area electron diffractogram (SAED), photothermal-induced resonance (PTIR),[170] Kelvin probe force microscopy (KPFM),[177] thermogravimetric analysis (TGA),[181] ion chromatography,[172] potentiometric titration.[173] However, there are also at least 15 studies[186−199] arriving at the conclusion that Cl is absent in the final perovskite films or is below the detection limit of the instruments (e.g., EDX detection limit is 0.1−1 at. %[194,195,197] or ∼1000 ppm[193] and XPS detection limit is 0.1 at. %[190]). It has been argued that (1) as a result of the larger difference in ionic radii, Cl incorporation yields low miscibility with iodine;[15,176,185] (2) the $MAPbI_{3-x}Cl_x$ phase is metastable or possess higher formation energies;[186] (3) $PbCl_2$ is the least

DOI: 10.1021/acsami.7b06001
ACS Appl. Mater. Interfaces XXXX, XXX, XXX−XXX

soluble Pb-halide in DMF that may lead to $PbCl_2$ particles;[194,195] (4) experimental evidence that Cl were found at the perovskite/substrate interface (i.e., the affinity of Cl to TiO_2[169,176,179] and PEDOT:PSS[165] is high) and/or grain boundaries;[169,170,176,177] (5) the postannealing step (100 °C, 45 min) leads to sublimation of Cl in the form of MACl;[55,181,182,192,199] (6) $MAPbI_{3-x}Cl_x$ and $MAPbI_3$ perovskites show very similar UV−vis and XRD patterns indicating no or a very small amount of Cl can be incorporated;[15,60,186,191,197−199] (7) crystallization (crystallographic texture, crystalline orientation) and morphological (polycrystalline grain structure) improvements instead of Cl-incorporation.[167,182,194,195,205]

In Table 2, we compare the relevant parameters such as sample conditions (sample preparation method and environment, sample structure, perovskite thicknesses) as well as technical aspects of measurement conditions (vacuum versus ambient pressure and/or under inert gas environment). We find that the different results from these studies may stem from (1) the various sample preparation conditions, for instance, vapor-based techniques (e.g., vacuum codeposition, vapor-assisted solution deposition at ambient, chemical vapor deposition) versus solution methods (one-step and two-step methods; use of MACl or $PbCl_2$ as source for Cl) and (2) the influence of excitation probes and environment during measurements. Zhao and Zhu[197] showed that Cl can be incorporated in $MAPbI_3$ employing MACl precursor by controlling the annealing time (~20 min). On the contrary, Chen et al.[175] reported that it is difficult to incorporate Cl using the MACl precursor. $PbCl_2$ was proposed to be a better way to introduce Cl. Li et al.[173] employed a two-step dipping method for the fabrication of $MAPbI_{3-x}Cl_x$ films, which were deposited on PEDOT:PSS. The $PbCl_2$:PbI_2 with various mole fractions were dissolved at 85 °C in DMF and spin coated on PEDOT:PSS films (after the solutions were cooled to room temperature). The substrates were then dipped into a preheated MAI solution (70 °C, 60 s) dissolved in 2-propanol. Finally, the substrates were postannealed at a temperature of 75 °C for 20 min. It is noticed that in several works large variations in the postannealing temperature is employed for the perovskite crystallization, for example in the one-step method, 90−120 °C for 45−120 min.[60,165,169,172,176,179,181,182,184,185,189,195,199] The fine-tuning of annealing temperature and time will play a major role for the delicate incorporation of Cl into the perovskite crystal lattice. The XRD data on $MAPbI_{3-x}Cl_x$ films using the two-step method by Li et al.[173] show that the (110) and (220) diffraction peaks shift as a $PbCl_2$ concentration increases (Figure 11a,b). Although the shift is small, it is above the instrumental sensitivity and not negligible. They performed further XRD data fitting extracting the lattice parameters and unit cell volumes (inset in Figure 11a). In addition, the XRD pattern shows that the Cl-content in perovskites prepared by the two-step dipping method is higher than the ones fabricated by the one-step method. Furthermore, no (110) diffraction peak (15.68°) related to $MAPbCl_3$ was found indicating no phase segregation occurring (Figure 11a,b).[173,186,196] The UV−vis of perovskite films show the shift of absorption edge toward a shorter wavelength with increasing $PbCl_2$:PbI_2 mole fraction (Figure 11c) corroborating with XRD on solid-solution formation. Zhang et al.[167] synthesized single-crystalline nanofibers (NFs) of $MAPbI_{3-x}Cl_x$ perovskites in the tetragonal phase at room temperature with the Cl-content between $0 \leq x \leq 0.75$. Furthermore, based on SAED patterns it was suggested that I ions are not substituted by Cl ions along the [001] direction of single-crystalline NFs, but the Cl incorporation takes place along the [100] or [010] directions, i.e., within the crystal ab-plane (Figure 11d). In other words, Cl-inclusion occurred along the [001] direction (apical positions) because of high intensity of (110) diffraction planes observed for $MAPbI_{3-x}Cl_x$ perovskites.[15,206−208] Pistor et al.[180] and Luo et al.[171] synthesized $MAPbI_{3-x}Cl_x$ perovskites under vacuum conditions by coevaporation of MAI and $PbCl_2$ sources. Interestingly, upon subsequent postannealing treatments, they observed that a phase transition from tetragonal to a cubic phase (space group $Pm\bar{3}m$ with lattice constant of 6.276 Å) takes place in $MAPbI_{3-x}Cl_x$ perovskites, which was also reported to be stabilized after the cooling at room temperature. As comparison, $MAPbCl_3$ adopts a cubic structure at room temperature (Figure 2d). More recently, a recipe for the synthesis of single crystal MAPb(I/Cl) was reported by Lian et al.[209] and their TOF-SIMS measurements confirmed the trace amount of Cl in the MAPb(I/Cl) bulk film.

The second possible scenario for the discrepancies in the reports could lie on the technical aspects of the measurement conditions. Most of chemical analytical tools (XPS, EDX, TOF-SIMS, etc.) require high vacuum under which volatile species contained in perovskite films can desorb.[174] Furthermore, the situation can be more drastic when perovskite films are exposed to a probing beam (e-beam, UV, X-ray, etc.) that may lead to beam-induced artifacts during measurement. Colella et al.[185] mentioned that reliable values of Cl concentration could not be achieved as the amplitude of the Cl-related signal was observed to decrease during the measurement in EDX. Starr et al.[174] emphasized the importance of employing nondestructive techniques (e.g., HAXPS and FY-XAS) to guarantee that the measurement itself will not modify the original chemical composition of the perovskite samples. Based on the extensive analytical measurements (Table 2), our current understanding is that the incorporation of Cl ions into the perovskite crystal lattice is viable only in a small quantity (<1 at. %), but sufficient to induce new material properties.[173] Alternatively, Cl-based additives may be another way to facilitate Cl-incorporation into the perovskite lattice. HCl,[210−212] NH_4Cl,[213] $CaCl_2$,[214] tetraphenylphosphonium chloride (TPPCl),[215] and butylphosphonic acid 4-ammonium chloride (4-ABPACl)[216] additives were reported to play an important role in the formation of high quality films as well as enhancement of device stability; however, the question whether chloride ions enter the perovskite crystal lattice is still under debate.[217]

To our knowledge, there are only two reports focusing on the FAPb(I/Cl) system.[218,219] Lv et al.[218] employed the one-step method by mixing $PbCl_2$ and FAI in a molar ratio of 1:3 in DMF followed by stirring at 60 °C for 30 min. The solution was spin coated on FTO/c-TiO_2/mp-TiO_2, and the $FAPbI_{3-x}Cl_x$ films were formed by postannealing in an oven at a temperature ranging from 120 to 170 °C for 30 min. Based on XRD data, annealing at 140 °C generated $FAPbI_{3-x}Cl_x$ perovskite in the tetragonal phase (space group $P3m1$, $a = b = 8.977(7)$ Å, $c = 10.890(2)$ Å). A slight c lattice parameter contraction of ~1.1% compared to the $FAPbI_3$ perovskite ($a = b = 9.000(8)$ Å, $c = 11.012(2)$ Å) was attributed to the partial substitution of Cl^- into the perovskite structure. EDX was also employed to estimate the chlorine content, but it was barely detectable.[218] Wang et al.[219] employed NH_4Cl, MACl, and FACl additives to suppress the formation of yellow δ-phase

DOI: 10.1021/acsami.7b06001
ACS Appl. Mater. Interfaces XXXX, XXX, XXX−XXX

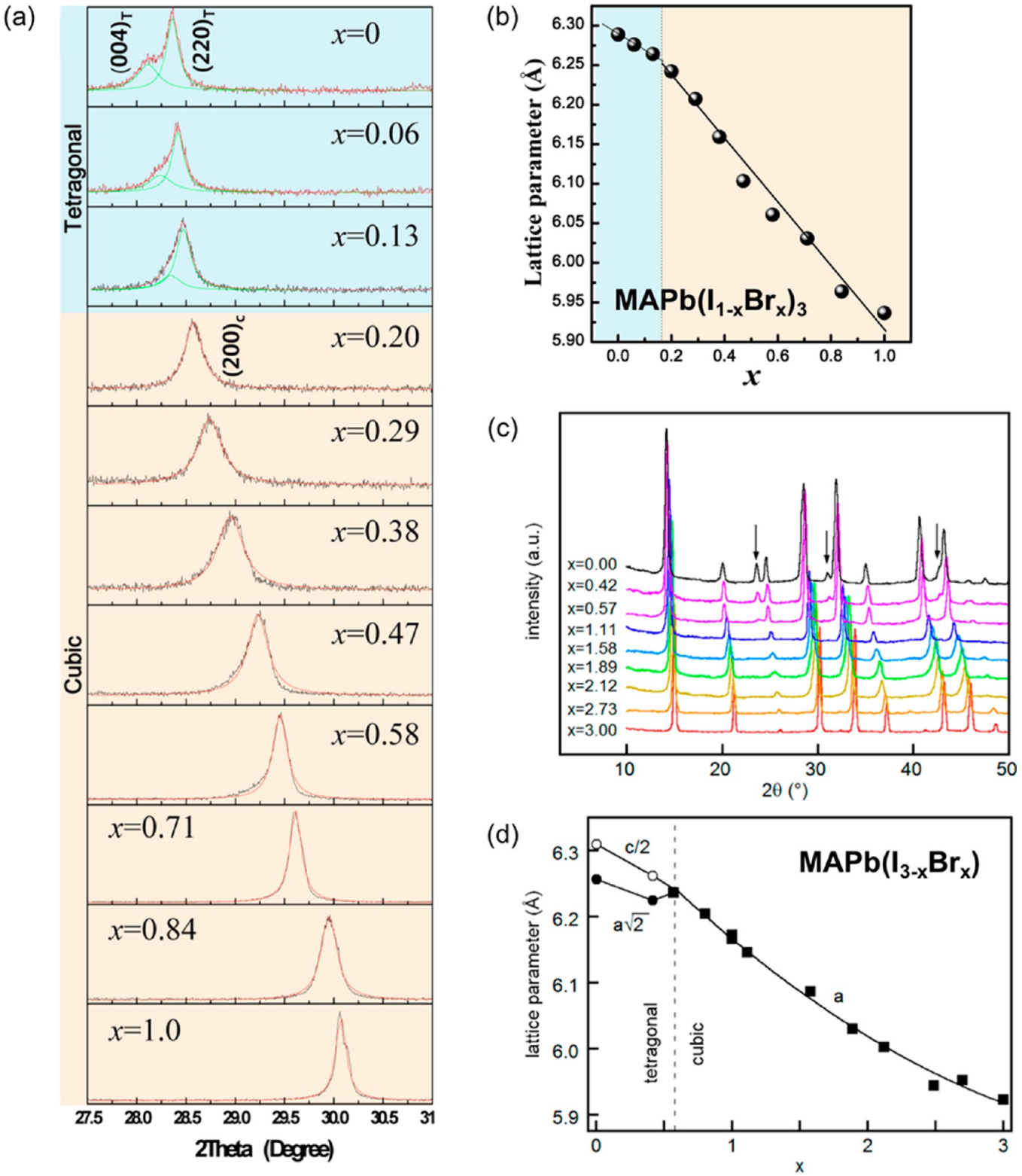

Figure 12. (a) Narrow-range XRD pattern of MAPb(I/Br) perovskites with varying Br:I molar ratio concentrations magnified in the region of the tetragonal $(004)_T$ and $(220)_T$ and cubic $(200)_C$ peaks. (b) Lattice constants of pseudocubic or cubic as a function of Br:I molar ratio concentrations. (c) Wide-range XRD pattern of MAPb(I/Br) perovskites and (d) extracted lattice parameters. (a,b) Reprinted with permission from ref 220. Copyright 2013 American Chemical Society. (c,d) Reprinted with permission from ref 226. Copyright 2015 American Chemical Society.

$FAPbI_3$. It has been proposed that suppressing the formation of δ-$FAPbI_3$ phase at all stages of the formation of $FAPbI_3$ on mp-TiO_2 is essential for achieving high-purity black α-$FAPbI_3$ perovskite phase.

3.2. Binary MAPb(I/Br) and FAPb(I/Br) Systems.

Contrary to the MAPb(I/Cl) material system described in section 3.1, the substitution of I^- by Br^- ions has been widely demonstrated and to effectively tune the band gap of

DOI: 10.1021/acsami.7b06001
ACS Appl. Mater. Interfaces XXXX, XXX, XXX−XXX

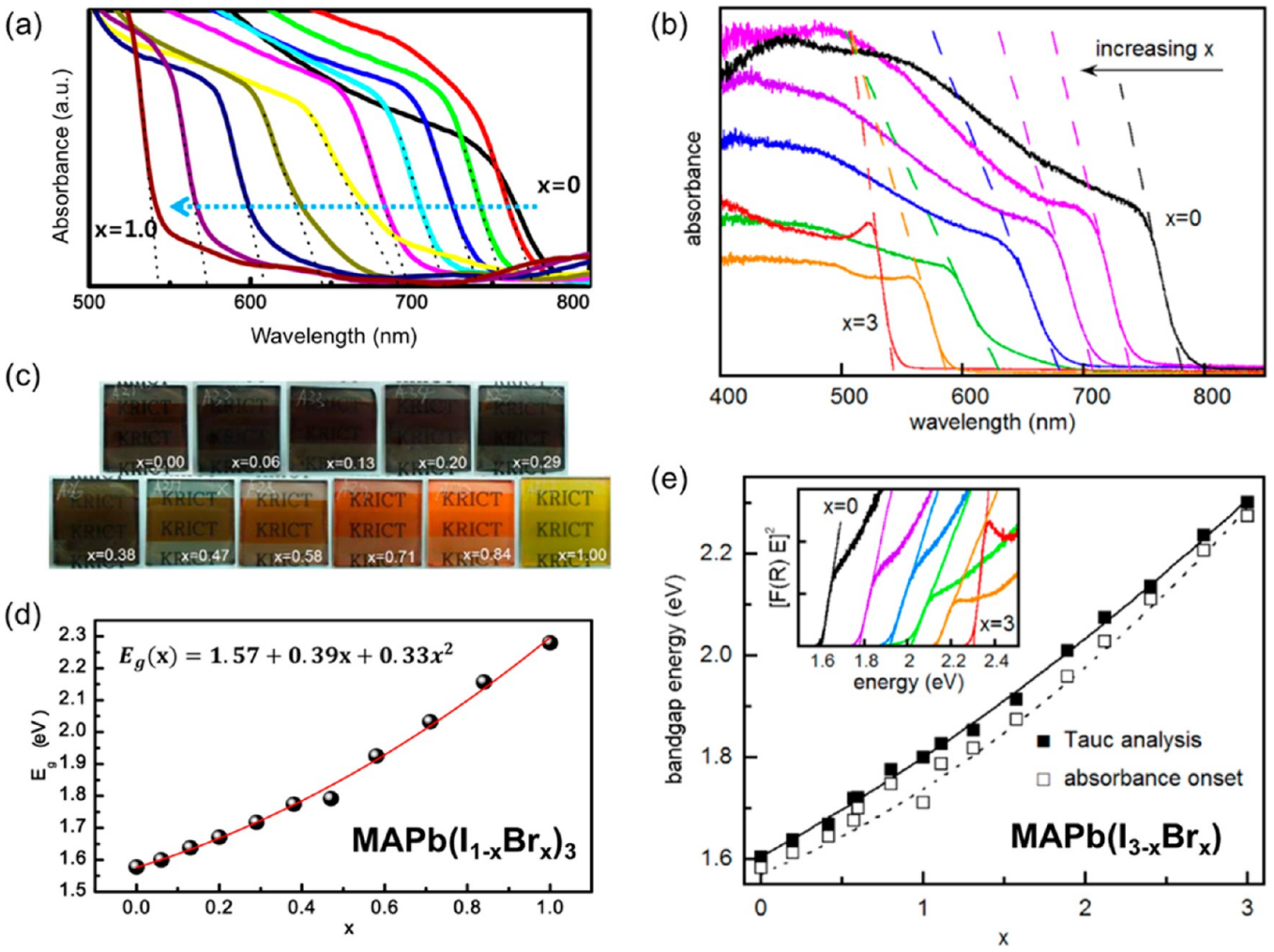

Figure 13. (a,b) UV−vis absorbance spectra of MAPb(I/Br) perovskites with varying Br:I molar ratio concentrations. (c) Photographs of MAPb(I/Br) perovskite films. (d,e) Band gap energies as a function of Br:I concentrations extracted from the absorbance onsets and Tauc analysis. Inset in (e) shows representative Tauc plots used to determine E_g. (a,c,d) Reprinted with permission from ref 220. Copyright 2013 American Chemical Society. (b,e) Reprinted with permission from ref 226. Copyright 2015 American Chemical Society.

perovskites.[220] The photovoltaic properties of mixed MAPbI$_{3-x}$Br$_x$ were first demonstrated by Noh et al.[220] reporting an efficiency of 12.3%. Jeon et al.[62] achieved a certified PCE of 16.2% (Figure 1b) by the solvent-engineering method, which enables the deposition of uniform and dense perovskite films of MAPbI$_{3-x}$Br$_x$ (x = 0.10−0.15). Later alternative deposition methods such as vacuum deposition,[221] low-pressure vapor-assisted solution (LP-VASP),[222] and printing[223] have been demonstrated. In the work by Noh et al.,[220] the Br content (<10%) gave the best initial efficiency due to a lower band gap, but higher Br contents (>20%) provided a better high-humidity shelf life stability (RH 55%). This was correlated with a tetragonal to pseudocubic structural transition (at x = 0.13) arising from a higher t factor due to the smaller ionic radius of Br (Figure 12). Mixed perovskites composed of two different perovskite crystals with similar lattice constants follow the Vegard's law. According to this law, a linear dependence of the lattice parameter with composition is expected, in the absence of strong electronic effects.[220,224−228] Fedeli et al.[226] claimed that in the cubic regime ($x \geq 0.57$, MAPbI$_{3-x}$Br$_x$), a small deviation from the Vegard's law was observed indicating additional interactions in the mixed-halogens (Figure 12d). Furthermore, a blue-shift of the absorption edge, i.e., increase in band gap following a quadratic function of the Br content was extracted from absorbance onsets, $E_g(x) = 1.57 + 0.39x + 0.33x^2$ (eV) by Noh et al.[220] (Figure 13a,c,d). Fedeli et al.[226] emphasized that slight variations (a few tens of meV) in E_g values are obtained when derived from the Tauc analysis and compared to E_g values extracted from the absorbance onset (Figure 13b). The $E_g(x)$ expression that is independent of the film properties (thickness, surface roughness related scattering) was derived based on Tauc plots (Figure 13e):

$$E_g(x) = E_{I3} + (E_{Br3} - E_{I3} - b)\frac{x}{3} + b\left(\frac{x}{3}\right)^2 \quad (3)$$

where E_{I3} and E_{Br3} are the bandgaps of MAPbI$_3$ (1.604 eV) and MAPbBr$_3$ (2.307 eV), respectively, and b (0.175 eV) is the so-called bowing parameter that accounts for the effects of composition disorder on the conduction and valence band edges. Based on the low b value extracted, the authors concluded that compositional disorder is low in MAPb(I/Br) perovskites (Figure 14a). Based on DFT calculations, Mosconi et al.[206] proposed that Br can occupy both apical and equatorial positions in the PbX$_6$ octahedra. Based on combined first-principles total energy calculations with statistical mechanical treatments (evoking the energy and entropy of mixing), Brivio

DOI: 10.1021/acsami.7b06001
ACS Appl. Mater. Interfaces XXXX, XXX, XXX−XXX

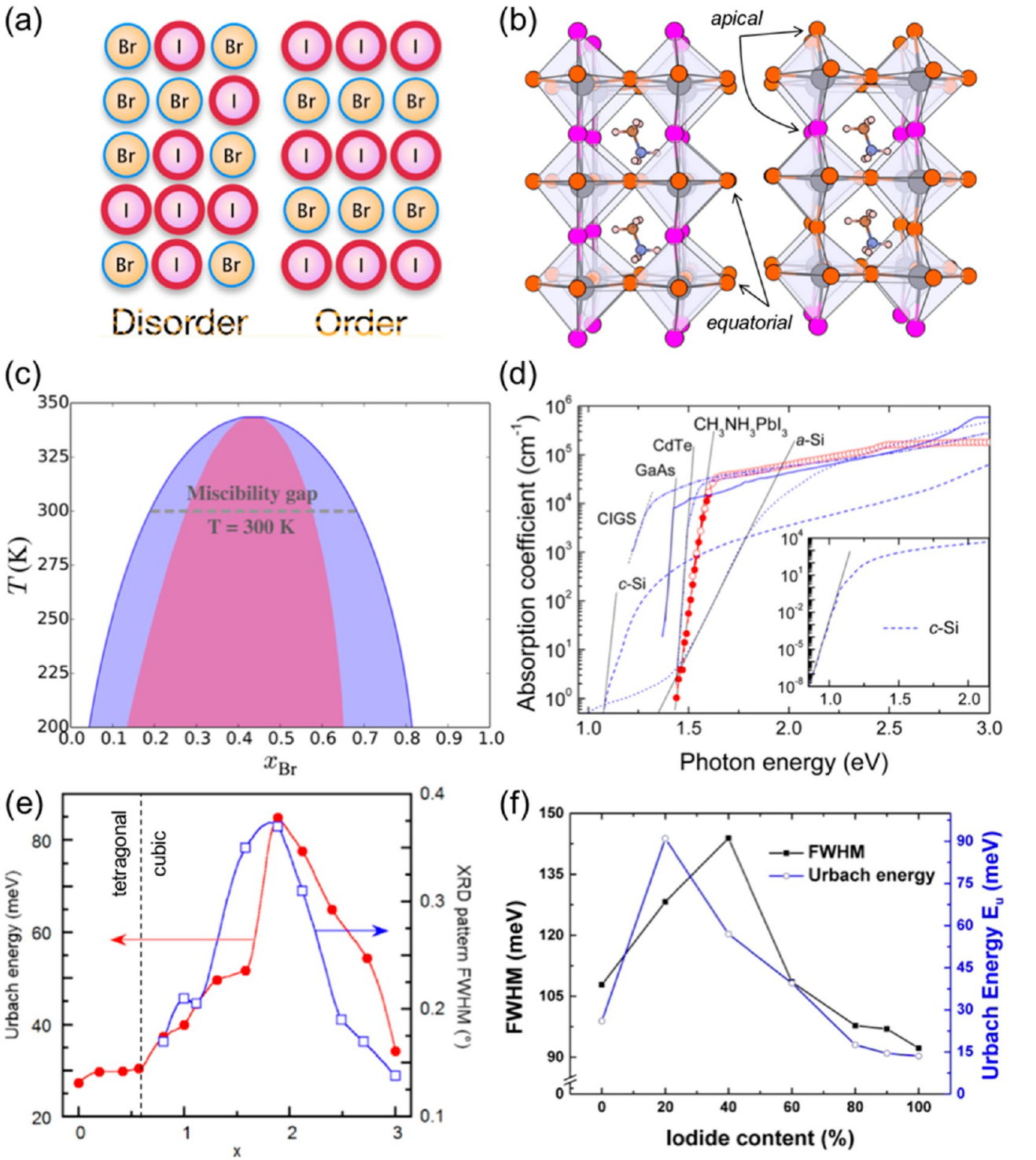

Figure 14. (a) Schematic illustration of disordered and ordered systems in MAPb(I/Br). (b) Identified stable ordered structures for $MAPbIBr_2$ and $MAPbI_{1/2}Br_{5/2}$ (layered with iodine at the apical positions) that minimize internal strain arising from the size mismatch between I and Br. (c) Calculated phase diagram of $MAPb(I_{1-x}Br_x)_3$ alloy. Purple and pink lines are binodal and spinodal lines, respectively. The dashed horizontal line corresponds to miscibility gap at room temperature. Thermodynamically stable alloy can be formed only in the white region. Reprinted with permission from ref 229. Copyright 2016 American Chemical Society. (d) Effective absorption coefficient of $MAPbI_3$ perovskite compared with other technologically relevant photovoltaic materials, amorphous-silicon (a-Si), GaAs, CIGS, CdTe, and crystalline silicone (c-Si), all corresponding to room temperature measurements. For each material, the slope of the Urbach tail is shown. The inset shows the data for c-Si down to low absorption values. Reprinted with permission from ref 230. Copyright 2014 American Chemical Society. (e) Urbach energy and fwhm of the XRD pattern in the cubic phase composition range as a function of Br:I molar ratios in MAPb(I/Br) perovskites. Reprinted with permission from ref 226. Copyright 2014 American Chemical Society. (f) Urbach energy and fwhm of the PL peak as a function of iodine concentration in MAPb(I/Br) perovskites. Reprinted with permission from ref 231. Copyright 2014 American Chemical Society.

DOI: 10.1021/acsami.7b06001
ACS Appl. Mater. Interfaces XXXX, XXX, XXX−XXX

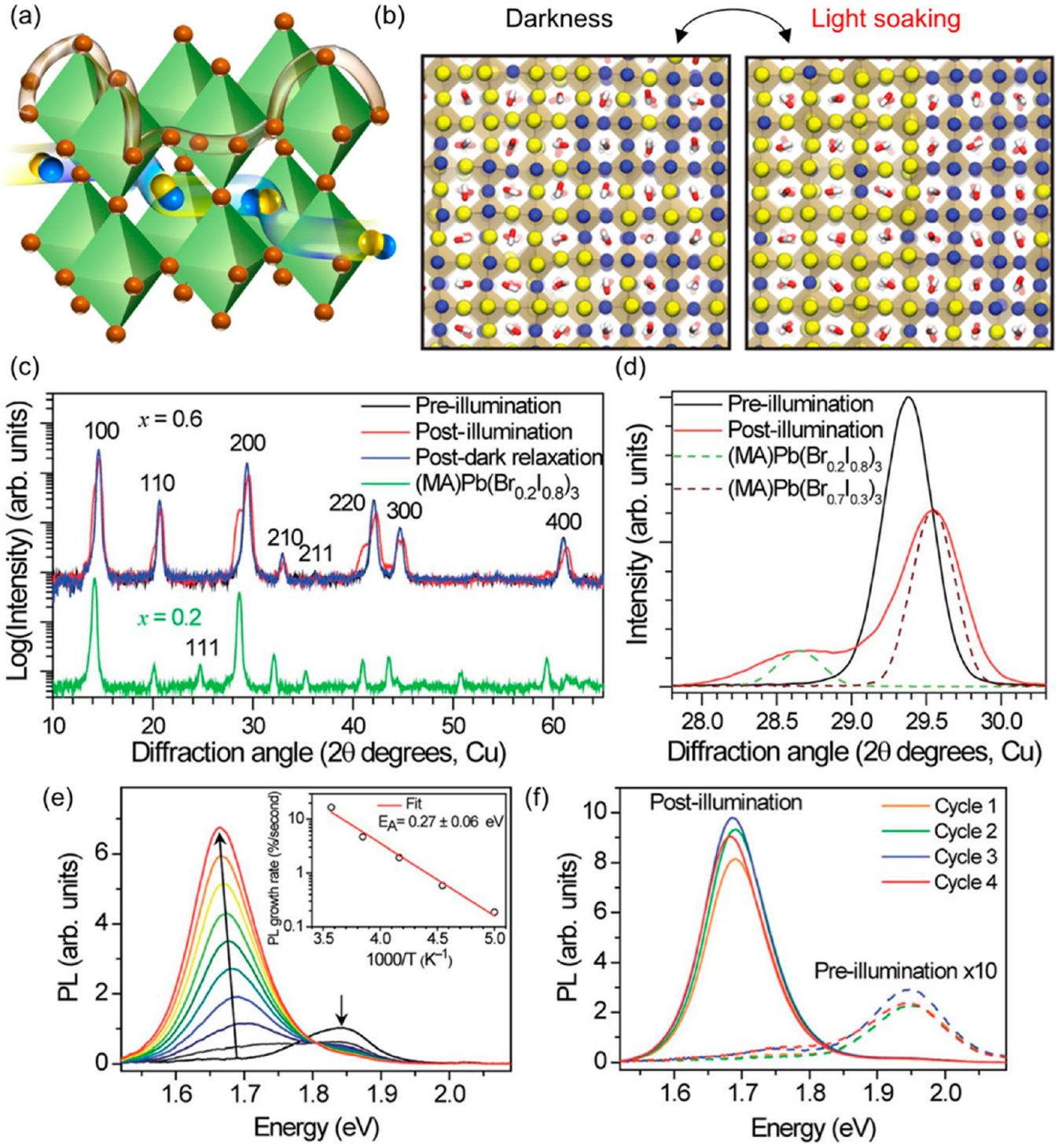

Figure 15. (a) Illustration of proposed migration path of I^- ions along the I^--I^- edge of the PbI_6 octahedra in $MAPbI_3$. MA^+ migration was also corroborated experimentally. Reprinted with permission from ref 232. Copyright 2016 American Chemical Society. (b) Schematic illustration of phase separation (Light soaking) and reversibility (darkness) in MAPb(I/Br) system, where yellow and blue spheres represent I^- and Br^-, respectively; the red and white pill shapes represent MA. Reprinted with permission from ref 233. Copyright 2017 American Chemical Society. (c) XRD pattern of $MAPbBr_{0.6}I_{0.4}$ film before (black) and after (red) white-light soaking (~50 mW/cm^2; ~0.5 sun) for 5 min, and subsequently after 2 h in the dark (blue). XRD of $MAPbBr_{0.2}I_{0.8}$ (green) is shown for comparison. (d) (200) XRD peak of $MAPbBr_{0.6}I_{0.4}$ film before (black) and after (red) white-light soaking (~50 mW/cm^2) for 5 min. XRD of $MAPbBr_{0.2}I_{0.8}$ (dashed green) and $MAPbBr_{0.7}I_{0.3}$ (dashed brown) are shown for comparison. (e) PL spectra of $MAPbBr_{0.4}I_{0.6}$ film over 45 s in 5 s increments under 475 nm, 15 mW/cm^2 at 300 K. Inset shows temperature dependence of initial PL growth rate. (f) PL spectra of $MAPbBr_{0.6}I_{0.4}$ film after sequential cycles of illumination (475 nm, 15 mW/cm^2) for 2 min followed by 5 min in the dark. Reprinted with permission from ref 234. Copyright 2015 The Royal Society of Chemistry.

et al.[229] identified the two most stable configurations corresponding to ordered structures of $MAPbIBr_2$ and $MAPbI_{1/2}Br_{5/2}$ (Figure 14b). Both structures were formed with iodine ions located at the apical locations. Furthermore,

DOI: 10.1021/acsami.7b06001
ACS Appl. Mater. Interfaces XXXX, XXX, XXX−XXX

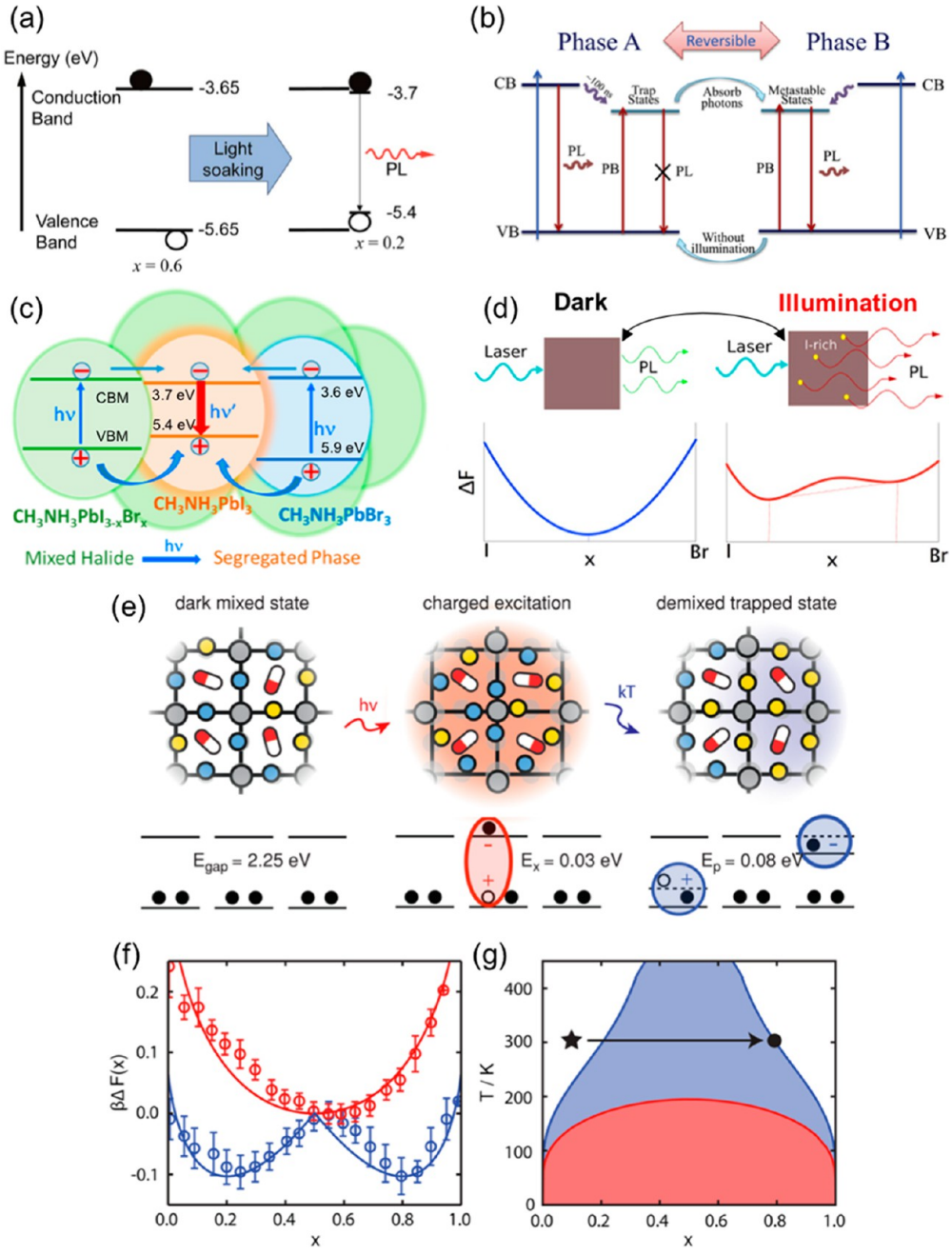

Figure 16. (a) Illustration of proposed mechanism for photoinduced trap states formation within the band gap in $MAPbBr_{0.4}I_{0.6}$. Photogenerated holes or excitons are hypothesized to stabilize the formation of iodine-rich domains (e.g., $MAPb(Br_{0.2}I_{0.8})_3$) that dominate PL. Reprinted with permission from ref 234. Copyright 2015 The Royal Society of Chemistry. (b) Illustration for the proposed two-step mechanism for light induced segregation: initial photon absorption will generate trap states in the band gap after 100 ns; these traps have lifetime of 1 μs (Phase A). If subsequent coming photons are absorbed by these traps, it transforms to a metastable state (Phase B), which behave as new energy band and can lead to PL emission. Reprinted with permission from ref 235. Copyright 2016 Elsevier Ltd. (c) Illustration of MAPb(I/Br) with each of the domains (iodide- and bromide-rich) having characteristic conduction band minimum (CBM) and valence band maximum (VBM) values will lead to iodide-rich domains to serve as sinks for the photogenerated charge carriers. Reprinted with permission from ref 236. Copyright 2016 American Chemical Society. (d) Schematic Helmholtz free-energy (ΔF) curves in light and in dark predicting phase segregation. The red vertical dashed lines show that the lowest attainable free energy in light occurs when the material segregates into I-rich and Br-rich phases, whereas the blue dashed line shows that the lowest energy corresponds when the material remains in a single phase in dark. Reprinted with permission from ref 237. Copyright 2016 American Chemical Society. (e) Photoinduced polaron trapping and associated energy scales. Yellow and blue spheres represent I^- and Br^-, respectively; the red and white pill shapes represent MA. Lead atoms represented by gray circles. (f) Free energies per unit cell for $MAPb(I_xBr_{1-x})_3$ with varying composition in the ground (red) and photoexcited (blue) states, computed from MD simulations (circles) and mean field theory (solid lines). (g) Temperature−composition phase diagram in the ground (red) and photoexcited state (blue). Areas beneath the red and blue coexisting curves indicate demixed states. The arrow through the phase diagram from initial state (star) to demixed state (circle) correspond to experimental observation for $MAPb(I_{0.1}Br_{0.9})_3$. Reprinted with permission from ref 233. Copyright 2017 American Chemical Society.

DOI: 10.1021/acsami.7b06001
ACS Appl. Mater. Interfaces XXXX, XXX, XXX−XXX

based on the Helmholtz free energy variation, a phase diagram of MAPb(I/Br) was constructed predicting that (i) there is a critical temperature of ~343 K, above which the solid solution is stable for any Br/I composition; (ii) at 300 K, the alloy is not stable against a phase separation in $MAPbI_3$ and $MAPbBr_3$ in the range of compositions between $0.19 < x < 0.68$ (miscibility gap). The lattice constant mismatch (~6%) between $MAPbI_3$ and $MAPbBr_3$ was associated with the instability of isovalent solid solutions.[229]

Further investigations regarding disorder dependence on Br:I ratio were conducted by analyzing the exponential decay of the sub-band gap absorbance, commonly described by the empirical Urbach rule, $A \propto \exp(E/E_0)$, where A is absorbance, E photon energy, and E_0 the characteristic Urbach energy representing the width of the exponential Urbach tail (Figure 14d).[226,230,231] Despite the fact that there is no theoretical derivation for the Urbach rule, a general consensus exists that the Urbach tail in crystalline semiconductors is related to the static (structural disorder) and/or dynamic (phonon) disorder, that arises from lattice point defects, dislocations, strain, deviation from ideal stoichiometry, and grains.[226,230,231] Pure $MAPbI_3$ and $MAPbBr_3$ perovskites were determined to have sharp absorption edges with low Urbach energy of ~15−27 meV and ~23−34 meV, respectively.[226,230,231] Compared with other semiconductors (Figure 14d), the Urbach energy of $MAPbI_3$ is close to the value of GaAs (monocrystalline direct band gap semiconductor). Crystalline Si (c-Si) shows also a similar slope below its bandgap, but because of its indirect band gap, it occurs at much a lower value and shows signatures related to phonon-assisted absorption (inset in Figure 14d). The disorder evaluated on $MAPbI_{3-x}Br_x$ perovskites through the Urbach energy showed larger values reaching a maxima of ~85 meV ($MAPbI_{1.12}Br_{1.88}$, Figure 14e)[226] and ~90 meV ($MAPbI_{1.2}Br_{1.8}$, Figure 14f).[231] Interestingly, the dependence of x with these Urbach energies was closely related to grain-size domains (Figure 14e), and it was suggested that the sub-band gap absorption is due to defect states localized at the grain boundaries.[226] It was also shown that the fwhm of the photoluminescence (PL) peaks are correlated with the Urbach energies (Figure 14f). This observation indicates that absorption and emission arise from similar states.[231] Also, the larger PL fwhm and Urbach energy with iodine concentrations of 20−40% (Figure 14f) was observed to correlate with shorter lifetimes observed in transient PL.[231]

Although under storage conditions the MAPb(I/Br) system exhibits enhanced stability, it has been reported that dynamical processes (e.g., material degradation and phase segregation) takes place when exposed to light. Misra et al.[227] performed photochemical stability tests of encapsulated films of $MAPbI_{3-x}Br_x$ (x = 0.11, 0.16, 0.22, 1) under accelerated stressing conditions using concentrated sunlight (100 suns). They observed that $MAPbBr_3$ was the most stable composition exhibiting no degradation, whereas increasing iodine incorporation leads to accelerated photochemical degradation yielding PbI_2 as a final remaining product. No degradation was recorded for $MAPbI_{3-x}Br_x$ under shelf-storage conditions, and degradation was observed to occur only under illumination conditions. Currently, it is widely accepted that ion migration is one of the causes for the anomalous photocurrent hysteresis phenomena (Figure 15a).[232,238,239] In addition, there are also concerns that ion migration is closely correlated with inherent instability issues in perovskite solar cells. For example, Hoke et al.[234] reported first on the occurrence of a serious phase segregation in MAPb(I/Br) films under illumination (coined as Hoke effect[237,240]). The initially homogeneous $MAPb(Br_xI_{1-x})_3$ ($0.2 < x < 0.9$) perovskite films were observed to undergo photoexcited phase-separation into two phases, one iodine-rich and the other bromide-rich domain in the same film (Figure 15b), as corroborated by the peak splitting probed in XRD (Figure 15c,d) and PL (Figure 15e,f) measurements. As shown in Figure 15d, when the $MAPb(Br_{0.6}I_{0.4})_3$ film was illuminated with white light, the original diffraction pattern splits into two peaks, suggesting formation of phases with larger and smaller lattice constants. More interestingly, when allowed to relax in dark, the XRD pattern returned to its original, single phase state. Additional, PL (Figure 15f) and absorption spectra acquired before and after light soaking confirmed this reversibility (Figure 15b). Temperature dependence (200−300 K) was performed to verify that phase segregation occurs solely due to illumination and not from temperature increase during illumination (Figure 15e). Although phase segregation (disappearance of the original peak and rise of new lower-energy peak) was observed at the lowest temperature of 200 K, the time scale for the changes varied widely. The changes occurred in ~1 min at 300 K, whereas at 200 K the phase segregation took ~1 h to complete. The Arrhenius plot behavior (inset in Figure 15e) was observed for this phase segregation, where an activation energy of ~0.3 eV was extracted. Interestingly, this value is similar to halide ion migration activation energies reported previously, supporting further that ionic transport plays a major role in perovskite solar cells (Figure 15a,b).[232,234,237] It is emphasized that even without light illumination, the PL peak position was observed to shift in $MAPbBr_{1.2}I_{1.8}$ films from 1.68 to 1.94 eV after 2 weeks storage under dark and inert environment.[231] This was attributed to a slow, but spontaneous room temperature phase segregation within the miscibility gap (Figure 14c).[229]

A number of reports proposed the microscopic origins for the phase-segregation phenomena.[74,233−237,240] Hoke et al. proposed that the existence of initial iodide-rich domains (nucleation points) in as prepared MAPb(I/Br) samples stabilizes hole accumulation upon illumination (Figure 16a). These accumulation of unbalanced charges (holes) provide further driving enthalpy for halide segregation growing further the iodide-rich domain sizes (Figure 15d,e). Yang et al.[235] employed PL and photomodulation (PM) spectroscopy to study the $MAPbBr_{1.7}I_{1.3}$ films. Using continuous wave (CW) or 10 ns pulsed laser with high repetition rates, they observed that the initial PL ~ 640 nm (~1.94 eV) peak position shifted to a longer wavelength of ~750 nm (~1.65 eV) after illumination.[235] Interestingly, with the same 10 ns pulsed laser, but using lower repetition rates (<500 Hz), no matter what the intensity of excitation light is, PL did not show shift in peak position. Based on CW pump probe spectroscopy and transient dynamics, Yang et al. proposed a two-step process: initial photon absorption will generate trap states within the band gap, but these traps will not lead to PL emission; these traps have lifetime of 1 μs (Phase A). If subsequent incident photons are absorbed by these traps within the lifetime, it transforms to a long-lived (~ms) "metastable" state (Phase B), which behaves as new energy band and can lead to PL emission (Figure 16b). These polar states (later identified as polaronic states[233]) were hypothesized to locally drive ion migration. Yoon et al.[236] proposed that MAPb(I/Br) with each of the domains (iodide- and bromide-rich) having characteristic conduction band minimum (CBM) and valence band maximum (VBM) values

DOI: 10.1021/acsami.7b06001
ACS Appl. Mater. Interfaces XXXX, XXX, XXX−XXX

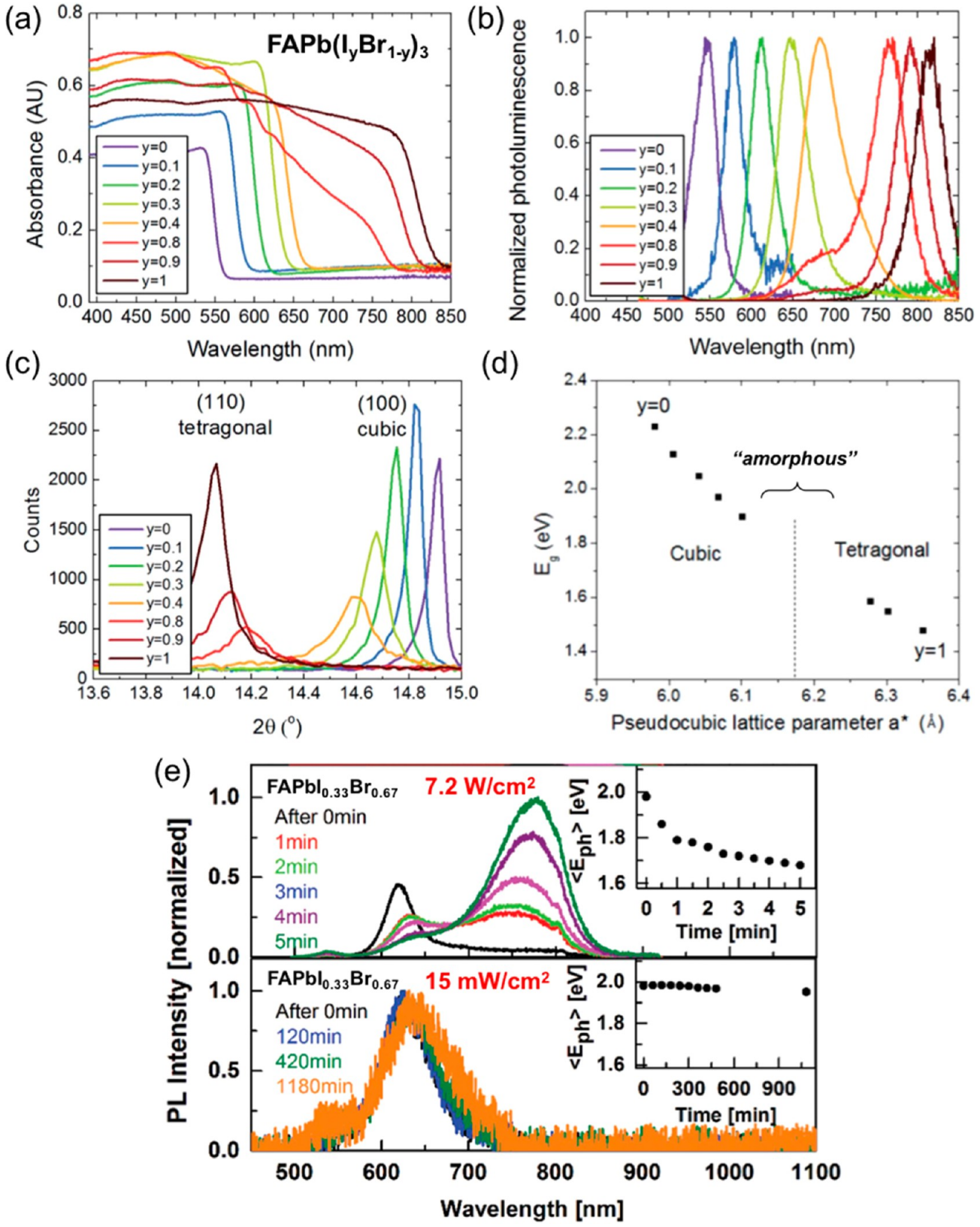

Figure 17. (a) UV−vis absorbance, (b) steady-state PL spectra, (c) XRD of $FAPbI_xBr_{3-x}$ perovskites with varying x composition. (d) Variation of band gap as a function of pseudocubic lattice parameter extracted from XRD data. Reprinted with permission from ref 147. Copyright 2014 The Royal Society of Chemistry. (e) PL spectra of $FAPb(Br_{0.67}I_{0.33})_3$ film over 5 min of continuous illumination following excitation at 400 nm with intensity of 7.2 W/cm^2 and 15 mW/cm2. Inset: Change of the average photon energy (E_{ph}) as a function of time. Reprinted with permission from ref 242. Copyright 2015 WILEY-VCH Verlag GmbH & Co. KGaA, Weinheim.

DOI: 10.1021/acsami.7b06001
ACS Appl. Mater. Interfaces XXXX, XXX, XXX−XXX

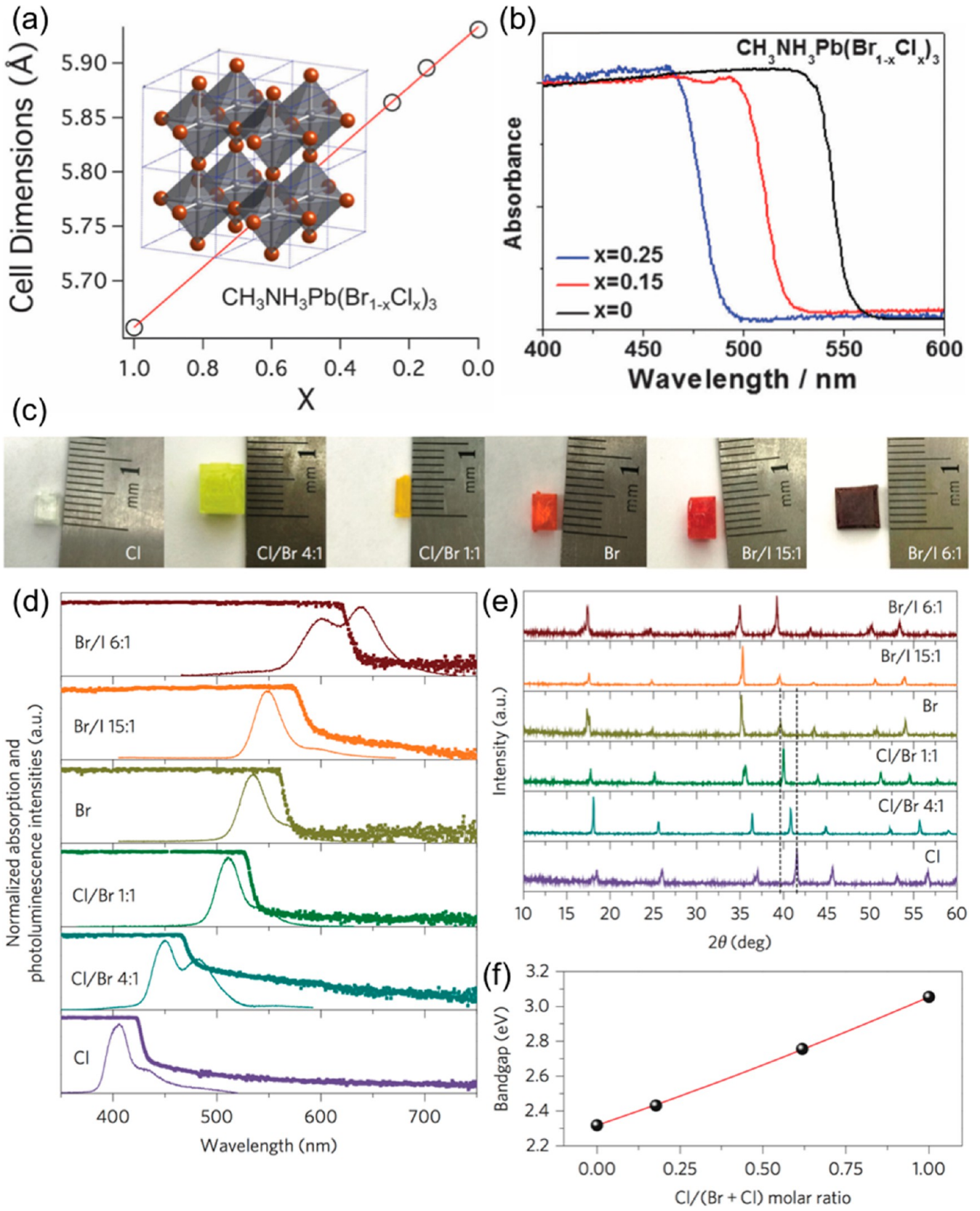

Figure 18. (a) Single crystal XRD cell dimensions and (b) UV−vis absorption spectra for $MAPb(Br_{1-x}Cl_x)_3$ (x = 0, 0.15, 0.25). Reprinted with permission from ref 247. Copyright 2015 The Royal Society of Chemistry. (c) Photographs of MAPb(Br/Cl) and MAPb(B/I) mixed halide perovskite single crystals with different halide compositions. (d) Absorption and PL spectra. (e) Powder XRD. (f) Crystal band gap extracted from PL as a function of Cl/(Cl + Br) molar ratio derived from XRD. Reprinted with permission from ref 246. Copyright 2015 Nature Publishing Group.

DOI: 10.1021/acsami.7b06001
ACS Appl. Mater. Interfaces XXXX, XXX, XXX−XXX

will lead to iodide-rich domains to serve as charge recombination sites and thus contribute to the observed PL emission (Figure 16c). Slotcavage et al.[237] discussed the thermodynamic origins of observed light-induced phase segregation (Figure 16d). Bischak et al.[233] performed combined cathodoluminescence (CL) mapping to visualize the spatial segregation into iodide- and bromide-rich domains. After prolonged illumination, small clusters enriched in iodide were observed to localize near grain boundaries. Their molecular dynamics (MD) simulations were able to demonstrate that photoinduced phase separation arises when charged excitations generate enough lattice strain to destabilize the solid solution, favoring phase-segregation. Their findings show that upon light absorption weakly bound electron−hole pair (binding energy ∼0.03 eV) quickly dissociates into free carriers (Figure 16e). Due to the ionic nature of the perovskite, these charges deform the surrounding lattice through electron−phonon coupling. The charge and the lattice deformation field that surrounds together form a polaron that was predicted to have an average size of 8 nm and binding energy of E_p = 0.08 eV (Figure 16e).[233] This polaron-induced lattice distortion changes the magnitude of the free energy as a function of bromide content from one with one minimum (in dark, red curve in Figure 16f) to another with two minima (under illumination, blue curve in Figure 16f). They also determined a full temperature−composition phase diagram for both ground- and photoexcited states (Figure 16g). This graph shows that for $MAPb(I_{0.1}Br_{0.9})_3$ film (star symbol in Figure 16g), temperature variation over a range of 50 K was insufficient to induce demixing, but does increase the demixing rate under light illumination (circle in Figure 16g). Their model suggests that naturally occurring small variations in perovskite composition that exists before illumination will yield iodide-rich domains that has a reduced band gap. Therefore, perovskite compositional homogeneity seems to be one of the determining factors that will favor stability.[233,237,240] It has been shown that photoinduced phase segregation is minimized in highly crystalline perovskites.[241]

Similarly, mixed halide $FAPbI_{3-x}Br_x$ perovskites were also synthesized with x varying from 0 to 1.[147,242] Interestingly, both reports described that they were unable to form crystalline phases of $FAPb(I_{1-x}Br_x)_3$ perovskites with bromide contents in the range $0.3 < x < 0.5$, as it was apparent from the absence of significant UV−vis, PL, and XRD data (Figure 17a−d). The term "amorphous"[242] was used implying that the crystalline order is too short in the length scale detectable by XRD (Figure 17d).[147] Fundamental origins for this amorphous regime have not been fully clarified. Phase segregation phenomena in iodide- and bromide-rich domains were also reported for the FAPb(I/Br) system.[234] Rehman et al.[242] reported that the intensity of the laser excitation spot played a major role in producing phase segregation (Figure 17e). The PL emission of $FAPb(Br_{0.67}I_{0.33})_3$ films recorded for laser excitation with an intensity of 7.2 W/cm^2 following 5 min of continuous illumination showed the gradual decrease and shift of the 620 nm (∼2 eV) to a new dominant low-energy PL feature at ∼785 nm (1.58 eV). On the other hand, when an identical $FAPb(Br_{0.67}I_{0.33})_3$ film was illuminated at the same wavelength (400 nm) with lower laser intensity of 15 mW/cm^2, no changes in PL spectra were observed even after 1180 min (∼20 h) exposure (Figure 17e). Compared to the MAPb(I/Br) system, it was reported that light intensity as low as 1.2 mW/cm^2 with continuous illumination (10 min) can induce phase segregation.[235] Because photovoltaic devices are typically tested under AM1.5 conditions (100 mW/cm^2), strategies to make both MAPb(I/Br) and FAPb(I/Br) systems resilient to phase segregation phenomena is needed.

3.3. Binary MAPb(Br/Cl) System. Contrary to the MAPb(I/Cl) system described in section 3.1, Cl was confirmed to coexist with I in the MAPb(Br/Cl) system.[243−249] Theoretical calculations determining the phase transitions of temperature-halide compositions showed a relatively low demixing critical temperature for MAPb(Br/Cl) system (∼140 K), which was similar to that of MAPb(Br/I) system (∼190 K).[233] In comparison, for the MAPb(I/Cl) system, the determined critical solution temperature of ∼1800 K was well above room temperature, explaining why this mixture is unstable.[233] The larger difference in ionic radii, Cl^- (1.67 Å) < Br^- (1.84 Å) < I^- (2.07 Å)[250] and the higher degree of ionic character is explained as origin for the "easy" miscibility between (Cl/Br) and (Br/I) system, but not for the (Cl/I) system.[15,233,250] This is also reinforced by the fact that growth of halide mixed $MAPbBr_{3-x}Cl_x$ and $MAPbBr_{3-x}I_x$ single crystal perovskites is possible in the full range of Br:Cl and Br:I molar ratios confirming halide miscibilities (Figure 18).[17,217,246,247] The single crystals were synthesized from stoichiometric $PbBr_2$ and $[y\text{MACl} + (1 - y)\text{MABr}]$ precursor solutions in DMF by Zhang et al.[247] employing the solvothermal method, which is based on inverse solubility (Figure 18a,b). Fang et al.[246] employed the cooling-induced crystallization method to growth mixed halide perovskite single crystals (Figure 18c−f). The authors constructed photodetector devices based on these single crystals with a thickness of ∼1 mm. The response spectrum could be tuned from blue to red by varying the halide composition of these single crystals. The main advantage lies on the very narrowband fwhm (less than 20 nm) photodetection.[246] Among the family of mixed halide perovskites, $MAPbBr_{3-x}Cl_x$ has a larger band gap (Figure 18b,d,f) than that of iodine-based perovskites ($MAPbI_{3-x}Cl_3$ and $MAPbI_{3-x}Br_x$).[217] Therefore, most of works focused on perovskite light-emitting devices where the emission color could be tuned from the red to blue color by modulating the halide composition in the perovskite.[245,246,251−253]

3.4. Ternary MAPb(I/Br/Cl) System. A few reports describe the triple halide-mixed MAPb(I/Br/Cl) system.[254−256] Similar to what was discussed in section 3.1, the amount of Cl incorporated seems negligible. Nevertheless, Cl was shown to impact device performance by improving coverage and reducing crystal growth rate.[254−256] On the other hand, Br was observed to influence strongly the band gap of MAPb(I/Br/Cl) system and consequently increase open-circuit voltage (V_{oc}). In addition, Br incorporation was reported to stabilize crystal lattice improving lifetime of device. These influences of Br incorporation are similar to what was discussed in section 3.2. We observe that the ternary MAPb(I/Br/Cl) system resembles a linear combination of MAPb(I/Cl) + MAPb(I/Br) systems. Chiang et al.[256] synthesized MAPb(I/Br/Cl) perovskites by a combined hot solution spin-coating and solvent annealing film casting engineering obtaining high quality solid solution films. Their inverted solar cell devices (ITO/PEDOT:PSS/$MAPbI_{3-x-y}Br_xCl_y$/$PC_{61}BM$/Ca/Al) with active areas of 0.1 cm^2 generated J_{sc} = 19.25 mA/cm2, V_{oc} = 1.10 V, FF = 78%, PCE = 16.52% (the average efficiency from 34 devices yields a small standard deviation: PCE = 15.61 ± 0.84%). Furthermore, the same authors up-scaled the process and their designed inverted perovskite module composed of 9 cells in series with an active area of each cell equal to 4 mm ×

DOI: 10.1021/acsami.7b06001
ACS Appl. Mater. Interfaces XXXX, XXX, XXX−XXX

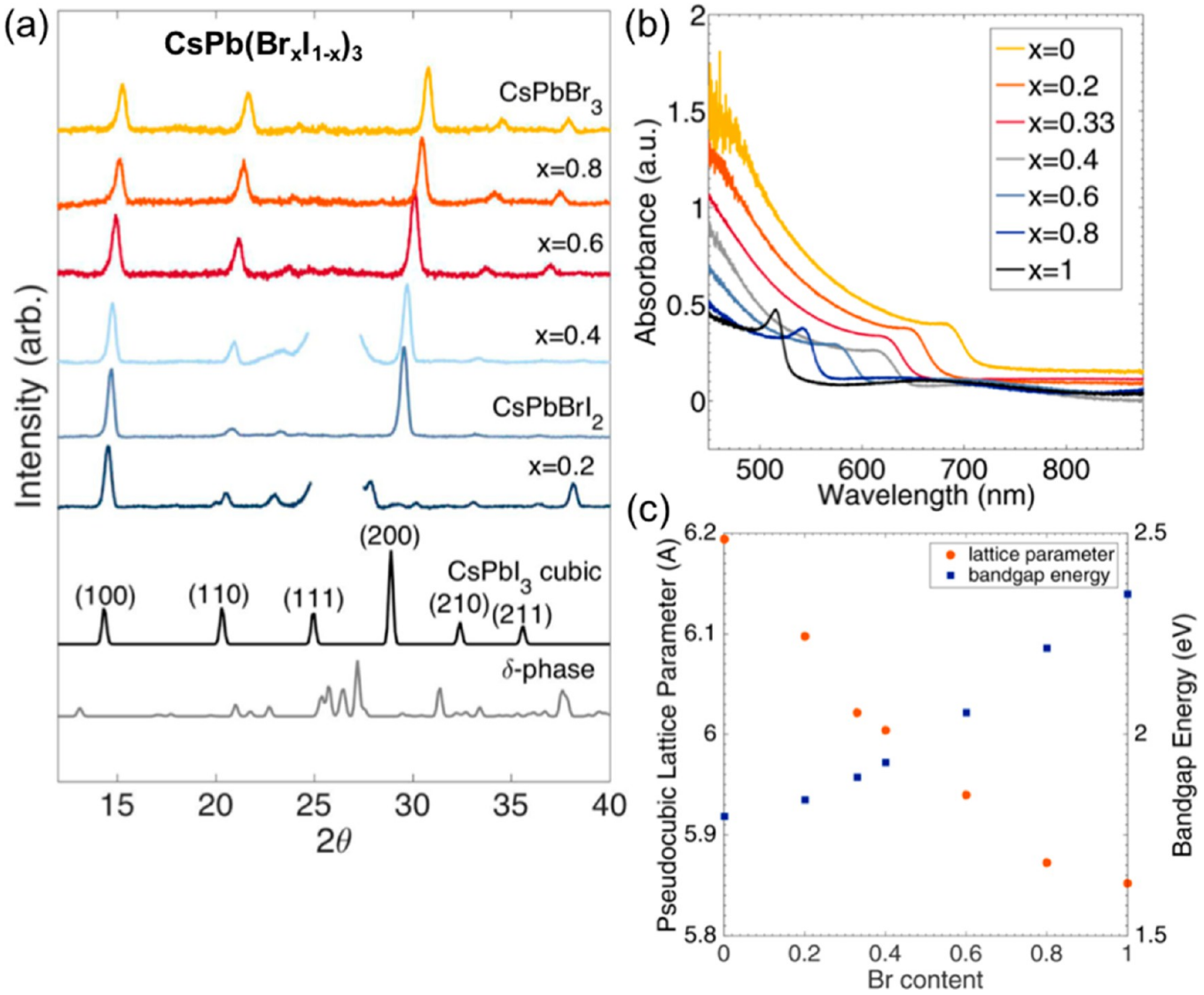

Figure 19. (a) XRD and (b) UV−vis absorption spectra for $CsPb(Br_xI_{1-x})_3$ ($0 \le x \le 1$) system. (c) Summary of lattice parameter changes based on the shift of the (100) peak and corresponding changes in the band gap energy extracted from the absorption onset. Reprinted with permission from ref 257. Copyright 2016 American Chemical Society.

70 mm (total active area = 25.2 cm^2) generated J_{sc} = 53.5 mA, V_{oc} = 9.05 V (average per each cell is 1.06 V), FF = 74.4%, overall PCE = 14.3%.[256]

3.5. Binary CsPb(I/Br), CsPb(Br/Cl), and CsPb(I/Cl) Systems. Recent reports bring additional relevant insights into the CsPb(I/Br) system (Figure 19).[98,250,257,258] For example, (i) contrary to the MAPb(I/Br) and FAPb(I/Br) systems (section 3.2), halide phase-segregation into iodide- and bromide-rich domains (or Hoke effect) was observed to be minimized for $CsPb(Br_xI_{1-x})_3$ films with low Br concentrations (x < 0.4).[257] However, for x > 0.4, phase separation was reported to occur under illumination (~1 sun). (ii) The $CsPbI_2Br$ in particular, was studied in more details due to its suitable band gap energy for photovoltaic applications. $CsPbI_2Br$ showed enhanced thermal stability when examined at 200 °C in an inert atmosphere[257] and under solar cell operation conditions (85 °C in air).[98] (iii) The addition of bromide reduces the phase transition temperature. Good thermal stability of $CsPbIBr_2$ alloy was also demonstrated at 200 °C in inert atmosphere.[258] The perovskite crystal forms at ~350 °C for $CsPbI_3$ and ~230 °C for $CsPbI_2Br$, meaning a reduction of over 100 °C in the transition temperature.[98] Device configuration of FTO/c-TiO_2/mp-TiO_2/$CsPbI_2Br$-(~150 nm)/spiro-MeOTAD/Ag was demonstrated to generate the best efficiency of 9.84%, with J_{sc} = 11.89 mA/cm^2, V_{oc} = 1.11 V, and FF = 75%.[98] Devices with an inverted structure, ITO/PEDOT:PSS/$CsPbI_2Br$(~150 nm)/PC60BM/BCP/Al, were shown to generate a PCE of 6.80%, J_{sc} = 10.9 mA/cm^2, V_{oc} = 1.06 V, and FF = PCE/(J_{sc} × V_{oc}) ~ 59%.[257]

Yin et al.[250] performed DFT calculations together with Monte Carlo simulations to systematically study the structural, electronic and energetic properties of mixed halide CsPb(I/Br), CsPb(Br/Cl), and CsPb(I/Cl) systems. They found that these perovskites exhibit anomalous alloy properties that differ from the conventional semiconductors (e.g., $GaAs_{1-x}Sb_x$). Generally, in conventional isovalent semiconductors, the formation energies are positive mostly attributed to the strain energy (e.g., original ideal A and B bulk materials are stretched or compressed to a new lattice constant of alloy $A_{1-x}B_x$). Halide perovskites have strong ionic character, so Coulomb

DOI: 10.1021/acsami.7b06001
ACS Appl. Mater. Interfaces XXXX, XXX, XXX−XXX

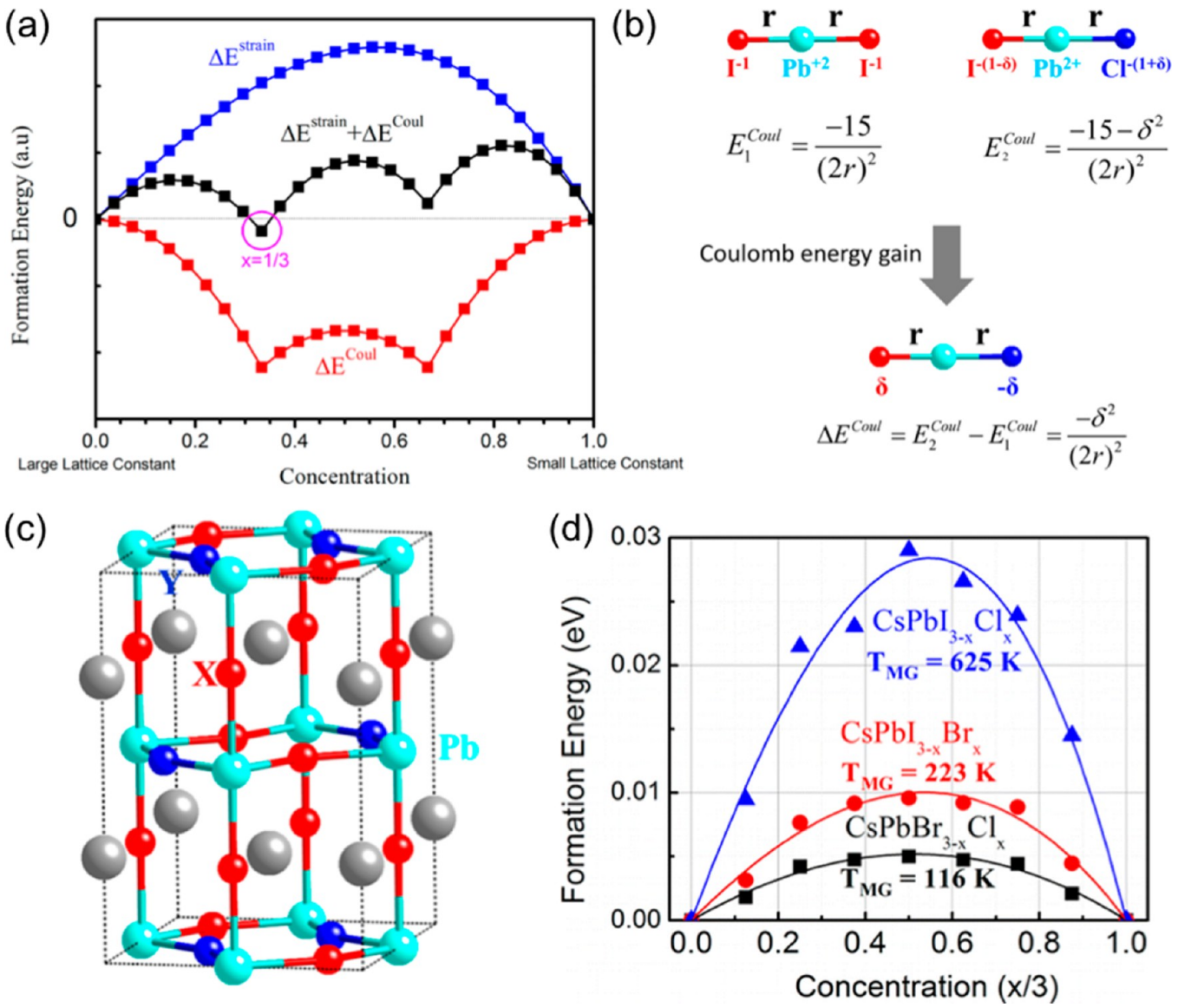

Figure 20. (a) Joint effects of strain (favoring demixing) and Coulomb (favoring mixing) energies for describing the formation energies of $CsPb(X_{1-x}Y_x)_3$ (X,Y = I, Br, Cl). This purely physical models lead the lowest energy at $x = 1/3$. (b) Model system (I−Pb−Cl trimer) shows the Coulomb energy gain process by charge transfer when halides are mixed. (c) Particular stable mixed-halide configuration for $CsPbX_{3-x}Y_x$ (X,Y = I, Br, Cl; atomic size of X > Y) at $x = 1$. (d) Formation energies (per halogen atom) of $CsPb(X_{1-x}Y_x)_3$ (X,Y = I, Br, Cl) alloys calculated based on special-quasirandom-structures (scattered points). The solid lines are fitting based on the nine different points per halogen atom. The miscibility gap temperatures (T_{MG}) are indicated. Reprinted with permission from ref 250. Copyright 2014 American Chemical Society.

interactions play a major role. The Coulomb energy gain (Figure 20a,b) was identified to lower the overall formation energy (i.e., lower the strain energy) favoring certain stable ordered structures (Figure 20c). The authors gave a comprehensive example of a rigid ionic I−Pb−I trimer model (Figure 20b), where Pb and I have nominal 2+ and 1− oxidation states, respectively. In this case, Pb has Coulomb attraction with two I ions and two I ions have Coulomb repulsion between them, which equilibrates the entire system. Now, when one ion is replaced by a Cl ion, there will be electron transfer between I and Cl because the two ions have different electronegativities. Cl will be $(1 + \delta)^-$ charged and I will be $(1 - \delta)^-$ charged. As consequence, the total Coulomb energy (before and after) will be lowered by $\delta^2/(2r)^2$ (Figure 20b). The schematic shapes of Coulomb energy gain are shown in Figure 20a. The alloy system has the largest Coulomb energy gain at $x = 1/3$. As described at the beginning of section 3.5, experimental reports by Sutton et al.[98] and Beal et al.[257] seem to confirm this prediction, where $CsPbI_2Br$ was demonstrated to show enhanced thermal and air stability. Yin et al.[250] calculated the miscibility gap temperature (T_{MG}), which is defined as critical temperature that alloys can be fully mixed based on special-quasirandom-structures (Figure 20d). TMGs of 625, 223, and 116 K were extracted for $CsPbI_{3-x}Cl_x$, $CsPbI_{3-x}Br_x$, and $CsPbBr_{3-x}Cl_x$, respectively. These indicate that mixed-(Br/I) and (Br/Cl) are easily formed, whereas mixed-(Cl/I) perovskites are difficult to be formed.

4. SIMULTANEOUS MIXED A-CATIONS AND MIXED X-HALIDE ANIONS

In the following sections, we continue to describe the more complex mixed-perovskite systems where the double (MA/

DOI: 10.1021/acsami.7b06001
ACS Appl. Mater. Interfaces XXXX, XXX, XXX−XXX

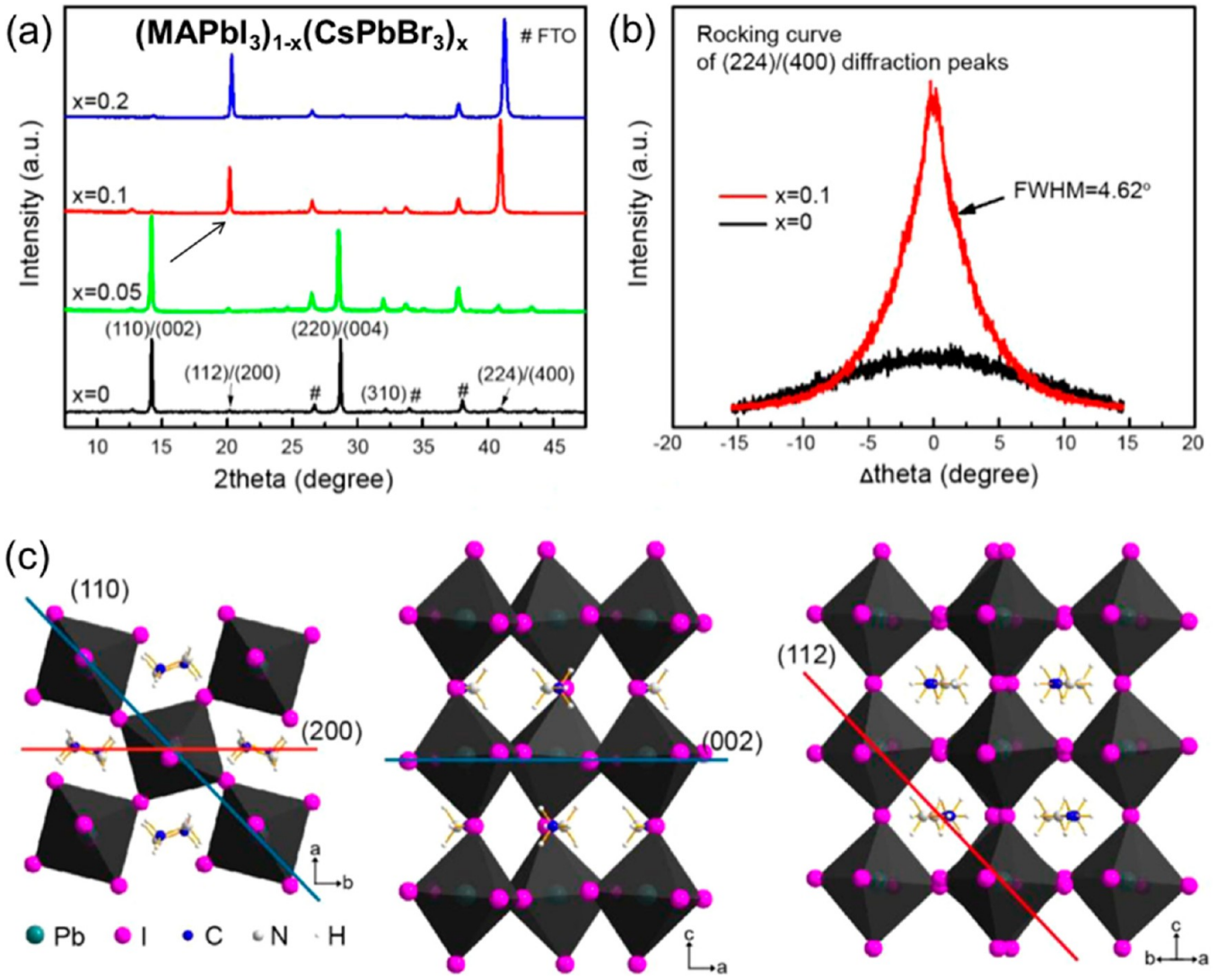

Figure 21. (a) XRD patterns of $(MAPbI_3)_{1-x}(CsPbBr_3)_x$ with x ranging from 0 to 0.2. (b) Rocking curve measurement of (224)/(400) diffraction peaks for x = 0 and 0.1. (c) Schematic illustrations of (110), (002), (112), and (200) perovskite crystal planes. Reprinted with permission from ref 123. Copyright 2016 Elsevier Ltd.

FA),[63,64,90,125−129,136,259] (Cs/MA),[123] (Cs/FA),[117,132−134,260,261] triple (Cs/FA/MA),[65,135,262] and even quadrupole (Rb/Cs/FA/MA) mixed cations[7,137] are generally followed by the mixed (I/Br), e.g., (Rb/Cs/FA/MA)Pb(I/Br). These newly developed material systems were reported to show even higher stability[137] and efficiencies as shown in the plot of certified efficiencies (Figure 1b).

4.1. (MA/Cs)Pb(I/Br) System. Niu et al.[123] reported for the first time on the synthesis of $(MAPbI_3)_{1-x}(CsPbBr_3)_x$ by a one-step method dissolving MAI, PbI_2, CsBr, $PbBr_2$ precursors in a mixed solvent of γ-butyrolactone:DMSO = 7:3 vol %. The fabricated solar cells exhibited an optimal performance at x = 0.1 with an average PCE of 15.9 ± 0.52% (Table 1). The best cell showed J_{sc} = 22.8 mA/cm^2, V_{oc} = 1.05 V, FF = 73%, and PCE = 17.6%. The stabilized power output (power output measurement over time until a steady value is reached) of the champion cell exhibited a PCE of 15.7% and photocurrent of 19.6 mA/cm^2, which means hysteresis is present. Accelerated stability of $(MAPbI_3)_{1-x}(CsPbBr_3)_x$-based solar cells was evaluated under UV irradiation (365 nm, 364 mW/cm^2) without encapsulation. It was mentioned that as x increased, the stability was significantly increased. For $(MAPbI_3)_{0.9}(CsPbBr_3)_{0.1}$, 75% of the initial performance was maintained after a total of 150 min irradiation. The same authors performed shelf life stability tests of unencapsulated $(MAPbI_3)_{0.9}(CsPbBr_3)_{0.1}$ devices in ambient air (dark, 25 °C, 20−30% RH) and observed that nearly 80% of the initial performance was maintained after 500 h.

The same work by Niu et al.[123] touches upon an interesting topic whether the photovoltaic efficiency is dependent on the facet-orientation in single grains of perovskites. This topic was discussed previously by Leblebici et al.[263] Generally, $MAPbI_3$ and $MAPbI_{3-x}Cl_x$ systems exhibit preferred orientation along ⟨110⟩ and/or ⟨002⟩ directions (see XRD pattern corresponding to x = 0 in Figure 21a). Interestingly, the (112) and (200) facets increased in intensity substantially with $(CsPbBr_3)_x$ (x = 0.1 and 0.2) concentration (Figure 21a). The orientation of the film can be further verified by rocking curve measurements (Figure 21b), which provides information on the existence of preferential growth axis and its spread on the azimuthal angle. For x = 0.1, (224)/(400) planes were parallel to the substrate with an angular spread of ±4.6°; meanwhile, for x = 0, no peaks

DOI: 10.1021/acsami.7b06001
ACS Appl. Mater. Interfaces XXXX, XXX, XXX−XXX

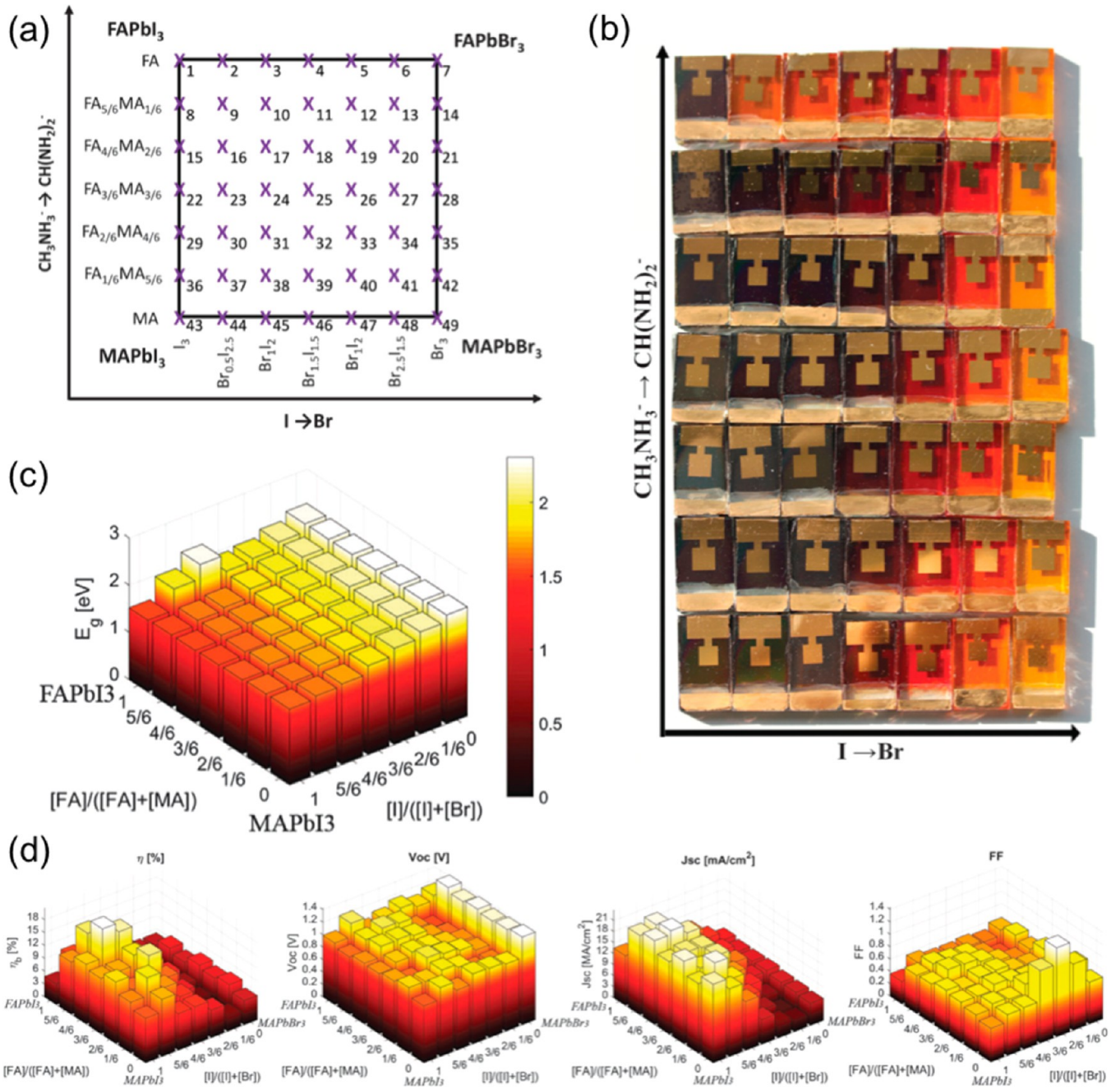

Figure 22. (a) Schematic illustration of the compositional matrix and (b) photo of fabricated cells of (FA/MA)Pb(I/Br) system. A total of 49 compositions were mapped. (c) Bar plot of the band gaps in the compositional space explored. (d) Solar cell device parameters for (FA/MA)Pb(I/Br)-based perovskite with different compositions. Reprinted with permission from ref 90. Copyright 2016 The Royal Society of Chemistry.

were observed. When x is increased to 0.3 and above, new peaks assigned to $CsPb_2Br_5$ were observed in XRD, which indicates x = 0.2 is a threshold limit for the full-miscibility in $(MAPbI_3)_{1-x}(CsPbBr_3)_x$. The origin for this preferential orientational growth was further examined employing XPS depth profile and DFT. Results from these measurements showed a heavily Cs-incorporated perovskite preferentially forms at the bottom layer. Based on DFT calculations of the $CsPbBr_3$ structure, it was shown that (100) (γ = 0.299 J/m^2) and (112) (γ = 0.314 J/m^2) planes showed a lower surface energy than the (110) (γ = 0.437 J/m^2) and (001) (γ = 0.526 J/m^2) planes. Therefore, it was concluded that the heavily Cs-incorporated perovskite at the bottom of the film could initiate the film growth along the ⟨112⟩/⟨200⟩ directions under thermodynamic control (Figure 21c).

4.2. (FA/MA)Pb(I/Br) System. After the initial works by Jeon et al.[63] and Yang et al.,[64] the simultaneous FA/MA-cation mixed and I/Br-halide mixed perovskites are one of the most studied ternary mixed perovskite system for photovoltaic applications (Table 1).[7,90,124−130,259,262,264−266] Out of six, three certified efficiencies reported by NREL is based on this perovskite system (Figure 1b). Jacobsson et al.[90] provided the entire compositional space of MA-FA−Br-I experimentally (Figure 22). In this study, a total of 49 precursor solutions with varying concentrations of PbI_2, $PbBr_2$, MAI, MABr, FAI, and FABr were used for perovskite synthesis (Figure 22a). The

DOI: 10.1021/acsami.7b06001
ACS Appl. Mater. Interfaces XXXX, XXX, XXX−XXX

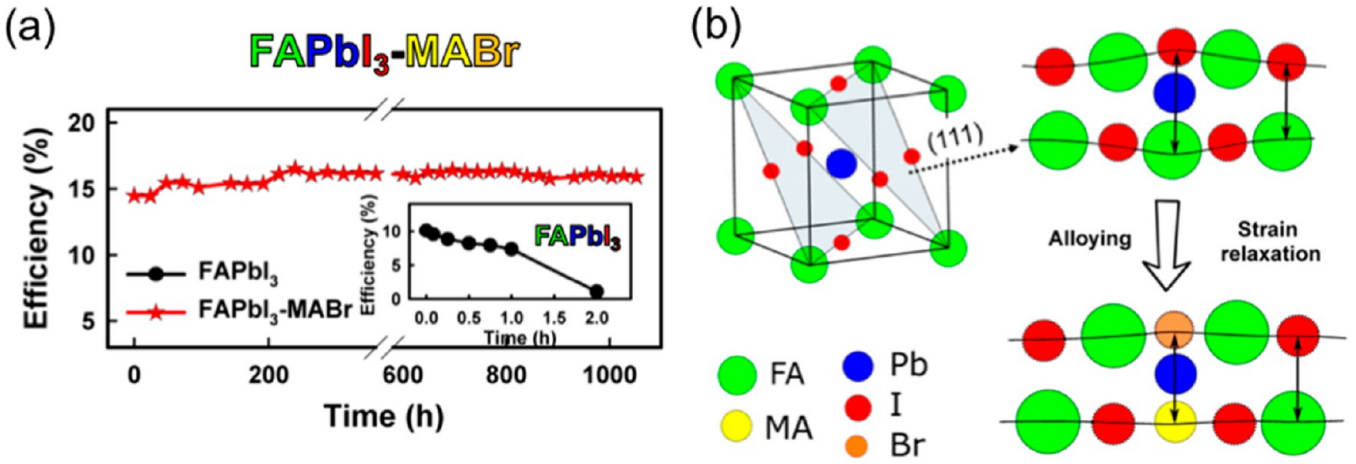

Figure 23. (a) Comparative PCEs of $FAPbI_3$-MABr- and $FAPbI_3$-based perovskite solar cells tested under storage conditions in air (~50% RH, 23 °C) without encapsulation. (b) Schematic illustration of strain relaxation when MABr is alloyed with $FAPbI_3$. Reprinted with permission from ref 125. Copyright 2016 American Chemical Society.

films were systematically characterized by UV−vis, PL, XRD techniques. Differences in cation and halide compositions lead to large variation in the optical appearance of deposited films (Figure 22b,c). The distribution of extracted bandgaps in the compositional matrix (Figure 22c) was fitted with an empirical relation to provide a numerical description of the dependence of band gap with respect to MA/FA and Br/I compositions (eq 4).

$$E_g(x, y) = 1.58 + 0.436x - 0.058y + 0.294x^2 + 0.0199x \cdot y \quad (4)$$

$$x = \frac{[Br]}{[Br] + [I]} \text{ and } y = \frac{[FA]}{[FA] + [MA]}$$

Similar to the description in section 3.2, PL measurements revealed also the appearance of more than one peak for films with 50% bromide or more, excluding the pure bromide perovskites. The authors proposed two explanations, (i) perovskites with a high bromide concentration increase the density of trap states within the band gap that can act as recombination centers and (ii) phase separation with the formation of an iodine-rich domains leads to the peak at lower photon energies in PL (section 3.2). XRD measurements provide valuable experimental observations: (i) iodine-rich pure FA-samples (numbers 2 and 3 in Figure 22a,b) deviate from others and the dominant phase is not the photoactive perovskites; (ii) Disregarding these two compositions and the $FAPbI_3$ composition (due to yellow phase; number 1 in Figure 22a,b), all other intended perovskites were formed and were the dominant phases; (iii) for compositions 1 to 38 (FA-rich devices), the experimental XRD data are in line with a cubic structure; (iv) it has been proposed that the transition border between room temperature tetragonal and cubic structures is found around $FA_{1/6}MA_{5/6}PbBr_1I_2$ (number 38). Full solar cell devices made with all 49 different compositions showed a widespread with efficiencies varying from 2.3% to 20.67% (Figure 22d). $FA_{4/6}MA_{2/6}Pb(Br_{1/6}I_{5/6})_3$ (number 16) yielded the best devices with a top efficiency of 20.67% (J_{sc} = 23.7 mA/cm^2, V_{oc} = 1.14 V, FF = 76%, Table 1). This is in agreement with other reports reporting high efficiencies around this composition.[63,130] Hysteresis was also observed to vary as mapping the compositional space. Interestingly, a trend can be observed that hysteresis is small for devices with a high fraction of both iodide and FA, and is higher for bromide- and MA-rich devices.[90] Ion migration on time scales from 10^{-1} to 10^2 s was previously reported to explain hysteresis.[7,259] Several reports showed that regardless of solar cell architectures and composition in perovskites, halide defects migrate and can reversibly accumulate at the interfaces of selective contacts. Furthermore, among several types of defects, iodide or bromide vacancy generation has been calculated to show the lowest formation energies (e.g., defects formed during sample preparation, under bias, etc.), with further bromide vacancies being favored over iodide.[7,259] Tress et al.[266] reported that inverted hysteresis (forward bias scan generates higher PCE than backward scan) is particularly pronounced in (FA/MA)Pb(I/Br) systems. Zheng et al.[125] fabricated $MAPbBr_3$-alloyed $FAPbI_3$ perovskites and solar cells based on these materials showed enhanced shelf life stability of more than 1000 h under ambient air (~50% RH, 23 °C) without encapsulation (Figure 23a). Based on XRD, the authors proposed a model that α-$FAPbI_3$ has an anisotropic strained lattice; higher strain in the (111) plane. In contrast, δ-$FAPbI_3$ is almost strain free explaining the favored $\alpha \rightarrow \delta$ phase transition at room temperature (section 2.1). They proposed that the strain in the (111) plane of α-phase is the driving force for the phase transition to the δ-phase (Figure 23b). When MABr is incorporated to alloy with $FAPbI_3$, the lattice size is reduced and strain within the grain is relaxed. In this way, the pseudocubic α-phase is stabilized at room temperature and even under humid air. In a recent report, Domanski et al.[259] investigated the impacts of cation defects formation and migration in the $(FAPbI_3)_{1-x}(MAPbBr_3)_x$ perovskite on its corresponding solar cell performance and long-term stability under operation conditions. Maximum power output was monitored for three identically prepared devices (A, B, C in Figure 24a). Devices A and B were continuously tracked over 100 h. These two devices exhibit very different profiles from that of device A showing high instability than that of device B. Because long-term stability is reflected from a convolution of several mechanisms (physicochemical and electrical) taking place within the perovskite solar cell, it is not surprising that identically prepared devices age differently. However, the authors identified that the initial decay in performance

DOI: 10.1021/acsami.7b06001
ACS Appl. Mater. Interfaces XXXX, XXX, XXX−XXX

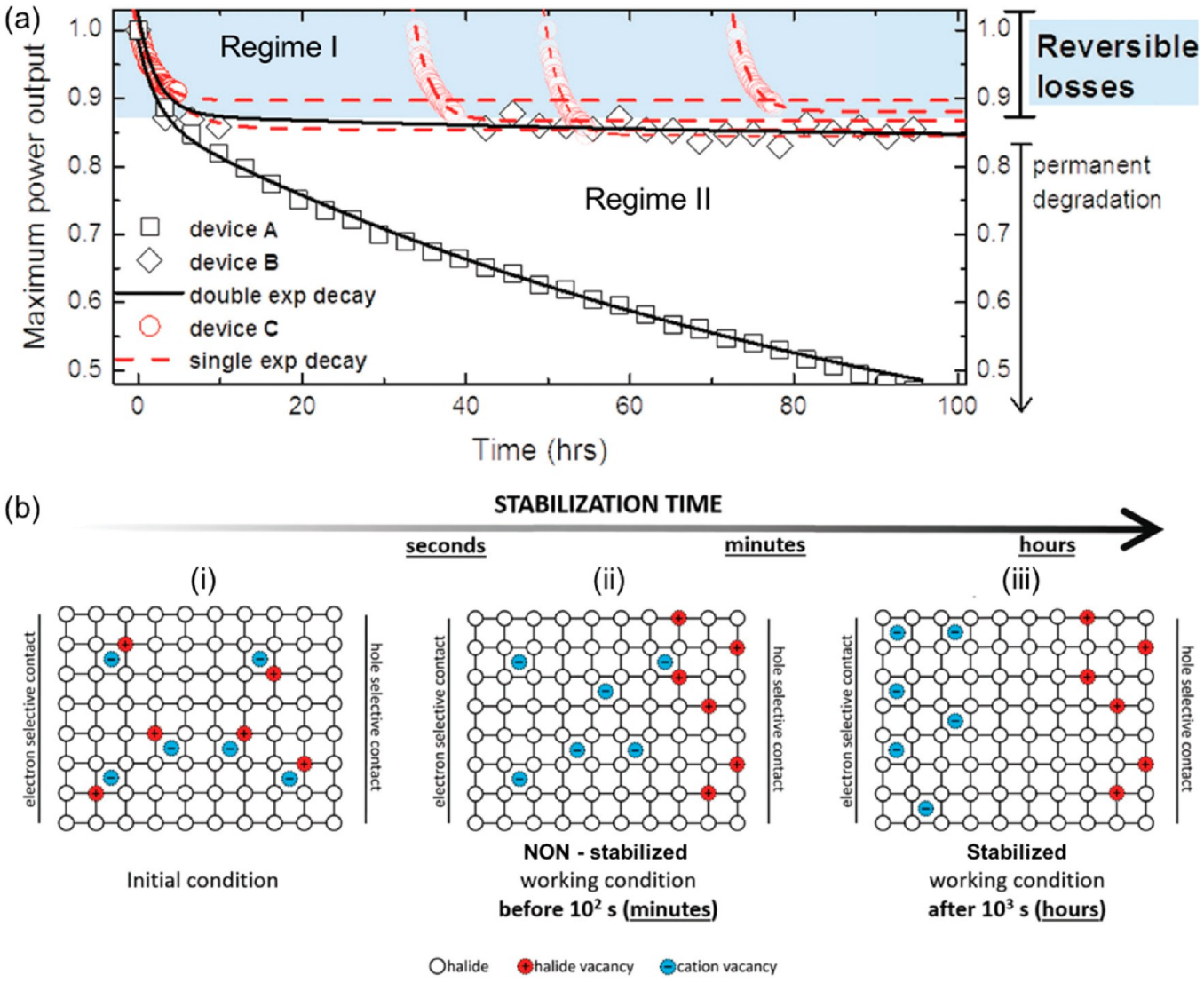

Figure 24. (a) Normalized maximum power output ($V \sim 0.85$ V) tested in N_2 environment for 3 identically prepared perovskite solar cells (devices A, B, C) measured under 1 sun. Devices A and B were continuously tracked for over 100 h. Device C was cyclically tracked 4 times for 5 h and it was left in dark at open circuit between consecutive measurements. (b) Schematic illustration showing the evolution of the ion distribution within the perovskite layer sandwiched between electron and hole selective contacts under working conditions on time scales from seconds to hours (i–iii). Reprinted with permission from ref 259. Copyright 2017 The Royal Society of Chemistry.

designated as regime I (Figure 24a) was unchanged. To isolate regime I from the subsequent degradation (regime II), the maximum power point for device C was stopped after only 5 h and repeated cyclically after resting the devices in dark for a different number of hours. Interestingly, the initial power output at each cycle was similar to the previous cycle, demonstrating that the initial performance losses are fully reversible (regime I) and can be separated from the subsequent permanent degradation (regime II). Degradation related to regime II (HTL, perovskite, top Au electrode related issues) was previously reported.[65,267,268] Followed by a subsequent series of experiments, the authors concluded that migration of cation vacancies form an additional Debye layer at the interface with the electron selective contact, which inhibits charge extraction (Figure 24b). However, when the device is given several hours of rest in dark, the ionic distribution equilibrates to the initial state, which leads to recovery of the initial performance (Regime I, Figure 24b). Migration of cation vacancies was shown to exhibit significantly longer time scales ($>10^3$ s) than the halide vacancy migration (between 10^{-1} and 10^2 s, Figure 24b).

4.3. (FA/MA)Pb(I/Cl) System. Mixed MA/FA cations and I/Cl halides perovskites with a chemical composition of $MA_{1-x}FA_xPb(I_{1-y}Cl_y)_3$ were first synthesized by Isikgor et al.[131] These perovskite films were prepared by dissolving PbI_2 + $PbCl_2$ and MAI + FAI precursors in a cosolvent of GBL/DMSO (3:7 vol. ratio) and low postannealing temperature of 80–110 °C to avoid chlorine species sublimate and/or decompose in the form of MACl (described in section 3.1). A planar heterojunction perovskite solar cell based on an inverted structure with ITO/PEDOT:PSS/$MA_{0.80}FA_{0.20}PbI_{3-y}Cl_y$/PC61BM/C60/LiF/Ag generated average $J_{sc} = 21.55 \pm 0.55$ mA/cm^2, $V_{oc} = 1.10 \pm 0.01$ V, FF = 75 ± 2%, and PCE = 17.45% (Table 1). This performance employing $MA_{0.80}FA_{0.20}PbI_{3-y}Cl_y$ ($E_g = 1.58$ eV) outperformed the control perovskite solar cells ($MAPbI_3$, $MAPbI_{3-y}Cl_y$, $MAPbI_{3-y}Br_y$, and $MA_{1-x}FA_xPbI_3$). The high photovoltaic performance was attributed mainly to (i) the long charge diffusion length

DOI: 10.1021/acsami.7b06001
ACS Appl. Mater. Interfaces XXXX, XXX, XXX–XXX

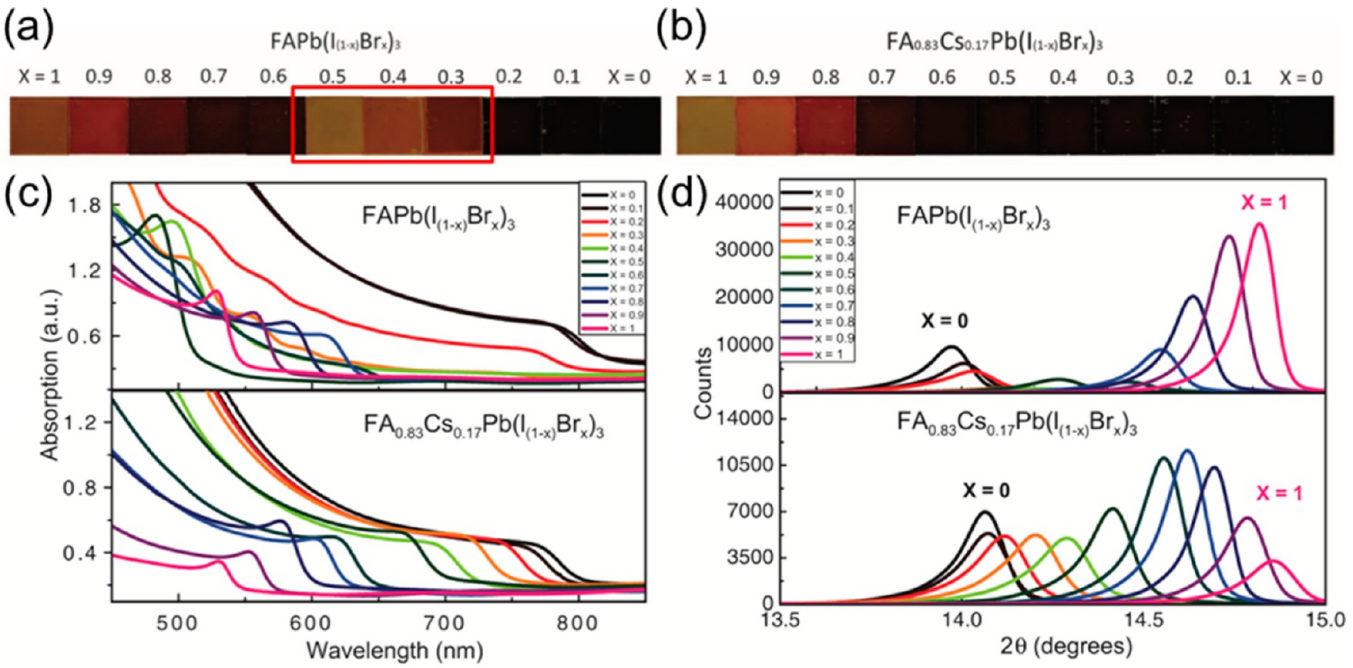

Figure 25. Photographs of (a) $FAPb(I_{1-x}Br_x)_3$ and (b) $FA_{0.83}Cs_{0.17}Pb(I_{1-x}Br_x)_3$ perovskite films with Br composition increasing from $x = 0$ to 1. (c) UV−vis absorbance spectra and (d) XRD patterns of $FAPb(I_{1-x}Br_x)_3$ and $FA_{0.83}Cs_{0.17}Pb(I_{1-x}Br_x)_3$ perovskites. Reprinted with permission from ref 132. Copyright 2016 American Association for the Advancement of Science (AAAS).

induced by mixed organic cations and mixed halides and (ii) suppression of the formation of undesirable yellow δ-phase of $FAPbI_3$ (E_g = 2.8 eV).

4.4. (FA/Cs)Pb(I/Br) System. With the aim to fabricate perovskite/silicon tandem solar cells, a number of reports synthesized mixed-cations and mixed-halides (i) to achieve high stability and (ii) to tune the band gap to an optimal value of ∼1.75 eV in order to current-match the top perovskite cell and bottom Si cell (E_g = 1.1 eV).[132,133,269] Based on the observations reported previously for binary mixed perovskites, (i) MAPb(I/Br) (section 3.2) is thermally unstable and suffers from halide segregation; (ii) FAPb(I/Br) shows better stability regarding halide segregation (section 3.2) and Br concentration helps tune the band gap to a desired value (∼1.75 eV); (iii) $FAPb(I_{1-x}Br_x)_3$ with $0.3 < x < 0.6$, an amorphous unstable phase is formed caused by a transition from a trigonal ($x < 0.3$) and cubic ($x > 0.5$) (Figure 25a); therefore, this composition range should be avoided (section 3.2); (iv) mixing small quantities of Cs with FA substantially enhances the stability of $Cs_xFA_{1-x}PbI_3$ suppressing halide segregation (section 2.3); (iv) the $\delta \rightarrow \alpha$ phase transformation in $FAPbI_3$ can be lowered down to room temperature when Cs/FA ratio of 45 at. % is incorporated in the $Cs_xFA_{1-x}PbI_3$ (section 2.3), McMeekin et al.[132] proposed the first $FA_yCs_{1-y}Pb(I_{1-x}Br_x)_3$ system based on FAI, CsI, $PbBr_2$, and PbI_2 precursors dissolved in DMF followed by addition of HI and HBr. Initially, they hypothesized that if FA is partially substituted by Cs, the structural instability in Br-to-I phase space could be shifted to higher energies, and thus achieve a structurally stable mixed halide perovskite with a band gap of 1.75 eV. Their trial with $FA_{0.83}Cs_{0.17}Pb(I_{1-x}Br_x)_3$ showed unexpected results that the region of structural instability was not observed (Figure 25b). Instead, a continuous series of dark films throughout the entire composition range ($0 \leq x \leq 1$) was observed and corroborated by UV−vis (Figure 25c) and XRD (Figure 25d) measurements. Over the entire of Br-to-I range, $FA_{0.83}Cs_{0.17}Pb(I_{0.6}Br_{0.4})_3$ composition was chosen based on the Vergard's law (section 3.2) leading to the band gap of 1.74 eV. These perovskites showed further improved structural stability and resistance to halide segregation when compared to $MAPb(I_{0.6}Br_{0.4})_3$ (section 3.2). Furthermore, under thermal stress conditions at 130 °C, $FA_{0.83}Cs_{0.17}Pb(I_{1-x}Br_x)_3$ showed superior stability compared to $MAPb(I_{0.6}Br_{0.4})_3$.[132] Planar heterojunction perovskite solar cell based on an inverted structure with FTO/SnO_2/PC60BM/$FA_{0.83}Cs_{0.17}Pb(I_{0.6}Br_{0.4})_3$/spiro-MeOTAD/Ag generated J_{sc} = 19.4 mA/cm^2, V_{oc} = 1.2 V, FF = 75.1%, and PCE = 17.1% (Table 1). When combined with a 19% PCE c-Si, the feasibility of achieving >25% PC four-terminal tandem cells were demonstrated.[132] Employing the same $FA_{0.83}Cs_{0.17}Pb(I_{0.6}Br_{0.4})_3$ perovskite, Busch et al.[133] demonstrated a two-terminal 1 cm^2 active area perovskite/tandem solar cell with J_{sc} = 18.1 mA/cm^2, V_{oc} = 1.65 V, FF = 79%, and PCE = 23.6%. More recently, Zhang et al.[269] performed DFT calculations determining three sets of x and y for $FA_yCs_{1-y}Pb(I_{1-x}Br_x)_3$ systems, which have band gap around 1.75 eV. In addition, their refractive indices and extinction coefficients were also calculated. They found that $FA_{0.89}Cs_{0.11}Pb(I_{0.56}Br_{0.44})_3$/c-Si tandem solar cells achieved the highest PCE among the three sets. The concept of perovskite-perovskite tandem cell employing $FA_{0.75}Cs_{0.25}Sn_{0.5}Pb_{0.5}I_3/FA_{0.83}Cs_{0.17}Pb(I_{0.6}Br_{0.4})_3$ with band gaps of 1.2 and 1.74 eV, respectively, was demonstrated to generate PCE as high as 20.3% in a four-terminal configuration.

Perovskite single-junction solar cells with regular structure (TiO_2 electron transport layer (ETL) and spiro-MeOTAD HTL) based on similar $FA_{0.8}Cs_{0.2}PbI_{2.84}Br_{0.16}$ composition, generated J_{sc} = 23.3 mA/cm^2, V_{oc} = 1.072 V, FF = 72.3%, and PCE = 18.02%. A wider parameter space of the influences of mixed-cation and mixed-halide perovskites in $Cs_yFA_{1-y}Pb(I_{1-x}Br_x)_3$ was studied by Rehman et al.[261] They showed that a region for Cs concentration between $0.10 < y < 0.30$ leads to high crystalline quality, long charge-carrier lifetimes, and high charge-carrier mobilities. Within the $Cs_yFA_{1-y}Pb(I_{0.4}Br_{0.6})_3$

DOI: 10.1021/acsami.7b06001
ACS Appl. Mater. Interfaces XXXX, XXX, XXX−XXX

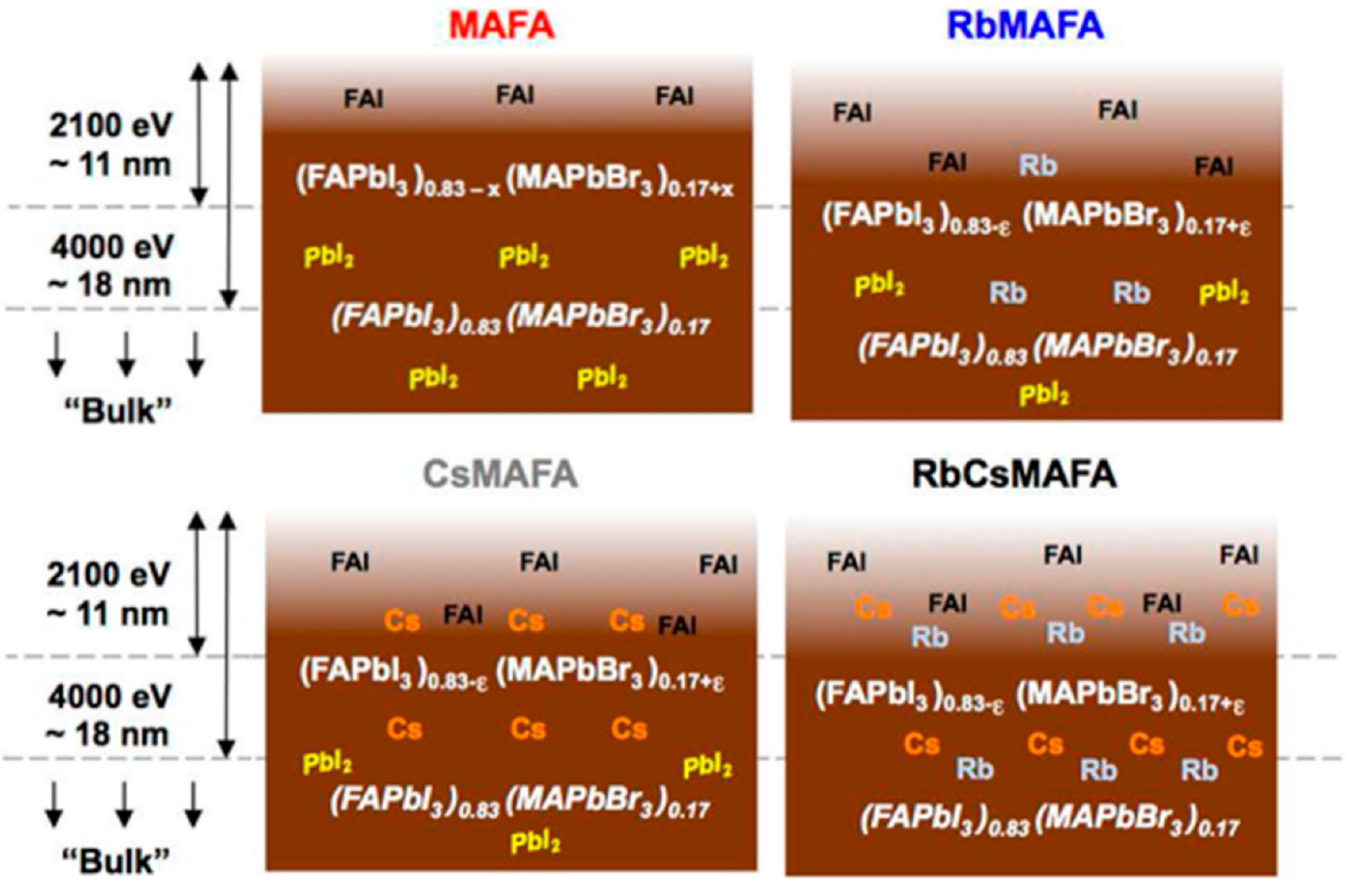

Figure 26. Schematic illustration of a depth-dependent chemical composition in MAFA = $(MA_{0.17}FA_{0.83})Pb(I_{0.83}Br_{0.17})_3$, 0.1[0.83$PbI_2$, 0.17$PbBr_2$]; RbMAFA = 0.05RbRbI[$(MA_{0.17}FA_{0.83})Pb(I_{0.83}Br_{0.17})_3$, 0.1[0.83$PbI_2$, 0.17$PbBr_2$]]$_{0.95}$; CsMAFA = 0.05CsI[$(MA_{0.17}FA_{0.83})Pb(I_{0.83}Br_{0.17})_3$, 0.1-[0.83$PbI_2$, 0.17$PbBr_2$]]$_{0.95}$; RbCsMAFA = 0.05RbI[0.05CsI[$(MA_{0.17}FA_{0.83})Pb(I_{0.83}Br_{0.17})_3$, 0.1[0.83$PbI_2$, 0.17$PbBr_2$] $_{0.95}$]$_{0.95}$. The chemical formula are based on the precursor solution composition. A nonstoichiometric solution was used in excess of 10 mol % lead precursors leading to the nominal composition of MAFA stated above. Reprinted with permission from ref 270. Copyright 2017 American Chemical Society.

series, y = 0.2 showed the concentration leading the perovskite film exhibiting high charge-carrier mobilities of ~18 $cm^2 \cdot V^{-1} \cdot s^{-1}$ and charge-carrier lifetimes of ~80 ns. They demonstrated a correlation between high crystallinity and suppressed photo-induced halide segregation, i.e., short-range crystalline order or the presence of grain boundaries enables halide segregation by releasing lattice strain energy leading to iodide-rich and bromide-rich domains (section 3.2). Next, the halide-parameter space was investigated for $Cs_{0.17}FA_{0.83}Pb(I_{1-x}Br_x)_3$. They showed that once the perovskite contains enough fraction of Cs for the stability, high charge-carrier mobilities and diffusion lengths are obtained across the full I:Br range. Furthermore, the band gap varies linearly with the Vegard's law (section 3.2) across the full I:Br range.[261] Nonencapsulated $Cs_{0.17}FA_{0.83}Pb(I_{0.6}Br_{0.4})$-based perovskite solar cells employing *n*-doped C60 as electron extraction layer in a planar heterojunction architecture, showed a 30-fold enhanced air stability compared to $MAPbI_{3-x}Cl_x$-based devices under full spectrum solar illumination without encapsulation (t_{80} ~ 600 h); and t_{80} > 3420 h when sealed.[134]

4.5. (Cs/FA/MA)Pb(I/Br) System. Based on previous successful reports of Cs incorporation in $(MA/Cs)PbI_3$ and $(FA/Cs)PbI_3$ systems (sections 2.2 and 2.3), Saliba et al.[65] (a follow up work from the same group was reported by Matsui et al.[135]) reported on the first triple cation mixed (Cs/FA/MA)Pb(I/Br) system generating stabilized power output of 21.1% that also holds a position in the certified NREL chart (Figure 1b). The stability of these devices was tested in a nitrogen atmosphere held at room temperature under constant illumination and maximum power tracking for 250 h. The device efficiencies of triple cation perovskites with FTO/c-TiO_2/mp-TiO_2/$Cs_{0.05}(FA_{0.83}MA_{0.17})_{0.95}Pb(I_{0.83}Br_{0.17})_3$/spiro-MeOTAD/Au structure decayed from ~20% to ~18% within a few hours (Regime I,[259] section 4.2) and then stayed stable for at least 250 h.

4.6. (Rb/FA/MA)Pb(I/Br) System. Duong et al.[136] and Zhang et al.[122] studied the incorporation of Rb in high performing $(FAPbI_3)_{1-x}(MAPbBr_3)_x$ mixed perovskites. The motivation for studying this system was that inclusion of a smaller cation of Cs in $(FAPbI_3)_{1-x}(MAPbBr_3)_x$ lead to enhanced stability (section 4.5). Therefore, the incorporation of an even smaller cation would be interesting to be tested. The addition of 5% RbI in combination with excess PbI_2 was observed to eliminate the formation of yellow nonperovskite phase and enhance the crystallinity of the films. However, inclusion of more than 10% RbI resulted in the formation of a Rb-rich phase, which was detrimental for the cell performance.[136] A side-by-side comparison of solar cell devices based on $Rb_{0.05}FA_{0.80}MA_{0.15}PbI_{2.55}Br_{0.45}$ and $Cs_{0.05}FA_{0.80}MA_{0.15}PbI_{2.55}Br_{0.45}$ showed very similar performances (PCE ~ 19.5%, Table 1).

4.7. (Rb/Cs/FA)Pb(I/Br) System. Syzgantseva et al.[157] reported theoretical calculations on the stabilization of $FAPbI_3$ by Cs/Rb incorporations. Enhanced stabilization of mixed

DOI: 10.1021/acsami.7b06001
ACS Appl. Mater. Interfaces XXXX, XXX, XXX−XXX

perovskites was demonstrated when Cs^+ and Rb^+ are employed instead of MA^+. In addition, the increased phase stability of Cs^+ and Rb^+ incorporated systems comes with only a slight increase in the band gap. Saliba et al.[137] fabricated systematically $Rb_{0.05}Cs_{0.05}FA_{0.90}Pb(I_{0.83}Br_{0.17})_3$-, $Rb_{0.05}Cs_{0.10}FA_{0.85}Pb(I_{0.83}Br_{0.17})_3$-, and $Rb_{0.10}Cs_{0.05}FA_{0.85}Pb(I_{0.83}Br_{0.17})_3$-based solar cells showing efficiencies as high as 18.3%, 19.3%, and 18.7%, respectively (Table 1).

4.8. (Rb/Cs/FA/MA)Pb(I/Br) System. Based on their past experience with binary and triply mixed cations (RbFA, RbCsFA, RbMAFA), Saliba et al.[137] were able to synthesize the first perovskite containing four simultaneous cations (RbCsFAMA). The concentration of Rb was limited to 5 at. % as they were aware that a higher concentration of Rb will lead to the formation of a Rb-rich phase, which is detrimental for the performance (section 2.4). Devices with the architecture of $FTO/c\text{-}TiO_2/mp\text{-}TiO_2/Rb_{0.05}Cs_{0.05}(FA_{0.83}MA_{0.17})_{0.90}Pb(I_{0.83}Br_{0.17})_3$/PTAA/Au generated stabilized efficiencies of up to 21.6% (averaged PCE was 20.2%, Table 1). Furthermore, PTAA was employed as hole transport layer (HTL) and these cells maintained ∼95% of their initial performance when tested in N_2 atmosphere, but at elevated temperature of 85 °C for 500 h and under operation conditions (full illumination and tracking the maximum power point). Similar high stability was also confirmed by Duong et al.[138] fabricating $FTO/c\text{-}TiO_2/mp\text{-}TiO_2/Rb(5\%)$ doped $FA_{0.75}(MA_{0.6}Cs_{0.4})_{0.25}PbI_2Br$/PTAA/Au, which generated stabilized power output of ∼17.4% (Table 1). The long-term high stability under illumination indicates that phase segregation in iodide- and bromide-rich domains phenomena (section 3.2) is significantly suppressed upon this cation engineering strategy.[137,138] The charge transport within the RbCsMAFA perovskite layer is substantially faster than in CsMAFA, which is already much faster than in MAFA leading to the conclusion that Rb incorporation leads to defect-free perovskites.[132]

Although these studies seem to infer a uniform solid solution, there is no clear evidence supporting that these cations are incorporated into the perovskite crystal structure forming a uniform solid solution. Recently, Philippe et al.[270] reported a depth-dependent chemical composition in (Rb/Cs/FA/MA)-Pb(I/Br) perovskite films employing hard X-ray photoelectron spectroscopy (HAXPES, synchrotron radiation source). These results were compared systematically with perovskite materials with two (MA/FA) and three cations (CsMAFA and RbMAFA) to investigate the role of Cs and Rb cations. Two photon energies were employed, with the photon energy of 2100 eV to probe the surface of the sample (∼11 nm) and the photon energy of 4000 eV to probe deeper (∼18 nm; referred as bulk chemical composition). Quantifications were conducted for both photon energies and the I/Pb, Cs/Pb, and Rb/Pb ratios and its interpretation were summarized in Figure 26. For example, the Br/Pb and I/Br ration correspond to the proportion of FA and MA. In the case of MAFA sample that is generally prepared with excess of PbI_2, HAXPS (4000 eV) confirms that the excessive PbI_2 can be found in the bulk of the material. Upon addition of a third cation (Cs^+ or Rb^+), less PbI_2 remains in the material. When the probe depth decreases, an increase of Br over Pb was observed indicating a slight bromide enrichment within the surface as compared to bulk as illustrate with $(MAPbBr_3)_{0.17+\varepsilon}(FAPbI_3)_{0.83-\varepsilon}$. This slight $MAPbBr_3$ enrichment in the surface was assigned to the presence of unreacted FAI at the surface and PbI_2 in the bulk leading to deficiency in $FAPbI_3$. In the RbMAFA sample, only 2% and 1% were detected at 4000 and 2100 eV, respectively, suggesting that Rb was mainly located in the bulk, but observed to easily migrate to the surface due to its small ionic radius. For the CsMAFA sample, ∼ 6% detected Cs was found to distribute uniformly at both depths. Interestingly, the RbCsMAFA sample did not correspond to a simple superposition of RbMAFA and CsMAFA samples. Both Cs and Rb distributions were homogeneous over the ∼18 nm indicating that Rb^+ and Cs^+ alkali metals act jointly in a way that Cs helps the incorporation of Rb into the perovskite compound.[270] This is also in good agreement with recent theoretical calculations by Syzgantseva et al.[157] reporting that doping by a mixture of Cs and Rb has a synergetic effect on perovskite stabilization.

5. SUMMARY AND OUTLOOK

The exceptional performance of perovskites as light harvester materials for solar cells are ascribed to excellent material properties such as direct band gap, outstanding high absorption coefficient, abrupt optical band edge, large charge carrier diffusion length and low exciton binding energy. The earlier works focused on $MAPbI_3$ (E_g ∼ 1.5−1.61 eV, section 1), α-$FAPbI_3$ (E_g ∼ 1.47−1.55 eV, section 2.1), and α-$CsPbI_3$ (E_g ∼ 1.67−1.73 eV, section 2.3) with preference for $FAPbI_3$ because of its smaller band gap. The optimal E_g for a single-junction solar cell is between 1.1 and 1.4 eV according to the Shockley−Queisser limit[91] and therefore there is still plenty of room for improvement to achieve even higher efficiencies. So far, the highest PCE of pure $MAPbI_3$-based solar cell was reported to reach ∼18−20%.[139,140] As a comparison, the best PCE reported for pure $FAPbI_3$-based perovskite solar cell reached 13.5−18%,[64,99,142−144] which is somewhat lower than $MAPbI_3$ (see section 2.1 for more details). $CsPbI_3$-based perovskite solar cell exhibited limited PCEs of <2.9% (section 2.3).[115,155,156] Despite high efficiencies of $MAPbI_3$- and $FAPbI_3$-based solar cells, these simple hybrid perovskite materials fail to meet the required long-term stability under working conditions (e.g., when tracking the maximum power point (MPP) voltage under continuous light illumination), which is the main obstacle for this technology to reach commercialization.

The fundamental origins for the major PCE loss during solar cell operation includes (i) thermal, moisture, oxygen, bias, and light induced permanent degradation leading to PbI_2 and I-containing volatile species[28,29,37,92,93,271,272] and (ii) polymorphism of α,δ-$FAPbI_3$ in ambient conditions (section 2.1 and Figure 3b−d). At room temperature, $FAPbI_3$ preferentially crystallizes to the δ-$FAPbI_3$, which possess a high E_g (∼2.43 eV[151]) and is unsuitable for photovoltaic applications. The photoactive α-$FAPbI_3$ is stabilized only at higher temperatures of ∼125−165 °C (Figure 3d). Note that phase transition (e.g., tetragonal to cubic in $MAPbI_3$) or polymorphism (α- to δ-phase in $FAPbI_3$) is not a permanent degradation phenomenon as they can be recovered reversibly.

The most promising approaches to improve degradation and phase/polymorphism stability in perovskite solar cells are the introduction of the mixing of A (binary, tertiary, or even quaternary mixed position) site cations and X site halide anions (I, Br, and Cl anions) (Figure 1b and Table 1), i.e., chemical compositional engineering[63] or alloying.[8,101] In fact, A cation mixed perovskite systems of $(FA/MA)PbI_3$, $(MA/Cs)PbI_3$, $(FA/Cs)PbI_3$, $(FA/Rb)PbI_3$ (section 2) showed enhanced stability (Figure 8c and Figure 9) as compared to reference cells comprising simple perovskites ($MAPbI_3$ or $FAPbI_3$). At the current stage, it is difficult to pinpoint the binary composition

DOI: 10.1021/acsami.7b06001
ACS Appl. Mater. Interfaces XXXX, XXX, XXX−XXX

(mixed A cation) that leads to the most enhanced stability. This is because of the various synthesis methods of perovskite films adopted by the different groups that lead to different grain sizes, uneven coverage, pinhole formation, capping layer thickness, variations in stoichiometry (e.g., excessive lead halide or cation), nonuniform spatial distribution of mixed perovskites' constituents, and etc. Furthermore, variations in devices induced by processing imperfections make it difficult to properly identify intrinsic material and device properties when comparing among the individual and independent reports from the various groups (Table 1). In this sense, a universal deposition protocol[262] is desirable that allows side-by-side comparisons from a myriad of different chemical compositions to pinpoint the most promising chemical composition for photovoltaic applications. Fundamental microscopic origins of enhanced stability for $(FA/MA)PbI_3$[106] (section 2.1) as well as $t_{effective}$ (geometric Goldschmidt effective tolerance factor) for $(FA/Cs)PbI_3$[101] (section 2.3) and thermodynamic considerations for $(FA/Cs)PbI_3$[117] and $(FA/Cs/Rb)PbI_3$[157] (section 2.3) were proposed. For the $(FA/MA)PbI_3$, the incorporation of MA^+ cations that has a high dipole moment leads to stronger interactions with PbI_6 octahedra and stabilizes the α-$FAPbI_3$ without significant lattice shrinkage or changes in the optical properties (Figure 3e).[106] It has been generalized that perovskites with $t < 0.8$ and $t > 1$ tend to form the δ-phase orthorhombic structure (e.g., δ_O-$CsPbI_3$) and the δ-phase hexagonal structure (e.g., δ_H-$FAPbI_3$), respectively.[101] The cubic structure is only preferred for $0.8 < t < 1$ (Figure 7a). Alloying a high t $FAPbI_3$ and low t $CsPbI_3$, $t_{effective}$ can be tuned to be between 0.8 and 1.0 in $(FA/Cs)PbI_3$ perovskites, which favors a stable perovskite structure.[101] Based on theoretical calculations, thermodynamic arguments were used to explain the stability of $(FA/Cs)PbI_3$[117] and $(FA/Cs/Rb)PbI_3$[157] perovskite systems. Cs^+ and Rb^+ were predicted to be more efficient in stabilizing the $FAPbI_3$ perovskite than MA^+ based on the balance of internal energy variation (ΔE), mixing entropy contributions ($-\Delta S$), and free energy $\Delta F = \Delta E - \Delta S$ (Figure 10). In short, the incorporation of Cs^+ and/or Rb^+ thermodynamically favors the formation of new perovskite phases and brings the system into a new equilibrium state. Systems with mixed X anion halides with A site constrained to a single monovalent cation, MAPb(I/Cl), FAPb(I/Cl), MAPb(I/Br), FAPb(I/Br), MAPb(Br/Cl), MAPb(I/Br/Cl), CsPb(I/Br), CsPb(Br/Cl), CsPb(I/Cl) were reported to show peculiar phenomena (section 3). MAPb(I/Cl) is one of the most studied binary mixed perovskite because of the strong interest from the field trying to answer the question whether Cl can in fact be incorporated into the lattice of $MAPbI_3$ (section 3.1). It has been proposed that Cl incorporation in $FAPbI_3$ structure helps stabilize the α-$FAPbI_3$ phase; however, further in-depth studies are needed as the reported works are scarce (section 3.1). Synthesis of MAPb(I/Br) system in the full range of Br:I composition ratio was reported by various groups where E_g can be tuned effectively (section 3.2 and Figure 13). These E_g values are closely related to the lattice parameter of MAPb(I/Br), which was demonstrated to closely follow the Vergard's law (section 3.2). Only a small deviation from the Vegard's law was observed in the cubic regime (Figure 12) indicating presence of additional interactions in the mixed-halogens.[220,226] Under storage conditions in dark or low light intensity, MAPb(I/Br) with the Br content of ~20% provided enhanced stability even under relative humidity of 55%. This was closely correlated to the tetragonal to pseudocubic phase transformation (Figure 12b,d) arising from the incorporation of smaller ionic radius of Br and consequently leading to a more compact tightly bound structure (higher t factor). However, when the initially homogeneous MAPb(I/Br) is exposed to light, a phase-separation into two phases, one I-rich domain and the other Br-rich domain form in the same film (Figure 15).[234,237,240] A number of reports proposed the microscopic as well as macroscopic origins based on thermodynamics, energy levels (CBM and VBM), and light-induced generation of lattice strain leading phase-segregation phenomena (see section 3.2 and Figure 16). In comparison, the FAPb(I/Br) system was reported to be more resilient against phase segregation than MAPb(I/Br) system (section 3.2). The XRD analysis of FAPb(I/Br) system in the full range of Br:I composition ratio shows an interesting phenomenon that has an amorphous phase, which a fundamental understanding is still lacking (Figure 17). More interestingly, incorporation of small amounts of Cs was observed to suppress this amorphous phase (section 4.4). Based on the fact that halide perovskites have strong ionic character, Coulomb interactions were also proposed to play a major role (section 3.5 and Figure 20). The interplay of strain (favoring demixing) and Coulomb (favoring mixing) energies describes the formation energies of CsPb(X/Y) with X,Y = I, Br, Cl that as consequence dictates its stability (Figure 20).[250] Based on these fundamental concepts described in sections 1 and 2, the more complex systems of simultaneously mixed A and mixed X (MA/Cs)Pb(I/Br), (FA/MA)Pb(I/Br), (FA/MA)Pb(I/Cl), (FA/Cs)Pb(I/Br), (Cs/FA/MA)Pb(I/Br), (Rb/FA/MA)Pb(I/Br), (Rb/Cs/FA)Pb(I/Br), (Rb/Cs/FA/MA)Pb(I/Br) perovskites were described in section 4. Out of six, five certified efficiencies reported by NREL were based on the (FA/MA)Pb(I/Br) perovskite system (Figure 1b). Enhanced stability under storage conditions was reported for (FA/MA)Pb(I/Br) system (Figure 23a). It was proposed that when MABr is incorporated to alloy with $FAPbI_3$, the lattice size is reduced and the strain forces (demixing) within the grain are relaxed. In this way, the pseudocubic α-phase is stabilized at room temperature and even under humid air (Figure 23b). However, (FA/MA)Pb(I/Br)-based solar cells under operation conditions (tracking the maximum power point), migration of halide vacancies as well as cation vacancies were proposed to take place (Figure 24).[259] Cs incorporation in (FA/Cs)Pb(I/Br) system (section 4.4) was reported to suppress halide segregation (section 2.3) and formation of unstable amorphous phase (Figure 25a). Optimized compositions lead generally to higher E_g and therefore the (FA/Cs)Pb(I/Br) system was employed as the top cell in the tandem solar cell structure showing high promises (section 4.4).[132,133,269] Reports on ternary (Cs/FA/MA)[65,135,262] and quaternary (Rb/Cs/FA/MA) mixed cations[7,137] have just bought new hopes that a "magical" composition may lead to a stable perovskite with even higher PCE.[84] Thermodynamics must underlie this "magical" composition. The concept of effective tolerance factor (section 2.3) may help as a starting point for identifying thermodynamically stable hybrid mixed cations and mixed halides perovskites. Multicomponent perovskite design to achieve a stable single pure phase can enable a creation of stable structures with optimal transport and optical properties. However, a strict control over the phase composition of mixed perovskites should be ensured at the preparation stage, i.e., mixed perovskite materials should be clean from admixtures of nonperovskite phases (section 3.2).[120,157] Strategies to fabricate perovskite single-crystal-based solar cells were reported in the

DOI: 10.1021/acsami.7b06001
ACS Appl. Mater. Interfaces XXXX, XXX, XXX−XXX

literature[17,273−275] and naturally it is of high interest to study the optoelectronic properties (e.g., surface and bulk trap densities) of mixed halide perovskite single crystals, which has significantly different morphological (e.g., grain boundary), structural (e.g., perovskite crystal orientation), as well as spatial chemical composition distribution compared to polycrystalline thin-films of perovskites.[209,246,247]

Energy levels measurements (work function, CBM, and VBM) of mixed perovskites and its alignments with adjacent selective contact layers (ETL and HTL) are largely missing in the literature. To date, only a handful of publications provided insights into the energy diagrams, band bending, and interfacial dipole concepts studied on simpler $MAPbI_3$, $MAPbI_{3-x}Cl_x$, $MAPbBr_3$, $MAPbBr_{3-x}Cl_x$, $CsPbBr_3$ perovskite systems.[276−288] Within perovskite solar cell structures, each underneath substrate may have influence on the energy levels of the top layer under examination by ultraviolet spectroscopy (UPS).[282,289,290] Therefore, precise energy level alignments among stacked layers can only be obtained if UPS is performed on the individual top layers that are stacked on the actual prior layers following device structure. A few studies provided the energy-level alignments across all stacked functional layers within the perovskite solar cell, e.g., FTO/c-TiO_2 (+mp-TiO_2)/$MAPbI_3$ (or $MAPbI_{3-x}Cl_x$)/spiro-MeOTAD/Ag or Au, employing KPFM.[291−293] Further studies on the energy level alignments of mixed perovskites across all stacked layers are expected to bring insights into the correlation with perovskite solar cell parameters.[276−288]

Pb-free perovskites are still being investigated intensively.[294−306] Computational approaches based on the tolerance factor (t) are generally employed to predict the geometrical stability of three-dimensional (3D) ABX_3 perovskite structures.[15,160,307] Based on revised ionic radii, which considers greater covalency in metal-halide bonds, Travis et al.[160] found that only a handful of cations may be successfully placed on the B site of iodide-based perovskite: Sn, Yb, Dy, Tm, Sm, Ca, Sr. Filip and Giustino[308] and Körbel et al.[309] performed a systematic combinatorial search based on DFT over the entire periodic table. Starting from over 32 000 possible 3D ABX_3 compounds, Körbel et al. found 199 thermodynamically stable perovskites in the cubic structure.[309] Considering the E_g values suitable for photovoltaic applications among these 199 perovskites, all ABX_3 structures with single cation and single anion were based on Sn and Ge halide perovskites. The overall conclusion from these studies is that Pb plays a key role in the optoelectronic properties of 3D ABX_3 perovskites and is unique among all single divalent metals in the periodic table. Great efforts[306] have been made toward searching for low-dimensional perovskites with multivalent elements yielding a "3-2-9" (or $A_3B_2X_9$) 2D,[81,310−312] quasi-2D,[313−316] "3-1-5" single-chain, "4-1-6" single-octahedron structures, and "2-1-1-6" 3D double perovskite structures with compensated charges.[81,296,299,306,317] Quasi-2D perovskite solar cells were reported to show enhanced moisture stability; however, it is often associated with poor photovoltaic properties. In a recent work, Xiao et al.[306] compiled reported Pb-free halide perovskites and introduced the concept of electronic dimensionality. It was proposed that the higher photovoltaic performance is intimately associated with the isotropic 3D transport properties of photogenerated charges.[313,315,316] In this sense, it explains the lower PCE reported for lower-dimensional perovskites as absorbers.[306] The chemical composition engineering or alloying strategy has been scarcely explored for Pb-free perovskite systems, and further exploration for a "magical" composition is expected to bring subsequent years of key findings for the photovoltaic community stimulating further interests of both academia (fundamental research) and industry (new technology).

AUTHOR INFORMATION

Corresponding Author

*Y. B. Qi. E-mail: Yabing.Qi@OIST.jp.

ORCID

Yabing Qi: 0000-0002-4876-8049

Author Contributions

‡These authors contributed equally to this work.

Author Contributions

Y.B.Q. conceived the idea, initiated, and supervised the work. All authors contributed to writing the paper.

Notes

The authors declare no competing financial interest.

ACKNOWLEDGMENTS

This work was supported by funding from the Energy Materials and Surface Sciences Unit of the Okinawa Institute of Science and Technology Graduate University, the OIST Proof of Concept (POC) Program, the OIST R&D Cluster Research Program, and JSPS KAKENHI Grant Number 15K17925.

REFERENCES

(1) Web of Science, Thomson Reuters. https://webofknowledge.com/ (accessed March 21st, 2017).

(2) Kojima, A.; Teshima, K.; Shirai, Y.; Miyasaka, T. Organometal Halide Perovskites as Visible-Light Sensitizers for Photovoltaic Cells. *J. Am. Chem. Soc.* **2009**, *131*, 6050−6051.

(3) Kim, H. S.; Lee, C. R.; Im, J. H.; Lee, K. B.; Moehl, T.; Marchioro, A.; Moon, S. J.; Humphry-Baker, R.; Yum, J. H.; Moser, J. E.; et al. Lead Iodide Perovskite Sensitized All-Solid-State Submicron Thin Film Mesoscopic Solar Cell with Efficiency Exceeding 9%. *Sci. Rep.* **2012**, *2*, 591.

(4) Bisquert, J.; Qi, Y. B.; Ma, T.; Yan, Y. Advances and Obstacles on Perovskite Solar Cell Research from Material Properties to Photovoltaic Function. *ACS Energy Lett.* **2017**, *2*, 520−523.

(5) Xu, F.; Zhang, T.; Li, G.; Zhao, Y. Mixed Cation Hybrid Lead Halide Perovskites with Enhanced Performance and Stability. *J. Mater. Chem. A* **2017**, *5*, 11450−11461.

(6) Ha, S. T.; Su, R.; Xing, J.; Zhang, Q.; Xiong, Q. Metal Halide Perovskite Nanomaterials: Synthesis and Applications. *Chem. Sci.* **2017**, *8*, 2522−2536.

(7) Correa-Baena, J.-P.; Abate, A.; Saliba, M.; Tress, W.; Jesper Jacobsson, T.; Gratzel, M.; Hagfeldt, A. The Rapid Evolution of Highly Efficient Perovskite Solar Cells. *Energy Environ. Sci.* **2017**, *10*, 710−727.

(8) Zhou, Y.; Zhou, Z.; Chen, M.; Zong, Y.; Huang, J.; Pang, S.; Padture, N. P. Doping and alloying for improved perovskite solar cells. *J. Mater. Chem. A* **2016**, *4*, 17623−17635.

(9) Ono, L. K.; Qi, Y. B. Surface and Interface Aspects of Organometal Halide Perovskite Materials and Solar Cells. *J. Phys. Chem. Lett.* **2016**, *7*, 4764−4794.

(10) Park, N.-G.; Grätzel, M.; Miyasaka, T.; Zhu, K.; Emery, K. Towards stable and commercially available perovskite solar cells. *Nat. Energy* **2016**, *1*, 16152.

(11) Fan, Z.; Sun, K.; Wang, J. Perovskites for Photovoltaics: A Combined Review of Organic-Inorganic Halide Perovskites and Ferroelectric Oxide Perovskites. *J. Mater. Chem. A* **2015**, *3*, 18809−18828.

(12) Brenner, T. M.; Egger, D. A.; Kronik, L.; Hodes, G.; Cahen, D. Hybrid Organic—Inorganic Perovskites: Low-Cost Semiconductors

DOI: 10.1021/acsami.7b06001
ACS Appl. Mater. Interfaces XXXX, XXX, XXX−XXX

with Intriguing Charge-Transport Properties. *Nat. Rev. Mater.* **2016**, *1*, 15007.
(13) Ye, M.; Hong, X.; Zhang, F.; Liu, X. Recent Advancements in Perovskite Solar Cells: Flexibility, Stability and Large Scale. *J. Mater. Chem. A* **2016**, *4*, 6755−6771.
(14) Yin, W. J.; Yang, J. H.; Kang, J.; Yan, Y. F.; Wei, S. H. Halide Perovskite Materials for Solar Cells: A Theoretical Review. *J. Mater. Chem. A* **2015**, *3*, 8926−8942.
(15) Chen, Q.; De Marco, N.; Yang, Y.; Song, T. B.; Chen, C. C.; Zhao, H. X.; Hong, Z. R.; Zhou, H. P.; Yang, Y. Under the Spotlight: The Organic-Inorganic Hybrid Halide Perovskite for Optoelectronic Applications. *Nano Today* **2015**, *10*, 355−396.
(16) Berry, J.; Buonassisi, T.; Egger, D. A.; Hodes, G.; Kronik, L.; Loo, Y.-L.; Lubomirsky, I.; Marder, S. R.; Mastai, Y.; Miller, J. S.; et al. Hybrid Organic−Inorganic Perovskites (HOIPs): Opportunities and Challenges. *Adv. Mater.* **2015**, *27*, 5102−5112.
(17) Huang, J.; Shao, Y.; Dong, Q. Organometal Trihalide Perovskite Single Crystals: A Next Wave of Materials for 25% Efficiency Photovoltaics and Applications Beyond? *J. Phys. Chem. Lett.* **2015**, *6*, 3218−3227.
(18) Christians, J. A.; Manser, J. S.; Kamat, P. V. Multifaceted Excited State of $CH_3NH_3PbI_3$. Charge Separation, Recombination, and Trapping. *J. Phys. Chem. Lett.* **2015**, *6*, 2086−2095.
(19) Green, M. A.; Jiang, Y.; Soufiani, A. M.; Ho-Baillie, A. Optical Properties of Photovoltaic Organic−Inorganic Lead Halide Perovskites. *J. Phys. Chem. Lett.* **2015**, *6*, 4774−4785.
(20) Zheng, F.; Saldana-Greco, D.; Liu, S.; Rappe, A. M. Material Innovation in Advancing Organometal Halide Perovskite Functionality. *J. Phys. Chem. Lett.* **2015**, *6*, 4862−4872.
(21) Zhou, Y.; Game, O. S.; Pang, S.; Padture, N. P. Microstructures of Organometal Trihalide Perovskites for Solar Cells: Their Evolution from Solutions and Characterization. *J. Phys. Chem. Lett.* **2015**, *6*, 4827−4839.
(22) Zhu, X. Y.; Podzorov, V. Charge Carriers in Hybrid Organic−Inorganic Lead Halide Perovskites Might Be Protected as Large Polarons. *J. Phys. Chem. Lett.* **2015**, *6*, 4758−4761.
(23) Song, T. B.; Chen, Q.; Zhou, H. P.; Jiang, C. Y.; Wang, H. H.; Yang, Y.; Liu, Y. S.; You, J. B.; Yang, Y. Perovskite Solar Cells: Film Formation and Properties. *J. Mater. Chem. A* **2015**, *3*, 9032−9050.
(24) Luo, S. Q.; Daoud, W. A. Recent Progress in Organic-Inorganic Halide Perovskite Solar Cells: Mechanisms and Material Design. *J. Mater. Chem. A* **2015**, *3*, 8992−9010.
(25) Kazim, S.; Nazeeruddin, M. K.; Grätzel, M.; Ahmad, S. Perovskite as Light Harvester: A Game Changer in Photovoltaics. *Angew. Chem., Int. Ed.* **2014**, *53*, 2812−2824.
(26) Gao, P.; Grätzel, M.; Nazeeruddin, M. K. Organohalide Lead Perovskites for Photovoltaic Applications. *Energy Environ. Sci.* **2014**, *7*, 2448−2463.
(27) Lee, M. V.; Raga, S. R.; Kato, Y.; Leyden, M. R.; Ono, L. K.; Wang, S.; Qi, Y. Transamidation of Dimethylformamide during Alkylammonium Lead Triiodide Film Formation for Perovskite Solar Cells. *J. Mater. Res.* **2017**, *32*, 45−55.
(28) Wang, S.; Jiang, Y.; Juarez-Perez, E. J.; Ono, L. K.; Qi, Y. B. Accelerated Degradation of Methylammonium Lead Iodide Perovskites Induced by Exposure to Iodine Vapour. *Nat. Energy* **2016**, *2*, 16195.
(29) Juarez-Perez, E. J.; Hawash, Z.; Raga, S. R.; Ono, L. K.; Qi, Y. B. Thermal Degradation of $CH_3NH_3PbI_3$ Perovskite into NH_3 and CH_3I Gases Observed by Coupled Thermogravimetry-Mass Spectrometry Analysis. *Energy Environ. Sci.* **2016**, *9*, 3406−3410.
(30) Jung, M.-C.; Qi, Y. B. Dopant Interdiffusion Effects in n-i-p Structured Spiro-OMeTAD Hole Transport Layer of Organometal Halide Perovskite Solar Cells. *Org. Electron.* **2016**, *31*, 71−76.
(31) Jung, M.-C.; Lee, Y. M.; Lee, H.-K.; Park, J.; Raga, S. R.; Ono, L. K.; Wang, S.; Leyden, M. R.; Yu, B. D.; Hong, S.; et al. The Presence of CH_3NH_2 Neutral Species in Organometal Halide Perovskite Films. *Appl. Phys. Lett.* **2016**, *108*, 073901.
(32) Juarez-Perez, E. J.; Leyden, M. R.; Wang, S.; Ono, L. K.; Hawash, Z.; Qi, Y. B. Role of the Dopants on the Morphological and Transport Properties of Spiro-MeOTAD Hole Transport Layer. *Chem. Mater.* **2016**, *28*, 5702−5709.
(33) Hawash, Z.; Ono, L. K.; Qi, Y. B. Moisture and Oxygen Enhance Conductivity of LiTFSI-Doped Spiro-MeOTAD Hole Transport Layer in Perovskite Solar Cells. *Adv. Mater. Interfaces* **2016**, *3*, 1600117.
(34) Ohmann, R.; Ono, L. K.; Kim, H.-S.; Lin, H.; Lee, M. V.; Li, Y.; Park, N.-G.; Qi, Y. B. Real-Space Imaging of the Atomic Structure of Organic−Inorganic Perovskite. *J. Am. Chem. Soc.* **2015**, *137*, 16049−16054.
(35) Ono, L. K.; Raga, S. R.; Remeika, M.; Winchester, A. J.; Gabe, A.; Qi, Y. B. Pinhole-Free Hole Transport Layers Significantly Improve the Stability of $MAPbI_3$-Based Perovskite Solar Cells Under Operating Conditions. *J. Mater. Chem. A* **2015**, *3*, 15451−15456.
(36) Hawash, Z.; Ono, L. K.; Raga, S. R.; Lee, M. V.; Qi, Y. B. Air-Exposure Induced Dopant Redistribution and Energy Level Shifts in Spin-Coated Spiro-MeOTAD Films. *Chem. Mater.* **2015**, *27*, 562−569.
(37) Kato, Y.; Ono, L. K.; Lee, M. V.; Wang, S. H.; Raga, S. R.; Qi, Y. B. Silver Iodide Formation in Methyl Ammonium Lead Iodide Perovskite Solar Cells with Silver Top Electrodes. *Adv. Mater. Interfaces* **2015**, *2*, 1500195.
(38) Ono, L. K.; Raga, S. R.; Wang, S.; Kato, Y.; Qi, Y. B. Temperature-Dependent Hysteresis Effects in Perovskite-Based Solar Cells. *J. Mater. Chem. A* **2015**, *3*, 9074−9080.
(39) Ono, L. K.; Schulz, P.; Endres, J. J.; Nikiforov, G. O.; Kato, Y.; Kahn, A.; Qi, Y. B. Air-Exposure-Induced Gas-Molecule Incorporation into Spiro-MeOTAD Films. *J. Phys. Chem. Lett.* **2014**, *5*, 1374−1379.
(40) National Renewable Energy Laboratory (NREL). Research Cell Efficiency Records. http://www.nrel.gov/ncpv/images/efficiency_chart.jpg (accessed March 21st, 2017).
(41) Green, M. A.; Ho-Baillie, A.; Snaith, H. J. The Emergence of Perovskite Solar Cells. *Nat. Photonics* **2014**, *8*, 506−514.
(42) Park, N. G. Organometal Perovskite Light Absorbers Toward a 20% Efficiency Low-Cost Solid-State Mesoscopic Solar Cell. *J. Phys. Chem. Lett.* **2013**, *4*, 2423−2429.
(43) Snaith, H. J. Perovskites: The Emergence of a New Era for Low-Cost, High-Efficiency Solar Cells. *J. Phys. Chem. Lett.* **2013**, *4*, 3623−3630.
(44) Seo, J.; Noh, J. H.; Seok, S. I. Rational Strategies for Efficient Perovskite Solar Cells. *Acc. Chem. Res.* **2016**, *49*, 562−572.
(45) Acik, M.; Darling, S. B. Graphene in Perovskite Solar Cells: Device Design, Characterization and Implementation. *J. Mater. Chem. A* **2016**, *4*, 6185−6235.
(46) Docampo, P.; Bein, T. A Long-Term View on Perovskite Optoelectronics. *Acc. Chem. Res.* **2016**, *49*, 339−346.
(47) Ono, L. K.; Leyden, M. R.; Wang, S.; Qi, Y. B. Organometal Halide Perovskite Thin Films and Solar Cells by Vapor Deposition. *J. Mater. Chem. A* **2016**, *4*, 6693−6713.
(48) Remeika, M.; Raga, S. R.; Zhang, S.; Qi, Y. B. Transferrable Optimization of Spray-Coated PbI_2 Films for Perovskite Solar Cell Fabrication. *J. Mater. Chem. A* **2017**, *5*, 5709−5718.
(49) Leyden, M. R.; Jiang, Y.; Qi, Y. B. Chemical Vapor Deposition Grown Formamidinium Perovskite Solar Modules with High Steady State Power and Thermal Stability. *J. Mater. Chem. A* **2016**, *4*, 13125−13132.
(50) Raga, S. R.; Ono, L. K.; Qi, Y. B. Rapid Perovskite Formation by CH_3NH_2 Gas-Induced Intercalation and Reaction of PbI_2. *J. Mater. Chem. A* **2016**, *4*, 2494−2500.
(51) Raga, S. R.; Qi, Y. The Effect of Impurities on the Impedance Spectroscopy Response of $CH_3NH_3PbI_3$ Perovskite Solar Cells. *J. Phys. Chem. C* **2016**, *120*, 28519−28526.
(52) Jiang, Y.; Juarez-Perez, E. J.; Ge, Q.; Wang, S.; Leyden, M. R.; Ono, L. K.; Raga, S. R.; Hu, J.; Qi, Y. Post-Annealing of $MAPbI_3$ Perovskite Films with Methylamine for Efficient Perovskite Solar Cells. *Mater. Horiz.* **2016**, *3*, 548−555.
(53) Jung, M.-C.; Raga, S. R.; Qi, Y. B. Properties and Solar Cell Applications of Pb-Free Perovskite Films Formed by Vapor Deposition. *RSC Adv.* **2016**, *6*, 2819−2825.

DOI: 10.1021/acsami.7b06001
ACS Appl. Mater. Interfaces XXXX, XXX, XXX−XXX

(54) Leyden, M. R.; Lee, M. V.; Raga, S. R.; Qi, Y. B. Large Formamidinium Lead Trihalide Perovskite Solar Cells Using Chemical Vapor Deposition with High Reproducibility and Tunable Chlorine Concentrations. *J. Mater. Chem. A* **2015**, *3*, 16097−16103.
(55) Raga, S. R.; Jung, M.-C.; Lee, M. V.; Leyden, M. R.; Kato, Y.; Qi, Y. B. Influence of Air Annealing on High Efficiency Planar Structure Perovskite Solar Cells. *Chem. Mater.* **2015**, *27*, 1597−1603.
(56) Wang, S.; Ono, L. K.; Leyden, M. R.; Kato, Y.; Raga, S. R.; Lee, M. V.; Qi, Y. B. Smooth Perovskite Thin Films and Efficient Perovskite Solar Cells Prepared by the Hybrid Deposition Method. *J. Mater. Chem. A* **2015**, *3*, 14631−14641.
(57) Leyden, M. R.; Ono, L. K.; Raga, S. R.; Kato, Y.; Wang, S. H.; Qi, Y. B. High Performance Perovskite Solar Cells by Hybrid Chemical Vapor Deposition. *J. Mater. Chem. A* **2014**, *2*, 18742−18745.
(58) Ono, L. K.; Wang, S.; Kato, Y.; Raga, S. R.; Qi, Y. B. Semi-Transparent Perovskite Films with Centimeter-scale Superior Uniformity by the Hybrid Deposition Method. *Energy Environ. Sci.* **2014**, *7*, 3989−3993.
(59) Burschka, J.; Pellet, N.; Moon, S. J.; Humphry-Baker, R.; Gao, P.; Nazeeruddin, M. K.; Grätzel, M. Sequential Deposition as a Route to High-Performance Perovskite-Sensitized Solar Cells. *Nature* **2013**, *499*, 316−319.
(60) Lee, M. M.; Teuscher, J.; Miyasaka, T.; Murakami, T. N.; Snaith, H. J. Efficient Hybrid Solar Cells Based on Meso-Superstructured Organometal Halide Perovskites. *Science* **2012**, *338*, 643−647.
(61) Liu, M. Z.; Johnston, M. B.; Snaith, H. J. Efficient Planar Heterojunction Perovskite Solar Cells by Vapour Deposition. *Nature* **2013**, *501*, 395−398.
(62) Jeon, N. J.; Noh, J. H.; Kim, Y. C.; Yang, W. S.; Ryu, S.; Seok, S. I. Solvent Engineering for High-Performance Inorganic−Organic Hybrid Perovskite Solar Cells. *Nat. Mater.* **2014**, *13*, 897−903.
(63) Jeon, N. J.; Noh, J. H.; Yang, W. S.; Kim, Y. C.; Ryu, S.; Seo, J.; Seok, S. I. Compositional Engineering of Perovskite Materials for High-Performance Solar Cells. *Nature* **2015**, *517*, 476−480.
(64) Yang, W. S.; Noh, J. H.; Jeon, N. J.; Kim, Y. C.; Ryu, S.; Seo, J.; Seok, S. I. High-Performance Photovoltaic Perovskite Layers Fabricated through Intramolecular Exchange. *Science* **2015**, *348*, 1234−1237.
(65) Saliba, M.; Matsui, T.; Seo, J.-Y.; Domanski, K.; Correa-Baena, J.-P.; Nazeeruddin, M. K.; Zakeeruddin, S. M.; Tress, W.; Abate, A.; Hagfeldt, A.; et al. Cesium-Containing Triple Cation Perovskite Solar Cells: Improved Stability, Reproducibility and High Efficiency. *Energy Environ. Sci.* **2016**, *9*, 1989−1997.
(66) Green, M. A.; Emery, K.; Hishikawa, Y.; Warta, W.; Dunlop, E. D. Solar cell efficiency tables (version 48). *Prog. Photovoltaics* **2016**, *24*, 905−913.
(67) Walsh, A. Principles of Chemical Bonding and Band Gap Engineering in Hybrid Organic−Inorganic Halide Perovskites. *J. Phys. Chem. C* **2015**, *119*, 5755−5760.
(68) Wang, B.; Xiao, X.; Chen, T. Perovskite Photovoltaics: A High-Efficiency Newcomer to the Solar Cell Family. *Nanoscale* **2014**, *6*, 12287−12297.
(69) Bakulin, A. A.; Selig, O.; Bakker, H. J.; Rezus, Y. L. A.; Müller, C.; Glaser, T.; Lovrincic, R.; Sun, Z.; Chen, Z.; Walsh, A.; et al. Real-Time Observation of Organic Cation Reorientation in Methylammonium Lead Iodide Perovskites. *J. Phys. Chem. Lett.* **2015**, *6*, 3663−3669.
(70) Leguy, A. M. A.; Frost, J. M.; McMahon, A. P.; Sakai, V. G.; Kochelmann, W.; Law, C.; Li, X.; Foglia, F.; Walsh, A.; O'Regan, B. C.; et al. The Dynamics of Methylammonium Ions in Hybrid Organic-Inorganic Perovskite Solar Cells. *Nat. Commun.* **2015**, *6*, 7124.
(71) Leguy, A. M. A.; Goni, A. R.; Frost, J. M.; Skelton, J.; Brivio, F.; Rodriguez-Martinez, X.; Weber, O. J.; Pallipurath, A.; Alonso, M. I.; Campoy-Quiles, M.; et al. Dynamic Disorder, Phonon Lifetimes, and the Assignment of Modes to the Vibrational Spectra of Methylammonium Lead Halide Perovskites. *Phys. Chem. Chem. Phys.* **2016**, *18*, 27051−27066.
(72) Miyasaka, T. Perovskite Photovoltaics: Rare Functions of Organo Lead Halide in Solar Cells and Optoelectronic Devices. *Chem. Lett.* **2015**, *44*, 720−729.
(73) Brivio, F.; Walker, A. B.; Walsh, A. Structural and Electronic Properties of Hybrid Perovskites for High-Efficiency Thin-Film Photovoltaics from First-Principles. *APL Mater.* **2013**, *1*, 042111.
(74) Brivio, F.; Butler, K. T.; Walsh, A.; van Schilfgaarde, M. Relativistic Quasiparticle Self-Consistent Electronic Structure of Hybrid Halide Perovskite Photovoltaic Absorbers. *Phys. Rev. B: Condens. Matter Mater. Phys.* **2014**, *89*, 155204.
(75) De Angelis, F. Modeling Materials and Processes in Hybrid/Organic Photovoltaics: From Dye-Sensitized to Perovskite Solar Cells. *Acc. Chem. Res.* **2014**, *47*, 3349−3360.
(76) Umari, P.; Mosconi, E.; De Angelis, F. Relativistic GW calculations on $CH_3NH_3PbI_3$ and $CH_3NH_3SnI_3$ Perovskites for Solar Cell Applications. *Sci. Rep.* **2015**, *4*, 4467.
(77) Quarti, C.; Mosconi, E.; De Angelis, F. Interplay of Orientational Order and Electronic Structure in Methylammonium Lead Iodide: Implications for Solar Cell Operation. *Chem. Mater.* **2014**, *26*, 6557−6569.
(78) Etienne, T.; Mosconi, E.; De Angelis, F. Dynamical Origin of the Rashba Effect in Organohalide Lead Perovskites: A Key to Suppressed Carrier Recombination in Perovskite Solar Cells? *J. Phys. Chem. Lett.* **2016**, *7*, 1638−1645.
(79) Quarti, C.; De Angelis, F.; Beljonne, D. Influence of Surface Termination on the Energy Level Alignment at the $CH_3NH_3PbI_3$ Perovskite/C60 Interface. *Chem. Mater.* **2017**, *29*, 958−968.
(80) Shirayama, M.; Kadowaki, H.; Miyadera, T.; Sugita, T.; Tamakoshi, M.; Kato, M.; Fujiseki, T.; Murata, D.; Hara, S.; Murakami, T. N.; et al. Optical Transitions in Hybrid Perovskite Solar Cells: Ellipsometry, Density Functional Theory, and Quantum Efficiency Analyses for $CH_3NH_3PbI_3$. *Phys. Rev. Appl.* **2016**, *5*, 014012.
(81) Saparov, B.; Mitzi, D. B. Organic−Inorganic Perovskites: Structural Versatility for Functional Materials Design. *Chem. Rev.* **2016**, *116*, 4558−4596.
(82) Stoumpos, C. C.; Malliakas, C. D.; Kanatzidis, M. G. Semiconducting Tin and Lead Iodide Perovskites with Organic Cations: Phase Transitions, High Mobilities, and Near-Infrared Photoluminescent Properties. *Inorg. Chem.* **2013**, *52*, 9019−9038.
(83) Weber, O. J.; Charles, B.; Weller, M. T. Phase Behaviour and Composition in the Formamidinium-Methylammonium Hybrid Lead Iodide Perovskite Solid Solution. *J. Mater. Chem. A* **2016**, *4*, 15375−15382.
(84) Nagabhushana, G. P.; Shivaramaiah, R.; Navrotsky, A. Direct Calorimetric Verification of Thermodynamic Instability of Lead Halide Hybrid Perovskites. *Proc. Natl. Acad. Sci. U. S. A.* **2016**, *113*, 7717−7721.
(85) Brandt, R. E.; Stevanovic, V.; Ginley, D. S.; Buonassisi, T. Identifying Defect-Tolerant Semiconductors with High Minority-Carrier Lifetimes: Beyond Hybrid Lead Halide Perovskites. *MRS Commun.* **2015**, *5*, 265−275.
(86) Umebayashi, T.; Asai, K.; Kondo, T.; Nakao, A. Electronic Structures of Lead Iodide Based Low-Dimensional Crystals. *Phys. Rev. B: Condens. Matter Mater. Phys.* **2003**, *67*, 155405.
(87) Lee, J.-H.; Bristowe, N. C.; Lee, J. H.; Lee, S.-H.; Bristowe, P. D.; Cheetham, A. K.; Jang, H. M. Resolving the Physical Origin of Octahedral Tilting in Halide Perovskites. *Chem. Mater.* **2016**, *28*, 4259−4266.
(88) Yin, W.-J.; Shi, T.; Yan, Y. Unique Properties of Halide Perovskites as Possible Origins of the Superior Solar Cell Performance. *Adv. Mater.* **2014**, *26*, 4653−4658.
(89) Yin, W.-J.; Shi, T.; Yan, Y. Unusual Defect Physics in $CH_3NH_3PbI_3$ Perovskite Solar Cell Absorber. *Appl. Phys. Lett.* **2014**, *104*, 063903.
(90) Jacobsson, T. J.; Correa-Baena, J.-P.; Pazoki, M.; Saliba, M.; Schenk, K.; Gratzel, M.; Hagfeldt, A. Exploration of the Compositional Space for Mixed Lead Halogen Perovskites for High Efficiency Solar Cells. *Energy Environ. Sci.* **2016**, *9*, 1706−1724.

AQ

(91) Shockley, W.; Queisser, H. J. Detailed Balance Limit of Efficiency of P-N Junction Solar Cells. *J. Appl. Phys.* **1961**, *32*, 510−519.
(92) Berhe, T. A.; Su, W.-N.; Chen, C.-H.; Pan, C.-J.; Cheng, J.-H.; Chen, H.-M.; Tsai, M.-C.; Chen, L.-Y.; Dubale, A. A.; Hwang, B.-J. Organometal Halide Perovskite Solar Cells: Degradation and Stability. *Energy Environ. Sci.* **2016**, *9*, 323−356.
(93) Xu, T.; Chen, L.; Guo, Z.; Ma, T. Strategic Improvement of The Long-Term Stability of Perovskite Materials and Perovskite Solar Cells. *Phys. Chem. Chem. Phys.* **2016**, *18*, 27026−27050.
(94) Carignano, M. A.; Saeed, Y.; Aravindh, S. A.; Roqan, I. S.; Even, J.; Katan, C. A Close Examination of the Structure and Dynamics of $HC(NH_2)_2PbI_3$ by MD Simulations and Group Theory. *Phys. Chem. Chem. Phys.* **2016**, *18*, 27109−27118.
(95) Hakamata, T.; Shimamura, K.; Shimojo, F.; Kalia, R. K.; Nakano, A.; Vashishta, P. The Nature of Free-Carrier Transport in Organometal Halide Perovskites. *Sci. Rep.* **2016**, *6*, 19599.
(96) Beecher, A. N.; Semonin, O. E.; Skelton, J. M.; Frost, J. M.; Terban, M. W.; Zhai, H.; Alatas, A.; Owen, J. S.; Walsh, A.; Billinge, S. J. L. Direct Observation of Dynamic Symmetry Breaking above Room Temperature in Methylammonium Lead Iodide Perovskite. *ACS Energy Lett.* **2016**, *1*, 880−887.
(97) Bergmann, V. W.; Guo, Y.; Tanaka, H.; Hermes, I. M.; Li, D.; Klasen, A.; Bretschneider, S. A.; Nakamura, E.; Berger, R.; Weber, S. A. L. Local Time-Dependent Charging in a Perovskite Solar Cell. *ACS Appl. Mater. Interfaces* **2016**, *8*, 19402−19409.
(98) Sutton, R. J.; Eperon, G. E.; Miranda, L.; Parrott, E. S.; Kamino, B. A.; Patel, J. B.; Hörantner, M. T.; Johnston, M. B.; Haghighirad, A. A.; Moore, D. T.; et al. Bandgap-Tunable Cesium Lead Halide Perovskites with High Thermal Stability for Efficient Solar Cells. *Adv. Energy Mater.* **2016**, *6*, 1502458.
(99) Lee, J.-W.; Seol, D.-J.; Cho, A.-N.; Park, N.-G. High-Efficiency Perovskite Solar Cells Based on the Black Polymorph of $HC(NH_2)_2PbI_3$. *Adv. Mater.* **2014**, *26*, 4991−4998.
(100) Lee, J.-W.; Kim, D.-H.; Kim, H.-S.; Seo, S.-W.; Cho, S. M.; Park, N.-G. Formamidinium and Cesium Hybridization for Photo- and Moisture-Stable Perovskite Solar Cell. *Adv. Energy Mater.* **2015**, *5*, 1501310.
(101) Li, Z.; Yang, M.; Park, J.-S.; Wei, S.-H.; Berry, J. J.; Zhu, K. Stabilizing Perovskite Structures by Tuning Tolerance Factor: Formation of Formamidinium and Cesium Lead Iodide Solid-State Alloys. *Chem. Mater.* **2016**, *28*, 284−292.
(102) Pellet, N.; Gao, P.; Gregori, G.; Yang, T.-Y.; Nazeeruddin, M. K.; Maier, J.; Grätzel, M. Mixed-Organic-Cation Perovskite Photovoltaics for Enhanced Solar-Light Harvesting. *Angew. Chem., Int. Ed.* **2014**, *53*, 3151−3157.
(103) Aharon, S.; Dymshits, A.; Rotem, A.; Etgar, L. Temperature Dependence of Hole Conductor Free Formamidinium Lead Iodide Perovskite Based Solar Cells. *J. Mater. Chem. A* **2015**, *3*, 9171−9178.
(104) Salado, M.; Calio, L.; Berger, R.; Kazim, S.; Ahmad, S. Influence of the Mixed Organic Cation Ratio in Lead Iodide Based Perovskite on the Performance of Solar Cells. *Phys. Chem. Chem. Phys.* **2016**, *18*, 27148−27157.
(105) Mahmud, M. A.; Elumalai, N. K.; Upama, M. B.; Wang, D.; Wright, M.; Chan, K. H.; Xu, C.; Haque, F.; Uddin, A. Single Vs Mixed Organic Cation for Low Temperature Processed Perovskite Solar Cells. *Electrochim. Acta* **2016**, *222*, 1510−1521.
(106) Binek, A.; Hanusch, F. C.; Docampo, P.; Bein, T. Stabilization of the Trigonal High-Temperature Phase of Formamidinium Lead Iodide. *J. Phys. Chem. Lett.* **2015**, *6*, 1249−1253.
(107) Ji, F.; Wang, L.; Pang, S.; Gao, P.; Xu, H.; Xie, G.; Zhang, J.; Cui, G. A Balanced Cation Exchange Reaction Toward Highly Uniform and Pure Phase $FA_{1-x}MA_xPbI_3$ Perovskite Films. *J. Mater. Chem. A* **2016**, *4*, 14437−14443.
(108) Li, G.; Zhang, T.; Guo, N.; Xu, F.; Qian, X.; Zhao, Y. Ion-Exchange-Induced 2D−3D Conversion of $HMA_{1-x}FA_xPbI_3Cl$ Perovskite into a High-Quality $MA_{1-x}FA_xPbI_3$ Perovskite. *Angew. Chem., Int. Ed.* **2016**, *55*, 13460−13464.
(109) Liu, J.; Shirai, Y.; Yang, X.; Yue, Y.; Chen, W.; Wu, Y.; Islam, A.; Han, L. High-Quality Mixed-Organic-Cation Perovskites from a Phase-Pure Non-stoichiometric Intermediate $(FAI)_{1-x}$-PbI_2 for Solar Cells. *Adv. Mater.* **2015**, *27*, 4918−4923.
(110) Chen, C.-C.; Chang, S. H.; Chen, L.-C.; Kao, F.-S.; Cheng, H.-M.; Yeh, S.-C.; Chen, C.-T.; Wu, W.-T.; Tseng, Z.-L.; Chuang, C. L.; et al. Improving the Efficiency of Inverted Mixed-Organic-Cation Perovskite Absorber based Photovoltaics by Tailing the Surface Roughness of PEDOT: PSS Thin Film. *Sol. Energy* **2016**, *134*, 445−451.
(111) Deng, Y.; Dong, Q.; Bi, C.; Yuan, Y.; Huang, J. Air-Stable, Efficient Mixed-Cation Perovskite Solar Cells with Cu Electrode by Scalable Fabrication of Active Layer. *Adv. Energy Mater.* **2016**, *6*, 1600372.
(112) Kim, J.; Kim, H. P.; Teridi, M. A. M.; Yusoff, A. R. b. M.; Jang, J. Bandgap Tuning of Mixed Organic Cation Utilizing Chemical Vapor Deposition Process. *Sci. Rep.* **2016**, *6*, 37378.
(113) Chen, J.; Xu, J.; Xiao, L.; Zhang, B.; Dai, S.; Yao, J. Mixed-Organic-Cation $(FA)_x(MA)_{1-x}PbI_3$ Planar Perovskite Solar Cells with 16.48% Efficiency via a Low-Pressure Vapor-Assisted Solution Process. *ACS Appl. Mater. Interfaces* **2017**, *9*, 2449−2458.
(114) Frost, J. M.; Butler, K. T.; Brivio, F.; Hendon, C. H.; van Schilfgaarde, M.; Walsh, A. Atomistic Origins of High-Performance in Hybrid Halide Perovskite Solar Cells. *Nano Lett.* **2014**, *14*, 2584−2590.
(115) Choi, H.; Jeong, J.; Kim, H.-B.; Kim, S.; Walker, B.; Kim, G.-H.; Kim, J. Y. Cesium-Doped Methylammonium Lead Iodide Perovskite Light Absorber for Hybrid Solar Cells. *Nano Energy* **2014**, *7*, 80−85.
(116) Niu, G.; Li, W.; Li, J.; Liang, X.; Wang, L. Enhancement of Thermal Stability for Perovskite Solar Cells through Cesium Doping. *RSC Adv.* **2017**, *7*, 17473−17479.
(117) Yi, C.; Luo, J.; Meloni, S.; Boziki, A.; Ashari-Astani, N.; Gratzel, C.; Zakeeruddin, S. M.; Rothlisberger, U.; Gratzel, M. Entropic Stabilization of Mixed A-Cation ABX_3 Metal Halide Perovskites for High Performance Perovskite Solar Cells. *Energy Environ. Sci.* **2016**, *9*, 656−662.
(118) Yu, Y.; Wang, C.; Grice, C. R.; Shrestha, N.; Chen, J.; Zhao, D.; Liao, W.; Cimaroli, A. J.; Roland, P. J.; Ellingson, R. J.; et al. Improving the Performance of Formamidinium and Cesium Lead Triiodide Perovskite Solar Cells using Lead Thiocyanate Additives. *ChemSusChem* **2016**, *9*, 3288−3297.
(119) Liu, T.; Zong, Y.; Zhou, Y.; Yang, M.; Li, Z.; Game, O. S.; Zhu, K.; Zhu, R.; Gong, Q.; Padture, N. P. High-Performance Formamidinium-Based Perovskite Solar Cells via Microstructure-Mediated δ-to-α Phase Transformation. *Chem. Mater.* **2017**, *29*, 3246−3250.
(120) Huang, J.; Xu, P.; Liu, J.; You, X.-Z. Sequential Introduction of Cations Deriving Large-Grain $Cs_xFA_{1-x}PbI_3$ Thin Film for Planar Hybrid Solar Cells: Insight into Phase-Segregation and Thermal-Healing Behavior. *Small* **2017**, *13*, 1603225.
(121) Park, Y. H.; Jeong, I.; Bae, S.; Son, H. J.; Lee, P.; Lee, J.; Lee, C.-H.; Ko, M. J. Inorganic Rubidium Cation as an Enhancer for Photovoltaic Performance and Moisture Stability of $HC(NH_2)_2PbI_3$ Perovskite Solar Cells. *Adv. Funct. Mater.* **2017**, *27*, 1605988.
(122) Zhang, M.; Yun, J. S.; Ma, Q.; Zheng, J.; Lau, C. F. J.; Deng, X.; Kim, J.; Kim, D.; Seidel, J.; Green, M. A.; et al. High-Efficiency Rubidium-Incorporated Perovskite Solar Cells by Gas Quenching. *ACS Energy Lett.* **2017**, *2*, 438−444.
(123) Niu, G.; Yu, H.; Li, J.; Wang, D.; Wang, L. Controlled Orientation of Perovskite Films Through Mixed Cations Toward High Performance Perovskite Solar Cells. *Nano Energy* **2016**, *27*, 87−94.
(124) Chen, B.-X.; Li, W.-G.; Rao, H.-S.; Xu, Y.-F.; Kuang, D.-B.; Su, C.-Y. Large-Grained Perovskite Films via $FA_xMA_{1-x}Pb(I_xBr_{1-x})_3$ Single Crystal Precursor for Efficient Solar Cells. *Nano Energy* **2017**, *34*, 264−270.
(125) Zheng, X.; Wu, C.; Jha, S. K.; Li, Z.; Zhu, K.; Priya, S. Improved Phase Stability of Formamidinium Lead Triiodide Perovskite by Strain Relaxation. *ACS Energy Lett.* **2016**, *1*, 1014−1020.

DOI: 10.1021/acsami.7b06001
ACS Appl. Mater. Interfaces XXXX, XXX, XXX−XXX

(126) Chen, L. C.; Tseng, Z. L.; Huang, J. K. A Study of Inverted-Type Perovskite Solar Cells with Various Composition Ratios of $(FAPbI_3)_{(1-x)}(MAPbBr_3)_x$. *Nanomaterials* **2016**, *6*, 183.
(127) Sveinbjornsson, K.; Aitola, K.; Zhang, J.; Johansson, M. B.; Zhang, X.; Correa-Baena, J.-P.; Hagfeldt, A.; Boschloo, G.; Johansson, E. M. J. Ambient Air-Processed Mixed-Ion Perovskites for High-Efficiency Solar Cells. *J. Mater. Chem. A* **2016**, *4*, 16536−16545.
(128) Reyna, Y.; Salado, M.; Kazim, S.; Pérez-Tomas, A.; Ahmad, S.; Lira-Cantu, M. Performance and Stability of Mixed FAPbI$_{3(0.85)}$MAPbBr$_{3(0.15)}$ Halide Perovskite Solar Cells Under Outdoor Conditions and the Effect of Low Light Irradiation. *Nano Energy* **2016**, *30*, 570−579.
(129) Chen, L.-C.; Wu, J.-R.; Tseng, Z.-L.; Chen, C.-C.; Chang, S.; Huang, J.-K.; Lee, K.-L.; Cheng, H.-M. Annealing Effect on $(FAPbI_3)_{1-x}(MAPbBr_3)_x$ Perovskite Films in Inverted-Type Perovskite Solar Cells. *Materials* **2016**, *9*, 747.
(130) Bi, D.; Tress, W.; Dar, M. I.; Gao, P.; Luo, J.; Renevier, C.; Schenk, K.; Abate, A.; Giordano, F.; Correa Baena, J.-P.; et al. Efficient Luminescent Solar Cells Based on Tailored Mixed-Cation Perovskites. *Sci. Adv.* **2016**, *2*, e1501170.
(131) Isikgor, F. H.; Li, B.; Zhu, H.; Xu, Q.; Ouyang, J. High Performance Planar Perovskite Solar Cells With A Perovskite Of Mixed Organic Cations And Mixed Halides, $MA_{1-x}FA_xPbI_{3-y}Cl_y$. *J. Mater. Chem. A* **2016**, *4*, 12543−12553.
(132) McMeekin, D. P.; Sadoughi, G.; Rehman, W.; Eperon, G. E.; Saliba, M.; Hörantner, M. T.; Haghighirad, A.; Sakai, N.; Korte, L.; Rech, B.; et al. A Mixed-Cation Lead Mixed-Halide Perovskite Absorber for Tandem Solar Cells. *Science* **2016**, *351*, 151−155.
(133) Bush, K. A.; Palmstrom, A. F.; Yu, Z. J.; Boccard, M.; Cheacharoen, R.; Mailoa, J. P.; McMeekin, D. P.; Hoye, R. L. Z.; Bailie, C. D.; Leijtens, T.; et al. 23.6%-Efficient Monolithic Perovskite/Silicon Tandem Solar Cells with Improved Stability. *Nat. Energy* **2017**, *2*, 17009.
(134) Wang, Z.; McMeekin, D. P.; Sakai, N.; van Reenen, S.; Wojciechowski, K.; Patel, J. B.; Johnston, M. B.; Snaith, H. J. Efficient and Air-Stable Mixed-Cation Lead Mixed-Halide Perovskite Solar Cells with n-Doped Organic Electron Extraction Layers. *Adv. Mater.* **2017**, *29*, 1604186.
(135) Matsui, T.; Seo, J.-Y.; Saliba, M.; Zakeeruddin, S. M.; Grätzel, M. Room-Temperature Formation of Highly Crystalline Multication Perovskites for Efficient, Low-Cost Solar Cells. *Adv. Mater.* **2017**, *29*, 1606258.
(136) Duong, T.; Mulmudi, H. K.; Shen, H.; Wu, Y.; Barugkin, C.; Mayon, Y. O.; Nguyen, H. T.; Macdonald, D.; Peng, J.; Lockrey, M.; et al. Structural Engineering Using Rubidium Iodide as a Dopant Under Excess Lead Iodide Conditions for High Efficiency and Stable Perovskites. *Nano Energy* **2016**, *30*, 330−340.
(137) Saliba, M.; Matsui, T.; Domanski, K.; Seo, J. Y.; Ummadisingu, A.; Zakeeruddin, S. M.; Correa-Baena, J. P.; Tress, W. R.; Abate, A.; Hagfeldt, A.; et al. Incorporation of Rubidium Cations Into Perovskite Solar Cells Improves Photovoltaic Performance. *Science* **2016**, *354*, 206−209.
(138) Duong, T.; Wu, Y.; Shen, H.; Peng, J.; Fu, X.; Jacobs, D.; Wang, E.-C.; Kho, T. C.; Fong, K. C.; Stocks, M.; et al. Rubidium Multication Perovskite with Optimized Bandgap for Perovskite-Silicon Tandem with over 26% Efficiency. *Adv. Energy Mater.* **2017**, *7*, 1700228.
(139) Son, D.-Y.; Lee, J.-W.; Choi, Y. J.; Jang, I.-H.; Lee, S.; Yoo, P. J.; Shin, H.; Ahn, N.; Choi, M.; Kim, D.; et al. Self-Formed Grain Boundary Healing Layer for Highly Efficient $CH_3NH_3PbI_3$ Perovskite Solar Cells. *Nat. Energy* **2016**, *1*, 16081.
(140) Momblona, C.; Gil-Escrig, L.; Bandiello, E.; Hutter, E. M.; Sessolo, M.; Lederer, K.; Blochwitz-Nimoth, J.; Bolink, H. J. Efficient Vacuum Deposited p-i-n and n-i-p Perovskite Solar Cells Employing Doped Charge Transport Layers. *Energy Environ. Sci.* **2016**, *9*, 3456−3463.
(141) Wu, C.-G.; Chiang, C.-H.; Tseng, Z.-L.; Nazeeruddin, M. K.; Hagfeldt, A.; Gratzel, M. High efficiency stable inverted perovskite solar cells without current hysteresis. *Energy Environ. Sci.* **2015**, *8*, 2725−2733.
(142) Wang, F.; Yu, H.; Xu, H.; Zhao, N. $HPbI_3$: A New Precursor Compound for Highly Efficient Solution-Processed Perovskite Solar Cells. *Adv. Funct. Mater.* **2015**, *25*, 1120−1126.
(143) Zhou, Y.; Yang, M.; Pang, S.; Zhu, K.; Padture, N. P. Exceptional Morphology-Preserving Evolution of Formamidinium Lead Triiodide Perovskite Thin Films via Organic-Cation Displacement. *J. Am. Chem. Soc.* **2016**, *138*, 5535−5538.
(144) Pool, V. L.; Dou, B.; Van Campen, D. G.; Klein-Stockert, T. R.; Barnes, F. S.; Shaheen, S. E.; Ahmad, M. I.; van Hest, M. F. A. M.; Toney, M. F. Thermal engineering of FAPbI3 perovskite material via radiative thermal annealing and in situ XRD. *Nat. Commun.* **2017**, *8*, 14075.
(145) Lee, J.-W.; Kim, H.-S.; Park, N.-G. $APbI_3$ (A = CH_3NH_3 and $HC(NH_2)_2$) Perovskite Solar Cells: From Sensitization to Planar Heterojunction. In *Organic-Inorganic Halide Perovskite Photovoltaics, From Fundamentals to Device Architectures*; Park, N.-G., Miyasaka, T., Gratzel, M., Eds.; Springer International Publishing: Switzerland, 2016; pp 223−253.
(146) Amat, A.; Mosconi, E.; Ronca, E.; Quarti, C.; Umari, P.; Nazeeruddin, M. K.; Grätzel, M.; De Angelis, F. Cation-Induced Band-Gap Tuning in Organohalide Perovskites: Interplay of Spin−Orbit Coupling and Octahedra Tilting. *Nano Lett.* **2014**, *14*, 3608−3616.
(147) Eperon, G. E.; Stranks, S. D.; Menelaou, C.; Johnston, M. B.; Herz, L. M.; Snaith, H. J. Formamidinium Lead Trihalide: A Broadly Tunable Perovskite for Efficient Planar Heterojunction Solar Cells. *Energy Environ. Sci.* **2014**, *7*, 982−988.
(148) Zhang, T.; Meng, X.; Bai, Y.; Xiao, S.; Hu, C.; Yang, Y.; Chen, H.; Yang, S. Profiling the Organic Cation-Dependent Degradation of Organolead Halide Perovskite Solar Cells. *J. Mater. Chem. A* **2017**, *5*, 1103−1111.
(149) Weller, M. T.; Weber, O. J.; Frost, J. M.; Walsh, A. Cubic Perovskite Structure of Black Formamidinium Lead Iodide, α-$[HC(NH_2)_2]PbI_3$, at 298 K. *J. Phys. Chem. Lett.* **2015**, *6*, 3209−3212.
(150) Han, Q.; Bae, S.-H.; Sun, P.; Hsieh, Y.-T.; Yang, Y.; Rim, Y. S.; Zhao, H.; Chen, Q.; Shi, W.; Li, G.; et al. Single Crystal Formamidinium Lead Iodide ($FAPbI_3$): Insight into the Structural, Optical, and Electrical Properties. *Adv. Mater.* **2016**, *28*, 2253−2258.
(151) Ma, F.; Li, J.; Li, W.; Lin, N.; Wang, L.; Qiao, J. Stable alpha/delta Phase Junction of Formamidinium Lead Iodide Perovskites for Enhanced Near-Infrared Emission. *Chem. Sci.* **2017**, *8*, 800−805.
(152) Dai, J.; Fu, Y.; Manger, L. H.; Rea, M. T.; Hwang, L.; Goldsmith, R. H.; Jin, S. Carrier Decay Properties of Mixed Cation Formamidinium−Methylammonium Lead Iodide Perovskite $[HC(NH_2)_2]_{1-x}[CH_3NH_3]_xPbI_3$ Nanorods. *J. Phys. Chem. Lett.* **2016**, *7*, 5036−5043.
(153) Slimi, B.; Mollar, M.; Assaker, I. B.; Kriaa, I.; Chtourou, R.; Marí, B. Perovskite $FA_{1-x}MA_xPbI_3$ for Solar Cells: Films Formation and Properties. *Energy Procedia* **2016**, *102*, 87−95.
(154) El-Mellouhi, F.; Bentria, E. T.; Rashkeev, S. N.; Kais, S.; Alharbi, F. H. Enhancing Intrinsic Stability of Hybrid Perovskite Solar Cell by Strong, yet Balanced, Electronic Coupling. *Sci. Rep.* **2016**, *6*, 30305.
(155) Eperon, G. E.; Paterno, G. M.; Sutton, R. J.; Zampetti, A.; Haghighirad, A. A.; Cacialli, F.; Snaith, H. J. Inorganic Caesium Lead Iodide Perovskite Solar Cells. *J. Mater. Chem. A* **2015**, *3*, 19688−19695.
(156) Chen, Z.; Wang, J. J.; Ren, Y.; Yu, C.; Shum, K. Schottky Solar Cells Based on $CsSnI_3$ Thin-Films. *Appl. Phys. Lett.* **2012**, *101*, 093901.
(157) Syzgantseva, O. A.; Saliba, M.; Grätzel, M.; Rothlisberger, U. Stabilization of the Perovskite Phase of Formamidinium Lead Triiodide by Methylammonium, Cs, and/or Rb Doping. *J. Phys. Chem. Lett.* **2017**, *8*, 1191−1196.
(158) Kieslich, G.; Sun, S.; Cheetham, A. K. Solid-State Principles Applied to Organic-Inorganic Perovskites: New Tricks for an Old Dog. *Chem. Sci.* **2014**, *5*, 4712−4715.

DOI: 10.1021/acsami.7b06001
ACS Appl. Mater. Interfaces XXXX, XXX, XXX−XXX

(159) Kieslich, G.; Sun, S.; Cheetham, A. K. An extended Tolerance Factor approach for organic-inorganic perovskites. *Chem. Sci.* **2015**, *6*, 3430−3433.
(160) Travis, W.; Glover, E. N. K.; Bronstein, H.; Scanlon, D. O.; Palgrave, R. G. On the Application of the Tolerance Factor to Inorganic and Hybrid Halide Perovskites: A Revised System. *Chem. Sci.* **2016**, *7*, 4548−4556.
(161) Brgoch, J.; Lehner, A. J.; Chabinyc, M.; Seshadri, R. Ab Initio Calculations of Band Gaps and Absolute Band Positions of Polymorphs of $RbPbI_3$ and $CsPbI_3$: Implications for Main-Group Halide Perovskite Photovoltaics. *J. Phys. Chem. C* **2014**, *118*, 27721−27727.
(162) Jishi, R. A.; Ta, O. B.; Sharif, A. A. Modeling of Lead Halide Perovskites for Photovoltaic Applications. *J. Phys. Chem. C* **2014**, *118*, 28344−28349.
(163) Yunakova, O. N.; Miloslavskii, V. K.; Kovalenko, E. N. Exciton Absorption Spectrum of Thin $(KI)_{1-x}(PbI_2)_x$ Films. *Funct. Mater.* **2013**, *20*, 59−63.
(164) Trots, D. M.; Myagkota, S. V. High-Temperature Structural Evolution of Caesium and Rubidium Triiodoplumbates. *J. Phys. Chem. Solids* **2008**, *69*, 2520−2526.
(165) Ralaiarisoa, M.; Busby, Y.; Frisch, J.; Salzmann, I.; Pireaux, J.-J.; Koch, N. Correlation of Annealing Time with Crystal Structure, Composition, and Electronic Properties of $CH_3NH_3PbI_{3-x}Cl_x$ Mixed-Halide Perovskite Films. *Phys. Chem. Chem. Phys.* **2017**, *19*, 828−836.
(166) Heo, J. H.; Lee, M. H.; Jang, M. H.; Im, S. H. Highly Efficient $CH_3NH_3PbI_{3-x}Cl_x$ Mixed Halide Perovskite Solar Cells Prepared by Re-Dissolution and Crystal Grain Growth via Spray Coating. *J. Mater. Chem. A* **2016**, *4*, 17636−17642.
(167) Zhang, H.; Liao, Q.; Wang, X.; Hu, K.; Yao, J.; Fu, H. Controlled Substitution of Chlorine for Iodine in Single-Crystal Nanofibers of Mixed Perovskite $MAPbI_{3-x}Cl_x$. *Small* **2016**, *12*, 3780−3787.
(168) Sedighi, R.; Tajabadi, F.; Shahbazi, S.; Gholipour, S.; Taghavinia, N. Mixed-Halide $CH_3NH_3PbI_{3-x}X_x$ (X = Cl, Br, I) Perovskites: Vapor-Assisted Solution Deposition and Application as Solar Cell Absorbers. *ChemPhysChem* **2016**, *17*, 2382−2388.
(169) Pool, V. L.; Gold-Parker, A.; McGehee, M. D.; Toney, M. F. Chlorine in $PbCl_2$-Derived Hybrid-Perovskite Solar Absorbers. *Chem. Mater.* **2015**, *27*, 7240−7243.
(170) Chae, J.; Dong, Q.; Huang, J.; Centrone, A. Chloride Incorporation Process in $CH_3NH_3PbI_{3-x}Cl_x$ Perovskites via Nanoscale Bandgap Maps. *Nano Lett.* **2015**, *15*, 8114−8121.
(171) Luo, D.; Yu, L.; Wang, H.; Zou, T.; Luo, L.; Liu, Z.; Lu, Z. Cubic Structure of the Mixed Halide Perovskite $CH_3NH_3PbI_{3-x}Cl_x$ via Thermal Annealing. *RSC Adv.* **2015**, *5*, 85480−85485.
(172) Cojocaru, L.; Uchida, S.; Jena, A. K.; Miyasaka, T.; Nakazaki, J.; Kubo, T.; Segawa, H. Determination of Chloride Content in Planar $CH_3NH_3PbI_{3-x}Cl_x$ Solar Cells by Chemical Analysis. *Chem. Lett.* **2015**, *44*, 1089−1091.
(173) Li, Y.; Sun, W.; Yan, W.; Ye, S.; Peng, H.; Liu, Z.; Bian, Z.; Huang, C. High-Performance Planar Solar Cells Based On $CH_3NH_3PbI_{3-x}Cl_x$ Perovskites with Determined Chlorine Mole Fraction. *Adv. Funct. Mater.* **2015**, *25*, 4867−4873.
(174) Starr, D. E.; Sadoughi, G.; Handick, E.; Wilks, R. G.; Alsmeier, J. H.; Kohler, L.; Gorgoi, M.; Snaith, H. J.; Bar, M. Direct Observation of an Inhomogeneous Chlorine Distribution in $CH_3NH_3PbI_{3-x}Cl_x$ Layers: Surface Depletion and Interface Enrichment. *Energy Environ. Sci.* **2015**, *8*, 1609−1615.
(175) Chen, Q.; Zhou, H.; Fang, Y.; Stieg, A. Z.; Song, T.-B.; Wang, H.-H.; Xu, X.; Liu, Y.; Lu, S.; You, J.; et al. The Optoelectronic Role of Chlorine In $CH_3NH_3PbI_3$(Cl)-Based Perovskite Solar Cells. *Nat. Commun.* **2015**, *6*, 7269.
(176) Unger, E. L.; Bowring, A. R.; Tassone, C. J.; Pool, V. L.; Gold-Parker, A.; Cheacharoen, R.; Stone, K. H.; Hoke, E. T.; Toney, M. F.; McGehee, M. D. Chloride in Lead Chloride-Derived Organo-Metal Halides for Perovskite-Absorber Solar Cells. *Chem. Mater.* **2014**, *26*, 7158−7165.
(177) Jiang, M.; Wu, J.; Lan, F.; Tao, Q.; Gao, D.; Li, G. Enhancing the Performance of Planar Organo-Lead Halide Perovskite Solar Cells by Using a Mixed Halide Source. *J. Mater. Chem. A* **2015**, *3*, 963−967.
(178) Chen, Y.; Chen, T.; Dai, L. Layer-by-Layer Growth of $CH_3NH_3PbI_{3-x}Cl_x$ for Highly Efficient Planar Heterojunction Perovskite Solar Cells. *Adv. Mater.* **2015**, *27*, 1053−1059.
(179) Colella, S.; Mosconi, E.; Pellegrino, G.; Alberti, A.; Guerra, V. L. P.; Masi, S.; Listorti, A.; Rizzo, A.; Condorelli, G. G.; De Angelis, F.; et al. Elusive Presence of Chloride in Mixed Halide Perovskite Solar Cells. *J. Phys. Chem. Lett.* **2014**, *5*, 3532−3538.
(180) Pistor, P.; Borchert, J.; Fränzel, W.; Csuk, R.; Scheer, R. Monitoring the Phase Formation of Coevaporated Lead Halide Perovskite Thin Films by in Situ X-ray Diffraction. *J. Phys. Chem. Lett.* **2014**, *5*, 3308−3312.
(181) Yantara, N.; Yanan, F.; Shi, C.; Dewi, H. A.; Boix, P. P.; Mhaisalkar, S. G.; Mathews, N. Unravelling the Effects of Cl Addition in Single Step $CH_3NH_3PbI_3$ Perovskite Solar Cells. *Chem. Mater.* **2015**, *27*, 2309−2314.
(182) Yu, H.; Wang, F.; Xie, F.; Li, W.; Chen, J.; Zhao, N. The Role of Chlorine in the Formation Process of "$CH_3NH_3PbI_{3-x}Cl_x$" Perovskite. *Adv. Funct. Mater.* **2014**, *24*, 7102−7108.
(183) You, J.; Hong, Z.; Yang, Y.; Chen, Q.; Cai, M.; Song, T.-B.; Chen, C.-C.; Lu, S.; Liu, Y.; Zhou, H.; et al. Low-Temperature Solution-Processed Perovskite Solar Cells with High Efficiency and Flexibility. *ACS Nano* **2014**, *8*, 1674−1680.
(184) Conings, B.; Baeten, L.; De Dobbelaere, C.; D'Haen, J.; Manca, J.; Boyen, H. G. Perovskite-Based Hybrid Solar Cells Exceeding 10% Efficiency with High Reproducibility Using a Thin Film Sandwich Approach. *Adv. Mater.* **2014**, *26*, 2041−2046.
(185) Colella, S.; Mosconi, E.; Fedeli, P.; Listorti, A.; Gazza, F.; Orlandi, F.; Ferro, P.; Besagni, T.; Rizzo, A.; Calestani, G.; et al. $MAPbI_{3-x}Cl_x$ Mixed Halide Perovskite for Hybrid Solar Cells: The Role of Chloride as Dopant on the Transport and Structural Properties. *Chem. Mater.* **2013**, *25*, 4613−4618.
(186) Fan, L.; Ding, Y.; Luo, J. S.; Shi, B.; Yao, X.; Wei, C. C.; Zhang, D. K.; Wang, G. C.; Sheng, Y.; Chen, Y. F.; et al. Elucidating the Role of Chlorine in Perovskite Solar Cells. *J. Mater. Chem. A* **2017**, *5*, 7423−7432.
(187) Zhang, X.; Liu, C.; Ma, Y.; Shen, Y.; Li, H.; Chen, R.; Mai, Y. Study on the Role of Additional Ions in $CH_3NH_3PbI_{3-x}Cl_x$ Planar Solar Cells. *Sol. Energy* **2017**, *148*, 70−77.
(188) Yang, B.; Keum, J.; Ovchinnikova, O. S.; Belianinov, A.; Chen, S.; Du, M.-H.; Ivanov, I. N.; Rouleau, C. M.; Geohegan, D. B.; Xiao, K. Deciphering Halogen Competition in Organometallic Halide Perovskite Growth. *J. Am. Chem. Soc.* **2016**, *138*, 5028−5035.
(189) Binek, A.; Grill, I.; Huber, N.; Peters, K.; Hufnagel, A. G.; Handloser, M.; Docampo, P.; Hartschuh, A.; Bein, T. Control of Perovskite Crystal Growth by Methylammonium Lead Chloride Templating. *Chem. - Asian J.* **2016**, *11*, 1199−1204.
(190) Ng, T.-W.; Chan, C.-Y.; Lo, M.-F.; Guan, Z. Q.; Lee, C.-S. Formation Chemistry of Perovskites with Mixed Iodide/Chloride Content and the Implications on Charge Transport Properties. *J. Mater. Chem. A* **2015**, *3*, 9081−9085.
(191) Luo, P.; Liu, Z.; Xia, W.; Yuan, C.; Cheng, J.; Xu, C.; Lu, Y. Chlorine-Conducted Defect Repairment and Seed Crystal-Mediated Vapor Growth Process for Controllable Preparation of Efficient and Stable Perovskite Solar Cells. *J. Mater. Chem. A* **2015**, *3*, 22949−22959.
(192) Xie, F. X.; Zhang, D.; Su, H.; Ren, X.; Wong, K. S.; Grätzel, M.; Choy, W. C. H. Vacuum-Assisted Thermal Annealing of $CH_3NH_3PbI_3$ for Highly Stable and Efficient Perovskite Solar Cells. *ACS Nano* **2015**, *9*, 639−646.
(193) Dar, M. I.; Arora, N.; Gao, P.; Ahmad, S.; Grätzel, M.; Nazeeruddin, M. K. Investigation Regarding the Role of Chloride in Organic-Inorganic Halide Perovskites Obtained from Chloride Containing Precursors. *Nano Lett.* **2014**, *14*, 6991−6996.
(194) Williams, S. T.; Zuo, F.; Chueh, C.-C.; Liao, C.-Y.; Liang, P.-W.; Jen, A. K. Y. Role of Chloride in the Morphological Evolution of

DOI: 10.1021/acsami.7b06001
ACS Appl. Mater. Interfaces XXXX, XXX, XXX−XXX

Organo-Lead Halide Perovskite Thin Films. *ACS Nano* **2014**, *8*, 10640−10654.
(195) Tidhar, Y.; Edri, E.; Weissman, H.; Zohar, D.; Hodes, G.; Cahen, D.; Rybtchinski, B.; Kirmayer, S. Crystallization of Methyl Ammonium Lead Halide Perovskites: Implications for Photovoltaic Applications. *J. Am. Chem. Soc.* **2014**, *136*, 13249−13256.
(196) Park, B.-W.; Philippe, B.; Gustafsson, T.; Sveinbjörnsson, K.; Hagfeldt, A.; Johansson, E. M. J.; Boschloo, G. Enhanced Crystallinity in Organic−Inorganic Lead Halide Perovskites on Mesoporous TiO_2 via Disorder−Order Phase Transition. *Chem. Mater.* **2014**, *26*, 4466−4471.
(197) Zhao, Y.; Zhu, K. CH_3NH_3Cl-Assisted One-Step Solution Growth of $CH_3NH_3PbI_3$: Structure, Charge-Carrier Dynamics, and Photovoltaic Properties of Perovskite Solar Cells. *J. Phys. Chem. C* **2014**, *118*, 9412−9418.
(198) Docampo, P.; Hanusch, F. C.; Stranks, S. D.; Döblinger, M.; Feckl, J. M.; Ehrensperger, M.; Minar, N. K.; Johnston, M. B.; Snaith, H. J.; Bein, T. Solution Deposition-Conversion for Planar Heterojunction Mixed Halide Perovskite Solar Cells. *Adv. Energy Mater.* **2014**, *4*, 1400355.
(199) Dualeh, A.; Tétreault, N.; Moehl, T.; Gao, P.; Nazeeruddin, M. K.; Grätzel, M. Effect of Annealing Temperature on Film Morphology of Organic-Inorganic Hybrid Pervoskite Solid-State Solar Cells. *Adv. Funct. Mater.* **2014**, *24*, 3250−3258.
(200) Stranks, S. D.; Eperon, G. E.; Grancini, G.; Menelaou, C.; Alcocer, M. J. P.; Leijtens, T.; Herz, L. M.; Petrozza, A.; Snaith, H. J. Electron-Hole Diffusion Lengths Exceeding 1 Micrometer in an Organometal Trihalide Perovskite Absorber. *Science* **2013**, *342*, 341−344.
(201) Im, J.-H.; Lee, C.-R.; Lee, J.-W.; Park, S.-W.; Park, N.-G. 6.5% efficient perovskite quantum-dot-sensitized solar cell. *Nanoscale* **2011**, *3*, 4088−4093.
(202) Sharenko, A.; Toney, M. F. Relationships between Lead Halide Perovskite Thin-Film Fabrication, Morphology, and Performance in Solar Cells. *J. Am. Chem. Soc.* **2016**, *138*, 463−470.
(203) Xing, G. C.; Mathews, N.; Sun, S. Y.; Lim, S. S.; Lam, Y. M.; Gratzel, M.; Mhaisalkar, S.; Sum, T. C. Long-Range Balanced Electron- and Hole-Transport Lengths in Organic-Inorganic $CH_3NH_3PbI_3$. *Science* **2013**, *342*, 344−347.
(204) Luo, S.; Daoud, W. Crystal Structure Formation of $CH_3NH_3PbI_{3-x}Cl_x$ Perovskite. *Materials* **2016**, *9*, 123.
(205) Dong, Q.; Yuan, Y.; Shao, Y.; Fang, Y.; Wang, Q.; Huang, J. Abnormal Crystal growth in $CH_3NH_3PbI_{3-x}Cl_x$ Using a Multi-Cycle Solution Coating Process. *Energy Environ. Sci.* **2015**, *8*, 2464−2470.
(206) Mosconi, E.; Amat, A.; Nazeeruddin, M. K.; Grätzel, M.; De Angelis, F. First-Principles Modeling of Mixed Halide Organometal Perovskites for Photovoltaic Applications. *J. Phys. Chem. C* **2013**, *117*, 13902−13913.
(207) Zheng, F.; Takenaka, H.; Wang, F.; Koocher, N. Z.; Rappe, A. M. First-Principles Calculation of the Bulk Photovoltaic Effect in $CH_3NH_3PbI_3$ and $CH_3NH_3PbI_{3-x}Cl_x$. *J. Phys. Chem. Lett.* **2015**, *6*, 31−37.
(208) Motta, C.; El-Mellouhi, F.; Sanvito, S. Charge carrier mobility in hybrid halide perovskites. *Sci. Rep.* **2015**, *5*, 12746.
(209) Lian, Z.; Yan, Q.; Gao, T.; Ding, J.; Lv, Q.; Ning, C.; Li, Q.; Sun, J.-l. Perovskite $CH_3NH_3PbI_3(Cl)$ Single Crystals: Rapid Solution Growth, Unparalleled Crystalline Quality, and Low Trap Density toward 10^8 cm^{-3}. *J. Am. Chem. Soc.* **2016**, *138*, 9409−9412.
(210) Li, G.; Zhang, T.; Zhao, Y. Hydrochloric Acid Accelerated Formation of Planar $CH_3NH_3PbI_3$ Perovskite With High Humidity Tolerance. *J. Mater. Chem. A* **2015**, *3*, 19674−19678.
(211) Yang, L.; Wang, J.; Leung, W. W.-F. Lead Iodide Thin Film Crystallization Control for High-Performance and Stable Solution-Processed Perovskite Solar Cells. *ACS Appl. Mater. Interfaces* **2015**, *7*, 14614−14619.
(212) Pan, J.; Mu, C.; Li, Q.; Li, W.; Ma, D.; Xu, D. Room-Temperature, Hydrochloride-Assisted, One-Step Deposition for Highly Efficient and Air-Stable Perovskite Solar Cells. *Adv. Mater.* **2016**, *28*, 8309−8314.
(213) Chen, Y.; Zhao, Y.; Liang, Z. Non-Thermal Annealing Fabrication of Efficient Planar Perovskite Solar Cells with Inclusion of NH_4Cl. *Chem. Mater.* **2015**, *27*, 1448−1451.
(214) Chen, Y.; Zhao, Y.; Liang, Z. Nonvolatile Chlorinated Additives Adversely Influence $CH_3NH_3PbI_3$ Based Planar Solar Cells. *J. Mater. Chem. A* **2015**, *3*, 9137−9140.
(215) Sun, C.; Xue, Q.; Hu, Z.; Chen, Z.; Huang, F.; Yip, H.-L.; Cao, Y. Phosphonium Halides as Both Processing Additives and Interfacial Modifiers for High Performance Planar-Heterojunction Perovskite Solar Cells. *Small* **2015**, *11*, 3344−3350.
(216) Li, X.; Ibrahim Dar, M.; Yi, C.; Luo, J.; Tschumi, M.; Zakeeruddin, S. M.; Nazeeruddin, M. K.; Han, H.; Grätzel, M. Improved Performance and Stability of Perovskite Solar Cells by Crystal Crosslinking with Alkylphosphonic Acid ω-Ammonium Chlorides. *Nat. Chem.* **2015**, *7*, 703−711.
(217) Chen, Y.; He, M.; Peng, J.; Sun, Y.; Liang, Z. Structure and Growth Control of Organic−Inorganic Halide Perovskites for Optoelectronics: From Polycrystalline Films to Single Crystals. *Adv. Sci.* **2016**, *3*, 1500392.
(218) Lv, S.; Pang, S.; Zhou, Y.; Padture, N. P.; Hu, H.; Wang, L.; Zhou, X.; Zhu, H.; Zhang, L.; Huang, C.; et al. One-Step, Solution-Processed Formamidinium Lead Trihalide $(FAPbI_{(3-x)}Cl_x)$ for Mesoscopic Perovskite-Polymer Solar Cells. *Phys. Chem. Chem. Phys.* **2014**, *16*, 19206−19211.
(219) Wang, Z.; Zhou, Y.; Pang, S.; Xiao, Z.; Zhang, J.; Chai, W.; Xu, H.; Liu, Z.; Padture, N. P.; Cui, G. Additive-Modulated Evolution of $HC(NH_2)_2PbI_3$ Black Polymorph for Mesoscopic Perovskite Solar Cells. *Chem. Mater.* **2015**, *27*, 7149−7155.
(220) Noh, J. H.; Im, S. H.; Heo, J. H.; Mandal, T. N.; Seok, S. I. Chemical Management For Colorful, Efficient, and Stable Inorganic-Organic Hybrid Nanostructured Solar Cells. *Nano Lett.* **2013**, *13*, 1764−1769.
(221) Gil-Escrig, L.; Miquel-Sempere, A.; Sessolo, M.; Bolink, H. J. Mixed Iodide−Bromide Methylammonium Lead Perovskite-based Diodes for Light Emission and Photovoltaics. *J. Phys. Chem. Lett.* **2015**, *6*, 3743−3748.
(222) Sutter-Fella, C. M.; Li, Y.; Amani, M.; Ager, J. W.; Toma, F. M.; Yablonovitch, E.; Sharp, I. D.; Javey, A. High Photoluminescence Quantum Yield in Band Gap Tunable Bromide Containing Mixed Halide Perovskites. *Nano Lett.* **2016**, *16*, 800−806.
(223) Cao, K.; Li, H.; Liu, S.; Cui, J.; Shen, Y.; Wang, M. $MAPbI_{3-x}Br_x$ Mixed Halide Perovskites for Fully Printable Mesoscopic Solar Cells with Enhanced Efficiency and Less Hysteresis. *Nanoscale* **2016**, *8*, 8839−8846.
(224) Kulkarni, S. A.; Baikie, T.; Boix, P. P.; Yantara, N.; Mathews, N.; Mhaisalkar, S. Band-Gap Tuning of Lead Halide Perovskites Using a Sequential Deposition Process. *J. Mater. Chem. A* **2014**, *2*, 9221−9225.
(225) Aharon, S.; Cohen, B. E.; Etgar, L. Hybrid Lead Halide Iodide and Lead Halide Bromide in Efficient Hole Conductor Free Perovskite Solar Cell. *J. Phys. Chem. C* **2014**, *118*, 17160−17165.
(226) Fedeli, P.; Gazza, F.; Calestani, D.; Ferro, P.; Besagni, T.; Zappettini, A.; Calestani, G.; Marchi, E.; Ceroni, P.; Mosca, R. Influence of the Synthetic Procedures on the Structural and Optical Properties of Mixed-Halide (Br,I) Perovskite Films. *J. Phys. Chem. C* **2015**, *119*, 21304−21313.
(227) Misra, R. K.; Ciammaruchi, L.; Aharon, S.; Mogilyansky, D.; Etgar, L.; Visoly-Fisher, I.; Katz, E. A. Effect of Halide Composition on the Photochemical Stability of Perovskite Photovoltaic Materials. *ChemSusChem* **2016**, *9*, 2572−2577.
(228) Jong, U.-G.; Yu, C.-J.; Ri, J.-S.; Kim, N.-H.; Ri, G.-C. Influence of Halide Composition on the Structural, Electronic, and Optical Properties of Mixed $CH_3NH_3Pb(I_{1-x}Br_x)_3$ Perovskites Calculated Using the Virtual Crystal Approximation Method. *Phys. Rev. B: Condens. Matter Mater. Phys.* **2016**, *94*, 125139.
(229) Brivio, F.; Caetano, C.; Walsh, A. Thermodynamic Origin of Photoinstability in the $CH_3NH_3Pb(I_{1-x}Br_x)_3$ Hybrid Halide Perovskite Alloy. *J. Phys. Chem. Lett.* **2016**, *7*, 1083−1087.

DOI: 10.1021/acsami.7b06001
ACS Appl. Mater. Interfaces XXXX, XXX, XXX−XXX

(230) De Wolf, S.; Holovsky, J.; Moon, S. J.; Loper, P.; Niesen, B.; Ledinsky, M.; Haug, F. J.; Yum, J. H.; Ballif, C. Organometallic Halide Perovskites: Sharp Optical Absorption Edge and Its Relation to Photovoltaic Performance. *J. Phys. Chem. Lett.* **2014**, *5*, 1035−1039.
(231) Sadhanala, A.; Deschler, F.; Thomas, T. H.; Dutton, S. E.; Goedel, K. C.; Hanusch, F. C.; Lai, M. L.; Steiner, U.; Bein, T.; Docampo, P.; et al. Preparation of Single-Phase Films of $CH_3NH_3Pb(I_{1-x}Br_x)_3$ with Sharp Optical Band Edges. *J. Phys. Chem. Lett.* **2014**, *5*, 2501−2505.
(232) Yuan, Y.; Huang, J. Ion Migration in Organometal Trihalide Perovskite and Its Impact on Photovoltaic Efficiency and Stability. *Acc. Chem. Res.* **2016**, *49*, 286−293.
(233) Bischak, C. G.; Hetherington, C. L.; Wu, H.; Aloni, S.; Ogletree, D. F.; Limmer, D. T.; Ginsberg, N. S. Origin of Reversible Photoinduced Phase Separation in Hybrid Perovskites. *Nano Lett.* **2017**, *17*, 1028−1033.
(234) Hoke, E. T.; Slotcavage, D. J.; Dohner, E. R.; Bowring, A. R.; Karunadasa, H. I.; McGehee, M. D. Reversible Photo-Induced Trap Formation in Mixed-Halide Hybrid Perovskites for Photovoltaics. *Chem. Sci.* **2015**, *6*, 613−617.
(235) Yang, X.; Yan, X.; Wang, W.; Zhu, X.; Li, H.; Ma, W.; Sheng, C. Light Induced Metastable Modification of Optical Properties in $CH_3NH_3PbI_{3-x}Br_x$ Perovskite Films: Two-Step Mechanism. *Org. Electron.* **2016**, *34*, 79−83.
(236) Yoon, S. J.; Draguta, S.; Manser, J. S.; Sharia, O.; Schneider, W. F.; Kuno, M.; Kamat, P. V. Tracking Iodide and Bromide Ion Segregation in Mixed Halide Lead Perovskites during Photoirradiation. *ACS Energy Lett.* **2016**, *1*, 290−296.
(237) Slotcavage, D. J.; Karunadasa, H. I.; McGehee, M. D. Light-Induced Phase Segregation in Halide-Perovskite Absorbers. *ACS Energy Lett.* **2016**, *1*, 1199−1205.
(238) Snaith, H. J.; Abate, A.; Ball, J. M.; Eperon, G. E.; Leijtens, T.; Noel, N. K.; Stranks, S. D.; Wang, J. T.-W.; Wojciechowski, K.; Zhang, W. Anomalous Hysteresis in Perovskite Solar Cells. *J. Phys. Chem. Lett.* **2014**, *5*, 1511−1515.
(239) Egger, D. A.; Rappe, A. M.; Kronik, L. Hybrid Organic−Inorganic Perovskites on the Move. *Acc. Chem. Res.* **2016**, *49*, 573−581.
(240) Unger, E. L.; Kegelmann, L.; Suchan, K.; Sörell, D.; Korte, L.; Albrecht, S. Roadmap and Roadblocks for the Band Gap Tunability of Metal Halide Perovskites. *J. Mater. Chem. A* **2017**, *5*, 11401−11409.
(241) Hu, M.; Bi, C.; Yuan, Y.; Bai, Y.; Huang, J. Stabilized Wide Bandgap $MAPbBr_xI_{3-x}$ Perovskite by Enhanced Grain Size and Improved Crystallinity. *Adv. Sci.* **2016**, *3*, 1500301.
(242) Rehman, W.; Milot, R. L.; Eperon, G. E.; Wehrenfennig, C.; Boland, J. L.; Snaith, H. J.; Johnston, M. B.; Herz, L. M. Charge-Carrier Dynamics and Mobilities in Formamidinium Lead Mixed-Halide Perovskites. *Adv. Mater.* **2015**, *27*, 7938−7944.
(243) Zhang, M.; Yu, H.; Lyu, M.; Wang, Q.; Yun, J.-H.; Wang, L. Composition-Dependent Photoluminescence Intensity and Prolonged Recombination Lifetime of Perovskite $CH_3NH_3PbBr_{3-x}Cl_x$ Films. *Chem. Commun.* **2014**, *50*, 11727−11730.
(244) Niemann, R. G.; Kontos, A. G.; Palles, D.; Kamitsos, E. I.; Kaltzoglou, A.; Brivio, F.; Falaras, P.; Cameron, P. J. Halogen Effects on Ordering and Bonding of $CH_3NH_3^+$ in $CH_3NH_3PbX_3$ (X = Cl, Br, I) Hybrid Perovskites: A Vibrational Spectroscopic Study. *J. Phys. Chem. C* **2016**, *120*, 2509−2519.
(245) Wei, M.; Chung, Y.-H.; Xiao, Y.; Chen, Z. Color Tunable Halide Perovskite $CH_3NH_3PbBr_{3-x}Cl_x$ Emission via Annealing. *Org. Electron.* **2015**, *26*, 260−264.
(246) Fang, Y.; Dong, Q.; Shao, Y.; Yuan, Y.; Huang, J. Highly Narrowband Perovskite Single-Crystal Photodetectors Enabled by Surface-Charge Recombination. *Nat. Photonics* **2015**, *9*, 679−686.
(247) Zhang, T.; Yang, M.; Benson, E. E.; Li, Z.; van de Lagemaat, J.; Luther, J. M.; Yan, Y.; Zhu, K.; Zhao, Y. A Facile Solvothermal Growth of Single Crystal Mixed Halide Perovskite $CH_3NH_3Pb(Br_{1-x}Cl_x)_3$. *Chem. Commun.* **2015**, *51*, 7820−7823.
(248) Edri, E.; Kirmayer, S.; Kulbak, M.; Hodes, G.; Cahen, D. Chloride Inclusion and Hole Transport Material Doping to Improve Methyl Ammonium Lead Bromide Perovskite-Based High Open-Circuit Voltage Solar Cells. *J. Phys. Chem. Lett.* **2014**, *5*, 429−433.
(249) Kitazawa, N.; Watanabe, Y.; Nakamura, Y. Optical Properties of $CH_3NH_3PbX_3$ (X = Halogen) and their Mixed-Halide Crystals. *J. Mater. Sci.* **2002**, *37*, 3585−3587.
(250) Yin, W.-J.; Yan, Y.; Wei, S.-H. Anomalous Alloy Properties in Mixed Halide Perovskites. *J. Phys. Chem. Lett.* **2014**, *5*, 3625−3631.
(251) Tan, Z. K.; Moghaddam, R. S.; Lai, M. L.; Docampo, P.; Higler, R.; Deschler, F.; Price, M.; Sadhanala, A.; Pazos, L. M.; Credgington, D.; et al. Bright Light-Emitting Diodes Based on Organometal Halide Perovskite. *Nat. Nanotechnol.* **2014**, *9*, 687−692.
(252) Zhang, F.; Zhong, H.; Chen, C.; Wu, X.-g.; Hu, X.; Huang, H.; Han, J.; Zou, B.; Dong, Y. Brightly Luminescent and Color-Tunable Colloidal $CH_3NH_3PbX_3$ (X = Br, I, Cl) Quantum Dots: Potential Alternatives for Display Technology. *ACS Nano* **2015**, *9*, 4533−4542.
(253) Kim, Y.-H.; Cho, H.; Heo, J. H.; Kim, T.-S.; Myoung, N.; Lee, C.-L.; Im, S. H.; Lee, T.-W. Multicolored Organic/Inorganic Hybrid Perovskite Light-Emitting Diodes. *Adv. Mater.* **2015**, *27*, 1248−1254.
(254) Suarez, B.; Gonzalez-Pedro, V.; Ripolles, T. S.; Sanchez, R. S.; Otero, L.; Mora-Sero, I. Recombination study of combined halides (Cl, Br, I) perovskite solar cells. *J. Phys. Chem. Lett.* **2014**, *5*, 1628−1635.
(255) Zhao, Y.; Zhu, K. Efficient Planar Perovskite Solar Cells Based on 1.8 eV Band Gap CH3NH3PbI2Br Nanosheets via Thermal Decomposition. *J. Am. Chem. Soc.* **2014**, *136*, 12241−12244.
(256) Chiang, C.-H.; Lin, J.-W.; Wu, C.-G. One-Step Fabrication of a Mixed-Halide Perovskite Film for a High-Efficiency Inverted Solar Cell and Module. *J. Mater. Chem. A* **2016**, *4*, 13525−13533.
(257) Beal, R. E.; Slotcavage, D. J.; Leijtens, T.; Bowring, A. R.; Belisle, R. A.; Nguyen, W. H.; Burkhard, G. F.; Hoke, E. T.; McGehee, M. D. Cesium Lead Halide Perovskites with Improved Stability for Tandem Solar Cells. *J. Phys. Chem. Lett.* **2016**, *7*, 746−751.
(258) Ma, Q.; Huang, S.; Wen, X.; Green, M. A.; Ho-Baillie, A. W. Y. Hole Transport Layer Free Inorganic $CsPbIBr_2$ Perovskite Solar Cell by Dual Source Thermal Evaporation. *Adv. Energy Mater.* **2016**, *6*, 1502202.
(259) Domanski, K.; Roose, B.; Matsui, T.; Saliba, M.; Turren-Cruz, S. H.; Correa-Baena, J. P.; Carmona, C. R.; Richardson, G.; Foster, J. M.; De Angelis, F.; et al. Migration of Cations Induces Reversible Performance Losses Over Day/Night Cycling in Perovskite Solar Cells. *Energy Environ. Sci.* **2017**, *10*, 604−613.
(260) Eperon, G. E.; Leijtens, T.; Bush, K. A.; Prasanna, R.; Green, T.; Wang, J. T.-W.; McMeekin, D. P.; Volonakis, G.; Milot, R. L.; May, R.; et al. Perovskite-Perovskite Tandem Photovoltaics with Optimized Band Gaps. *Science* **2016**, *354*, 861−865.
(261) Rehman, W.; McMeekin, D. P.; Patel, J. B.; Milot, R. L.; Johnston, M. B.; Snaith, H. J.; Herz, L. M. Photovoltaic Mixed-Cation Lead Mixed-Halide Perovskites: Links Between Crystallinity, Photo-Stability and Electronic Properties. *Energy Environ. Sci.* **2017**, *10*, 361−369.
(262) Conings, B.; Babayigit, A.; Klug, M. T.; Bai, S.; Gauquelin, N.; Sakai, N.; Wang, J. T.-W.; Verbeeck, J.; Boyen, H.-G.; Snaith, H. J. A Universal Deposition Protocol for Planar Heterojunction Solar Cells with High Efficiency Based on Hybrid Lead Halide Perovskite Families. *Adv. Mater.* **2016**, *28*, 10701−10709.
(263) Leblebici, S. Y.; Leppert, L.; Li, Y.; Reyes-Lillo, S. E.; Wickenburg, S.; Wong, E.; Lee, J.; Melli, M.; Ziegler, D.; Angell, D. K.; et al. Facet-Dependent Photovoltaic Efficiency Variations in Single Grains of Hybrid Halide Perovskite. *Nat. Energy* **2016**, *1*, 16093.
(264) Shallcross, R. C.; Zheng, Y.; Saavedra, S. S.; Armstrong, N. R. Determining Band-Edge Energies and Morphology-Dependent Stability of Formamidinium Lead Perovskite Films Using Spectroelectrochemistry and Photoelectron Spectroscopy. *J. Am. Chem. Soc.* **2017**, *139*, 4866−4878.
(265) Bella, F.; Griffini, G.; Correa-Baena, J.-P.; Saracco, G.; Grätzel, M.; Hagfeldt, A.; Turri, S.; Gerbaldi, C. Improving Efficiency and Stability of Perovskite Solar Cells with Photocurable Fluoropolymers. *Science* **2016**, *354*, 203−206.

DOI: 10.1021/acsami.7b06001
ACS Appl. Mater. Interfaces XXXX, XXX, XXX−XXX

(266) Tress, W.; Correa Baena, J. P.; Saliba, M.; Abate, A.; Graetzel, M. Inverted Current−Voltage Hysteresis in Mixed Perovskite Solar Cells: Polarization, Energy Barriers, and Defect Recombination. *Adv. Energy Mater.* **2016**, *6*, 1600396.
(267) Abate, A.; Paek, S.; Giordano, F.; Correa-Baena, J.-P.; Saliba, M.; Gao, P.; Matsui, T.; Ko, J.; Zakeeruddin, S. M.; Dahmen, K. H.; et al. Silolothiophene-Linked Triphenylamines as Stable Hole Transporting Materials for High Efficiency Perovskite Solar Cells. *Energy Environ. Sci.* **2015**, *8*, 2946−2953.
(268) Domanski, K.; Correa-Baena, J.-P.; Mine, N.; Nazeeruddin, M. K.; Abate, A.; Saliba, M.; Tress, W.; Hagfeldt, A.; Grätzel, M. Not All That Glitters Is Gold: Metal-Migration-Induced Degradation in Perovskite Solar Cells. *ACS Nano* **2016**, *10*, 6306−6314.
(269) Zhang, L.; Tian, F.; Xie, Z.; Qin, G. Efficiency Evaluation on $Cs_x[NH_2CH = NH_2]_{1-x}Pb(I_{1-y}Br_y)_3$/Crystalline Silicon Tandem Solar Cells. *Sol. Energy* **2017**, *147*, 432−438.
(270) Philippe, B.; Saliba, M.; Correa-Baena, J.-P.; Cappel, U. B.; Turren-Cruz, S.-H.; Grätzel, M.; Hagfeldt, A.; Rensmo, H. Chemical Distribution of Multiple Cation (Rb^+, Cs^+, MA^+, and FA^+) Perovskite Materials by Photoelectron Spectroscopy. *Chem. Mater.* **2017**, *29*, 3589−3596.
(271) Leijtens, T.; Bush, K.; Cheacharoen, R.; Beal, R.; Bowring, A.; McGehee, M. D. Towards Enabling Stable Lead Halide Perovskite Solar Cells; Interplay Between Structural, Environmental, and Thermal Stability. *J. Mater. Chem. A* **2017**, *5*, 11483−11500.
(272) Leijtens, T.; Eperon, G. E.; Noel, N. K.; Habisreutinger, S. N.; Petrozza, A.; Snaith, H. J. Stability of Metal Halide Perovskite Solar Cells. *Adv. Energy Mater.* **2015**, *5*, 1500963.
(273) Peng, Y.; Jing, G.; Cui, T. High Performance Perovskite Solar Cells through Vapor Deposition with Optimized PbI_2 Precursor Films. *RSC Adv.* **2015**, *5*, 95847−95853.
(274) Dong, Q.; Song, J.; Fang, Y.; Shao, Y.; Ducharme, S.; Huang, J. Lateral-Structure Single-Crystal Hybrid Perovskite Solar Cells via Piezoelectric Poling. *Adv. Mater.* **2016**, *28*, 2816−2821.
(275) Dong, Q.; Fang, Y.; Shao, Y.; Mulligan, P.; Qiu, J.; Cao, L.; Huang, J. Electron-Hole Diffusion Lengths > 175 μm in Solution-Grown $CH_3NH_3PbI_3$ Single Crystals. *Science* **2015**, *347*, 967−970.
(276) Schulz, P.; Edri, E.; Kirmayer, S.; Hodes, G.; Cahen, D.; Kahn, A. Interface Energetics in Organo-Metal Halide Perovskite-Based Photovoltaic Cells. *Energy Environ. Sci.* **2014**, *7*, 1377−1381.
(277) Schulz, P.; Whittaker-Brooks, L. L.; MacLeod, B. A.; Olson, D. C.; Loo, Y.-L.; Kahn, A. Electronic Level Alignment in Inverted Organometal Perovskite Solar Cells. *Adv. Mater. Interfaces* **2015**, *2*, 1400532.
(278) Schulz, P.; Dowgiallo, A.-M.; Yang, M.; Zhu, K.; Blackburn, J. L.; Berry, J. J. Charge Transfer Dynamics between Carbon Nanotubes and Hybrid Organic Metal Halide Perovskite Films. *J. Phys. Chem. Lett.* **2016**, *7*, 418−425.
(279) Endres, J.; Egger, D. A.; Kulbak, M.; Kerner, R. A.; Zhao, L.; Silver, S. H.; Hodes, G.; Rand, B. P.; Cahen, D.; Kronik, L.; et al. Valence and Conduction Band Densities of States of Metal Halide Perovskites: A Combined Experimental−Theoretical Study. *J. Phys. Chem. Lett.* **2016**, *7*, 2722−2729.
(280) Endres, J.; Kulbak, M.; Zhao, L.; Rand, B. P.; Cahen, D.; Hodes, G.; Kahn, A. Electronic structure of the $CsPbBr_3$/polytriarylamine (PTAA) system. *J. Appl. Phys.* **2017**, *121*, 035304.
(281) Emara, J.; Schnier, T.; Pourdavoud, N.; Riedl, T.; Meerholz, K.; Olthof, S. Impact of Film Stoichiometry on the Ionization Energy and Electronic Structure of $CH_3NH_3PbI_3$ Perovskites. *Adv. Mater.* **2016**, *28*, 553−559.
(282) Olthof, S.; Meerholz, K. Substrate-dependent electronic structure and film formation of MAPbI3 perovskites. *Sci. Rep.* **2017**, *7*, 40267.
(283) Wang, Q. K.; Wang, R. B.; Shen, P. F.; Li, C.; Li, Y. Q.; Liu, L. J.; Duhm, S.; Tang, J. X. Energy Level Offsets at Lead Halide Perovskite/Organic Hybrid Interfaces and Their Impacts on Charge Separation. *Adv. Mater. Interfaces* **2015**, *2*, 1400528.
(284) Li, C.; Wei, J.; Sato, M.; Koike, H.; Xie, Z.-Z.; Li, Y.-Q.; Kanai, K.; Kera, S.; Ueno, N.; Tang, J.-X. Halide-Substituted Electronic Properties of Organometal Halide Perovskite Films: Direct and Inverse Photoemission Studies. *ACS Appl. Mater. Interfaces* **2016**, *8*, 11526−11531.
(285) Liu, X. L.; Wang, C. G.; Lyu, L.; Wang, C. C.; Xiao, Z. G.; Bi, C.; Huang, J. S.; Gao, Y. L. Electronic Structures at the Interface between Au and $CH_3NH_3PbI_3$. *Phys. Chem. Chem. Phys.* **2015**, *17*, 896−902.
(286) Chen, S.; Goh, T. W.; Sabba, D.; Chua, J.; Mathews, N.; Huan, C. H. A.; Sum, T. C. Energy Level Alignment at the Methylammonium Lead Iodide/Copper Phthalocyanine Interface. *APL Mater.* **2014**, *2*, 081512.
(287) Wang, C. G.; Liu, X. L.; Wang, C. C.; Xiao, Z. G.; Bi, C.; Shao, Y. C.; Huang, J. S.; Gao, Y. L. Surface Analytical Investigation on Organometal Triiodide Perovskite. *J. Vac. Sci. Technol., B: Nanotechnol. Microelectron.: Mater., Process., Meas., Phenom.* **2015**, *33*, 032401.
(288) Liu, P.; Liu, X. L.; Lyu, L.; Xie, H. P.; Zhang, H.; Niu, D. M.; Huang, H.; Bi, C.; Xiao, Z. G.; Huang, J. S.; et al. Interfacial Electronic Structure at the $CH_3NH_3PbI_3/MoO_x$ Interface. *Appl. Phys. Lett.* **2015**, *106*, 193903.
(289) Miller, E. M.; Zhao, Y. X.; Mercado, C. C.; Saha, S. K.; Luther, J. M.; Zhu, K.; Stevanovic, V.; Perkins, C. L.; van de Lagemaat, J. Substrate-Controlled Band Positions in $CH_3NH_3PbI_3$ Perovskite Films. *Phys. Chem. Chem. Phys.* **2014**, *16*, 22122−22130.
(290) Thibau, E. S.; Llanos, A.; Lu, Z. H. A simple rule for determining the band offset at CH3NH3PbI3/organic semiconductor heterojunctions. *Appl. Phys. Lett.* **2016**, *108*, 021602.
(291) Jiang, C.-S.; Yang, M.; Zhou, Y.; To, B.; Nanayakkara, S. U.; Luther, J. M.; Zhou, W.; Berry, J. J.; van de Lagemaat, J.; Padture, N. P.; et al. Carrier Separation and Transport in Perovskite Solar Cells Studied by Nanometre-Scale Profiling of Electrical Potential. *Nat. Commun.* **2015**, *6*, 8397.
(292) Bergmann, V. W.; Weber, S. A. L.; Javier Ramos, F.; Nazeeruddin, M. K.; Grätzel, M.; Li, D.; Domanski, A. L.; Lieberwirth, I.; Ahmad, S.; Berger, R. Real-Space Observation of Unbalanced Charge Distribution Inside a Perovskite-Sensitized Solar Cell. *Nat. Commun.* **2014**, *5*, 5001.
(293) Guerrero, A.; Juarez-Perez, E. J.; Bisquert, J.; Mora-Sero, I.; Garcia-Belmonte, G. Electrical Field Profile and Doping in Planar Lead Halide Perovskite Solar Cells. *Appl. Phys. Lett.* **2014**, *105*, 133902.
(294) Chakraborty, S.; Xie, W.; Mathews, N.; Sherburne, M.; Ahuja, R.; Asta, M.; Mhaisalkar, S. G. Rational Design: A High-Throughput Computational Screening and Experimental Validation Methodology for Lead-Free and Emergent Hybrid Perovskites. *ACS Energy Lett.* **2017**, *2*, 837−845.
(295) Kamat, P. V.; Bisquert, J.; Buriak, J. Lead-Free Perovskite Solar Cells. *ACS Energy Lett.* **2017**, *2*, 904−905.
(296) Volonakis, G.; Filip, M. R.; Haghighirad, A. A.; Sakai, N.; Wenger, B.; Snaith, H. J.; Giustino, F. Lead-Free Halide Double Perovskites via Heterovalent Substitution of Noble Metals. *J. Phys. Chem. Lett.* **2016**, *7*, 1254−1259.
(297) Savory, C. N.; Walsh, A.; Scanlon, D. O. Can Pb-Free Halide Double Perovskites Support High-Efficiency Solar Cells? *ACS Energy Lett.* **2016**, *1*, 949−955.
(298) Harikesh, P. C.; Mulmudi, H. K.; Ghosh, B.; Goh, T. W.; Teng, Y. T.; Thirumal, K.; Lockrey, M.; Weber, K.; Koh, T. M.; Li, S.; et al. Rb as an Alternative Cation for Templating Inorganic Lead-Free Perovskites for Solution Processed Photovoltaics. *Chem. Mater.* **2016**, *28*, 7496−7504.
(299) Giustino, F.; Snaith, H. J. Toward Lead-Free Perovskite Solar Cells. *ACS Energy Lett.* **2016**, *1*, 1233−1240.
(300) Gupta, S.; Bendikov, T.; Hodes, G.; Cahen, D. $CsSnBr_3$, A Lead-Free Halide Perovskite for Long-Term Solar Cell Application: Insights on SnF_2 Addition. *ACS Energy Lett.* **2016**, *1*, 1028−1033.
(301) Yokoyama, T.; Cao, D. H.; Stoumpos, C. C.; Song, T.-B.; Sato, Y.; Aramaki, S.; Kanatzidis, M. G. Overcoming Short-Circuit in Lead-Free $CH_3NH_3SnI_3$ Perovskite Solar Cells via Kinetically Controlled Gas−Solid Reaction Film Fabrication Process. *J. Phys. Chem. Lett.* **2016**, *7*, 776−782.

DOI: 10.1021/acsami.7b06001
ACS Appl. Mater. Interfaces XXXX, XXX, XXX−XXX

(302) Liao, W.; Zhao, D.; Yu, Y.; Grice, C. R.; Wang, C.; Cimaroli, A. J.; Schulz, P.; Meng, W.; Zhu, K.; Xiong, R.-G.; et al. Lead-Free Inverted Planar Formamidinium Tin Triiodide Perovskite Solar Cells Achieving Power Conversion Efficiencies up to 6.22%. *Adv. Mater.* **2016**, *28*, 9333−9340.
(303) Yu, Y.; Zhao, D.; Grice, C. R.; Meng, W.; Wang, C.; Liao, W.; Cimaroli, A. J.; Zhang, H.; Zhu, K.; Yan, Y. Thermally Evaporated Methylammonium Tin Triiodide Thin Films for Lead-Free Perovskite Solar Cell Fabrication. *RSC Adv.* **2016**, *6*, 90248−90254.
(304) Vigneshwaran, M.; Ohta, T.; Iikubo, S.; Kapil, G.; Ripolles, T. S.; Ogomi, Y.; Ma, T.; Pandey, S. S.; Shen, Q.; Toyoda, T.; et al. Facile Synthesis and Characterization of Sulfur Doped Low Bandgap Bismuth Based Perovskites by Soluble Precursor Route. *Chem. Mater.* **2016**, *28*, 6436−6440.
(305) Ogomi, Y.; Morita, A.; Tsukamoto, S.; Saitho, T.; Fujikawa, N.; Shen, Q.; Toyoda, T.; Yoshino, K.; Pandey, S. S.; Ma, T. L.; et al. $CH_3NH_3Sn_xPb_{(1-x)}I_3$ Perovskite Solar Cells Covering up to 1060 nm. *J. Phys. Chem. Lett.* **2014**, *5*, 1004−1011.
(306) Xiao, Z. W.; Meng, W. W.; Wang, J. B.; Mitzi, D. B.; Yan, Y. F. Searching for Promising New Perovskite-Based Photovoltaic Absorbers: The Importance of Electronic Dimensionality. *Mater. Horiz.* **2017**, *4*, 206−216.
(307) Filip, M. R.; Eperon, G. E.; Snaith, H. J.; Giustino, F. Steric engineering of metal-halide perovskites with tunable optical band gaps. *Nat. Commun.* **2014**, *5*, 5757.
(308) Filip, M. R.; Giustino, F. Computational Screening of Homovalent Lead Substitution in Organic−Inorganic Halide Perovskites. *J. Phys. Chem. C* **2016**, *120*, 166−173.
(309) Korbel, S.; Marques, M. A. L.; Botti, S. Stability and electronic properties of new inorganic perovskites from high-throughput ab initio calculations. *J. Mater. Chem. C* **2016**, *4*, 3157−3167.
(310) Lee, B.; Stoumpos, C. C.; Zhou, N.; Hao, F.; Malliakas, C.; Yeh, C.-Y.; Marks, T. J.; Kanatzidis, M. G.; Chang, R. P. H. Air-Stable Molecular Semiconducting Iodosalts for Solar Cell Applications: Cs_2SnI_6 as a Hole Conductor. *J. Am. Chem. Soc.* **2014**, *136*, 15379−15385.
(311) Park, B.-W.; Philippe, B.; Zhang, X.; Rensmo, H.; Boschloo, G.; Johansson, E. M. J. Bismuth Based Hybrid Perovskites $A_3Bi_2I_9$ (A: Methylammonium or Cesium) for Solar Cell Application. *Adv. Mater.* **2015**, *27*, 6806−6813.
(312) Johansson, M. B.; Zhu, H.; Johansson, E. M. J. Extended Photo-Conversion Spectrum in Low-Toxic Bismuth Halide Perovskite Solar Cells. *J. Phys. Chem. Lett.* **2016**, *7*, 3467−3471.
(313) Hamaguchi, R.; Yoshizawa-Fujita, M.; Miyasaka, T.; Kunugita, H.; Ema, K.; Takeoka, Y.; Rikukawa, M. Formamidine and Cesium-Based Quasi-Two-Dimensional Perovskites as Photovoltaic Absorbers. *Chem. Commun.* **2017**, *53*, 4366−4369.
(314) Vassilakopoulou, A.; Papadatos, D.; Zakouras, I.; Koutselas, I. Mixtures of quasi-two and three dimensional hybrid organic-inorganic semiconducting perovskites for single layer LED. *J. Alloys Compd.* **2017**, *692*, 589−598.
(315) Smith, I. C.; Hoke, E. T.; Solis-Ibarra, D.; McGehee, M. D.; Karunadasa, H. I. A Layered Hybrid Perovskite Solar-Cell Absorber with Enhanced Moisture Stability. *Angew. Chem.* **2014**, *126*, 11414−11417.
(316) Cao, D. H.; Stoumpos, C. C.; Farha, O. K.; Hupp, J. T.; Kanatzidis, M. G. 2D Homologous Perovskites as Light-Absorbing Materials for Solar Cell Applications. *J. Am. Chem. Soc.* **2015**, *137*, 7843−7850.
(317) Slavney, A. H.; Smaha, R. W.; Smith, I. C.; Jaffe, A.; Umeyama, D.; Karunadasa, H. I. Chemical Approaches to Addressing the Instability and Toxicity of Lead-Halide Perovskite Absorbers. *Inorg. Chem.* **2017**, *56*, 46−55.

DOI: 10.1021/acsami.7b06001
ACS Appl. Mater. Interfaces XXXX, XXX, XXX−XXX